BEARING WORLD

www.bearingworld.org

Journal

Volume 2_2017

Editors: G. Poll _ A. Grunau _ B. Hagemann

Published by
FVA Forschungsvereinigung Antriebstechnik e.V.
VDMA Verlag

Imprint

Bearing World Journal
Volume 2, December 2017

Published by:
Forschungsvereinigung Antriebstechnik e.V.
Lyoner Straße 18
60528 Frankfurt am Main
Germany
www.fva-net.de

PDF-ISSN 2566-4794

Volume 2_2017

Dear reader,

Globalisation of industry increasingly requires international networking of research and development work. With BEARING WORLD, the German Research Association for Drive Technology, FVA, has initiated an international dialogue in which researchers and developers from universities and bearing manufacturers come together with users and experts from the industry. The first international Bearing World Conference, initiated and organised by FVA, took place in April 2016. More than 200 experts from 11 countries met in Hanover to share the latest research findings in the world of bearings.

With Bearing World Journal, our aim is to continue this exchange among international experts by regularly publishing high-quality scientific reports related to rolling and plain bearings. We want to offer the international research community a new international publication platform for cutting-edge research in the field of bearings.

The high quality of Bearing World Journal is ensured by the peer review process, which is carried out by the Bearing World Scientific Board.

We would like to thank all of the authors for their interesting contributions to the Bearing World Journal.

_ **Prof. Dr.-Ing. Gerhard Poll,** Initiator, Head of international Scientific Board
_ **Dr.-Ing. Arbogast Grunau,** President of the FVA Management Board
_ **Bernhard Hagemann,** Editor-in-chief

Please send the paper you intend to publish in the next issue of the Bearing World Journal via e-mail as Word document to FVA (**submission@bearingworld.org**).
In addition please attach a PDF document.

Bearing World Scientific Board

Scott Bair, Georgia Institute of Technology, USA
Prof. Harry Bhadeshia, University of Cambrigde, Great Britain
Prof. Stefan Björklund, KTH Royal Institute of Technology, Stockholm, Sweden
Prof. Benyebka Bou-Said, Institut National Des Sciences Appliquées (INSA) Lyon, France
Prof. Ludger Deters, TU Magdeburg, Germany
Prof. Duncan Dowson, University of Leeds, Great Britain
Prof. Rob Dwyer-Joyce, University of Sheffield, Great Britain
Prof. Michel Fillon, Université de Poitiers, France
Prof. Sergei Glavastkih, KTH Royal Institute of Technology, Stockholm, Sweden
Prof. Irina Goryacheva, Russian Academy of Sciences, Russia
Prof. Feng Guo, Qingdao Technological University, China
Prof. Martin Hartl, Brno University of Technology, Czech Republic
Prof. Stathis Ioannides, Imperial College London, Great Britain
Prof. Georg Jacobs, RWTH Aachen University, Germany
Prof. Motohiro Kaneta, Brno University of Technology, Czech Republic
Prof. Michael M. Khonsari, Louisiana State University, USA
Prof. Ivan Krupka, Brno University of Technology, Czech Republic
Prof. Roland Larsson, Luleå University of Technology, Sweden
Prof. Antonius Lubrecht, Institut National Des Sciences Appliquées (INSA) Lyon, France
Prof. Piet Lugt, SKF Nieuwegin; University of Twente, Enschede, Netherlands
Prof. Jianbin Luo, State Key Laboratory of Tribology, Tsinghua University, China
Prof. Guillermo Morales-Espejel, INSA Lyon, France
Prof. Anne Neville, University of Leeds, Great Britain
Prof. Hiroyuki Ohta, Nagaoka University of Technology, Japan
Prof. Gerhard Poll, Leibniz University Hanover, Germany
Prof. Martin Priest, University of Bradford, Great Britain
Prof. Farshid Sadeghi, Purdue University, Lafayette, Indiana, USA
Prof. Richard Salant, Georgia Institute of Technology, USA
Prof. Bernd Sauer, TU Kaiserslautern, Germany
Prof. Ian Sherrington, University of Central Lancashire, Great Britain
Prof. Hugh Spikes, Imperial College London, Great Britain
Prof. Gwidon Stachowiak, Curtin University Australia, Australia
Prof. Kees Venner, University of Twente, Enschede, Netherlands
Prof. Philippe Vergne, Institut National Des Sciences Appliquées (INSA) Lyon, France
Prof. Fabrice Ville, Institut National Des Sciences Appliquées (INSA) Lyon, France
Prof. Sandro Wartzack, Friedrich-Alexander-University Erlangen-Nürnberg, Germany
Prof. John A. Williams, University of Cambridge, Great Britain
Prof. Hans-Werner Zoch, IWT Stiftung Institut für Werkstofftechnik, Bremen, Germany

Contents

Analysis of planetary bearing and gear loads of a wind turbine main gearbox on a 4 MW system test bench

C. Liewen[1], G. Jacobs[2], D. Bosse[3]

[1] *Center for Wind Power Drives, RWTH Aachen University, Christian.liewen@cwd.rwth-aachen.de*
[2] *Center for Wind Power Drives, RWTH Aachen University, Georg.jacobs@cwd.rwth-aachen.de*
[3] *Center for Wind Power Drives, RWTH Aachen University, Dennis.bosse@cwd.rwth-aachen.de*

Abstract – The majority of wind turbines (WT) worldwide have a main gearbox to increase their rotor speed [1]. With the exception of a few niche products, most gear concepts use planetary stages as the first gear stage, because of their advantages regarding power splitting, low construction volume and weight, as well as a high transmission ratio at high efficiency. Inside the planetary stage the high rotor torque of the wind turbines is distributed over several planets and reunited at the sun gear.

The rolling bearings inside a WT gearbox are the cause of about two-thirds of all gearbox damages [2] [3]. A substantial share of the downtime resulting from these damages come from the planetary bearings [4]. To increase the WT reliability and to further optimize the design of the planetary bearings a better knowledge of the resulting local loads at the planetary bearing and at the surrounding components is required. It is the aim of this paper to show the impact of planetary gear loads on the local loads of an overdetermined multi-row (4 rows) planetary bearing of a 2.7 MW research nacelle through measurements on a 4 MW system test bench. Furthermore, the procedure of estimating gear and planetary bearing load distribution from measured data is presented. The comparison of a WT operation point with 100 % pure torque with an operation point with additional non-torque loads (NTL) leads to the conclusion that during gearbox development and prototype testing, unexpected and overlooked additional bearing row loading can occur.

Keywords – wind turbine, system test bench, planetary bearing, load distribution, strain

1. Introduction

The majority of wind turbines (WT) worldwide have a main gearbox to increase their rotor speed [1]. Thereby the size and cost of the required generators can be reduced. Although gearbox damages are relatively low compared to damages of other wind turbine components, gearbox damages cause the longest downtimes [5]. Long downtimes result mainly from damages in which the complete gearbox has to be replaced for maintenance. The rolling bearings are the cause of about two-thirds of all gearbox damages [2] [3]. The most frequent reason for a gearbox replacement is a failure of the planetary bearing of the first gearbox stage [4], thus a safe design of the planetary bearings and the knowledge of the local loads plays an important role regarding the improvement of WT reliability.

A safe design of the mostly multi-row planetary bearings is hampered by a numerous number of influencing factors. The dynamic and stochastic wind loads can lead to unexpected deformations and misalignments of the planetary stage components. An uneven load distribution at the planetary gears and bearings can be the consequence.

Within the research project “Loads on the drive train components of wind turbines generators” (short name: “FVA nacelle”), a generic 2.7 MW research WT is being tested on the system test bench of the Center for Wind Power Drives (CWD) under realistic wind and grid loads. The loads at the ring gear and the sun gear as well as the loads on the planetary bearing are measured. Together with the system test bench an investigation of the impact of reproducible and adjustable wind loads in all degrees of freedom on the local loads of the gears and the planetary bearing is enabled.

In the following chapters, this paper gives a short description of the system test bench of the CWD and the device under test (DUT) with a focus on the multi-row planetary bearing. Afterwards the measurement technology for determining the local loads and the load distribution at the gears and the planetary bearing is presented. The procedure of estimating gear and planetary bearing load distribution from measured data is described. The paper ends with the presentation and discussion of the obtained results regarding the impact of planetary gear loads on the loads of the planetary bearing.

2. Test bench and device under test

2.1. 4 MW system test bench of the CWD

The wind acting on a WT is characterized by gusts and turbulences and is of a highly variable nature. Also the behavior of the electrical grid at the point of common coupling (PCC) of a WT is not predictable. If a WT and its components are to be investigated in field, this variable wind and grid conditions impede all measurements.

A remedy with a very good degree of abstraction is the 4 MW system test bench of the CWD. The test bench makes it possible to apply variable and reproducible forces and bending moments on the nacelle, thus enabling an investigation under laboratory conditions. At the test bench, weather, wind and grid conditions can be ignored and all measurements can be repeated several times with an increased number of sensors. To make this possible, the dynamic wind loads are applied by a 4 MW Direct Drive Permanent Magnet Motor (DDPM) with a maximum torque of 3400 kNm, followed by a servohydraulic, backlash-free Load Application System (LAS), connected via a clutch shaft, see Figure 1. This enables the test bench to load the nacelle in all six degrees of freedom. Thrust forces up to 4000 kN, radial forces up to 3250 kN and bending moments up to 7200 kNm can be transmitted dynamically with up to 10 Hz at the hub flange of the DUT.

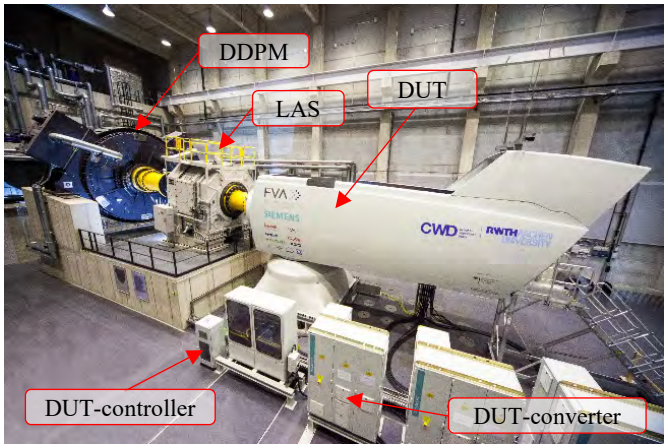

Figure 1: 4 MW system test bench of the CWD with research nacelle.

Besides, the so called "Hardware-in-the-Loop" (HiL) mode of the test bench [6] [7] [8] enables the test bench to calculate and apply the wind loads for parameters like wind speed, turbulence intensity and angle of inclined flow. Therefore the set-point value for the loads in all six degrees of freedom at the hub flange is calculated from the interaction of a stochastic three-dimensional wind field and the elastic rotor of the wind turbine in an aerodynamic model in real time.

The grid loads at the PCC are determined by a grid emulator which is based on a 17 MVA converter setup. The grid conditions at the PCC is thus also freely adjustable and the application of grid errors is possible [9]. In combination with a frequency variation between 47 Hz and 63 Hz and a short-term voltage variation between 0 % and 110 %, a realistic electric grid can be emulated and different faults and disturbances can be triggered without affecting the public grid [9].

2.2. Device under test – the FVA nacelle

The investigated DUT is based on a 2.75 MW wind turbine which has been operating near the German North Sea for approximately 12 years, see Figure 2. It has a rotor diameter of 80 m, a hub height of 60 m and a rated speed of 17.5 rpm. The WT has been rebuild to a generic research nacelle by installing new state-of-the-art components and replacing all worn parts. This includes the replacement of all gearbox bearings and the installation of new gears and shafts. The tooth flank topology of the new helical toothed planetary stage and the two new spur gears were modified at the CWD and produced in close cooperation with the German Research Association for Power Transmission Engineering (FVA), Siemens AG and further gear manufacturers involved in the research project. This makes the DUT independent of a special Original Equipment Manufacturer (OEM) and enables an open discussion about the achieved results.

The drivetrain consists of a classic, modular, three-point mounted design with a three-stage gearbox (i≈63) for a high-speed generator. A new generator, a standard asynchronous machine with a short-circuited rotor, has been installed. Figure 2 shows the FVA research nacelle in field operation prior to the modifications.

Figure 2: FVA research nacelle in field prior to project modifications.

2.3. Device under test – a multi-row planetary bearing

The first stage of the DUT gearbox is a planetary stage. The stage has three helical planets each on a multi-row planetary bearing consisting of four cylindrical roller rows, illustrated in *Figure 8*. For the design of this planetary bearing and especially for a useful lifetime approximation, one has to know the bearing loads resulting for different input loads of the wind turbine. Regarding the illustrated planetary bearing, the load distribution between the different bearing rows must be at hand. Otherwise it is not possible to make a statement on roller pressures or maximum roller forces. As also stated in [10], the gear contacts (sun-planet and planet-ring gear), especially the eccentricity of the resulting contact forces, can have a non-neglectable impact on the loads seen by the individual bearing rows. Also the tilting moments resulting from the opposite axial gear forces on to the helical planets need to be considered.

For the gears, the determination of the load distribution across the face width is state of the art and prescribed [11] for the planetary stage of a prototype gearbox for WT. For the planetary bearing, the load distribution between the bearing rows is mostly calculated/simulated. A measurement of the load distribution is not mandatory for a prototype gearbox. Regarding a determined multi-row bearing configuration (2 rows), like it is illustrated in Figure 3 [10], the calculation of the bearing row loads can be easily obtained as sufficient force / moment equilibrium equations are available. It is clear that for the illustrated configurations with different eccentricity of the resulting contact forces at the ring / sun contacts, the “One side” configuration leads to higher bearing row loads for the bearing row at the point of load application [10].

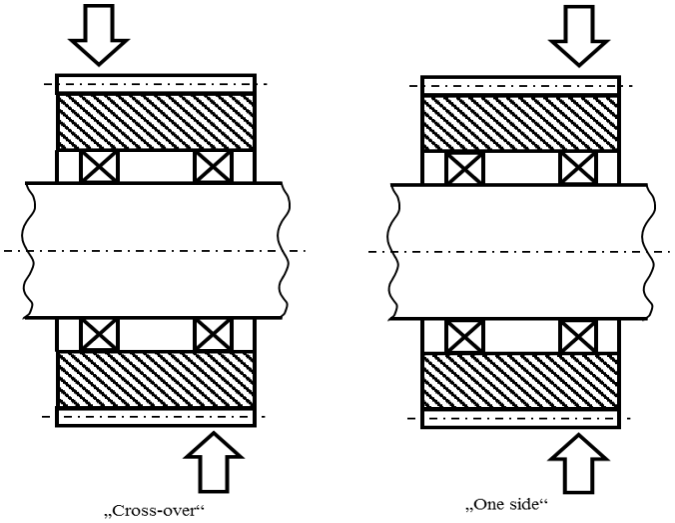

Figure 3: Two configurations of load concentration [10].

The same calculation for a planetary bearing with 4 rows leads to the finding that the system is overdetermined and a determination of the resulting bearing row loads needs simplifying assumptions (as i.e. [10], not a sufficient solution as not all influence parameters can be considered) or advanced simulation models. Validated simulation models for a multi-megawatt WT with an overdetermined multi-row planetary bearing are not publicly available, thus a safe design is difficult.

After the above considerations, it cannot be denied that the contact forces at the gears have a decisive influence on the load distribution of the bearing rows. In the following chapters, an approach to measure and analyze gear and planetary bearing load distribution is described for the presented DUT. For the gears and the planetary bearings different effects related to the load distribution will be shown based on measurement data. The dependence of the load distribution of gears and planetary bearing on the circumferential ring gear position is presented. Afterwards the impact of the load distribution of the gears on the planetary bearing row loads is analysed. Finally an operation point with pure torque (100 %) will be compared with an operation point with additional non-torque loads.

3. Measurement technology

A robust and reliable state of the art measurement technology regarding planetary bearing loads, is the load measurement with strain

gauges. For a determined planetary bearing (2 rows) it has been successfully used [12]. For a better understanding of this load measurement, a simplified FE-model of the planetary bearing with 4 cylindrical rollers pressing on one inner ring has been created, see upper half of Figure 5. The impact regarding inner ring deformation of the loaded rollers in the fit surface between inner ring and planetary bolt is illustrated. Every loaded roller on the bearing raceways generates a strained zone in the fit surface, which can be detected with strain gauges. For the calibration, the inner rings have been mounted on a supported shaft (see Figure 4) on a separate test bench. Afterwards the strain gauges of the inner rings have been loaded with a defined roller force.

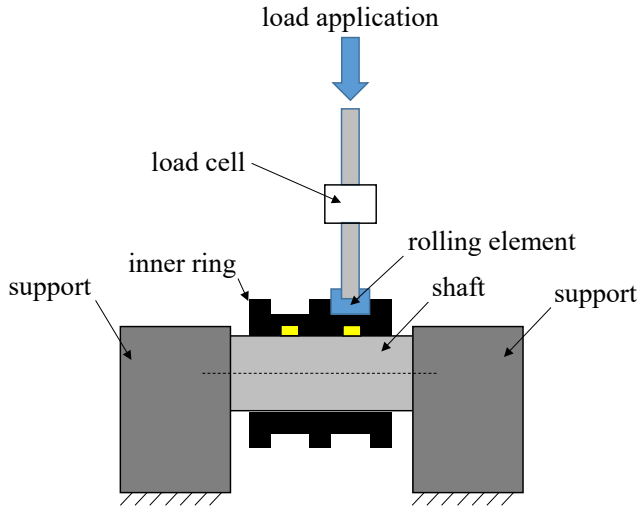

Figure 4: Calibration procedure for the bearing strain gauges.

Together with the calibration procedure carried out with defined roller forces, the measured strains allow a conclusion to be drawn in respect to the roller forces in normal operation.

To integrate the strain gauges and the needed cables, circumferential grooves (presented in lower half of Figure 5 or in Figure 6) beneath the raceways have been inserted. As the groove depth and groove width influence the resulting strains, the shown FE-model has been used to find an optimal configuration. Of course these grooves have been made as big as necessary for strain measurement, but as small as possible for a low disturbance of the system.

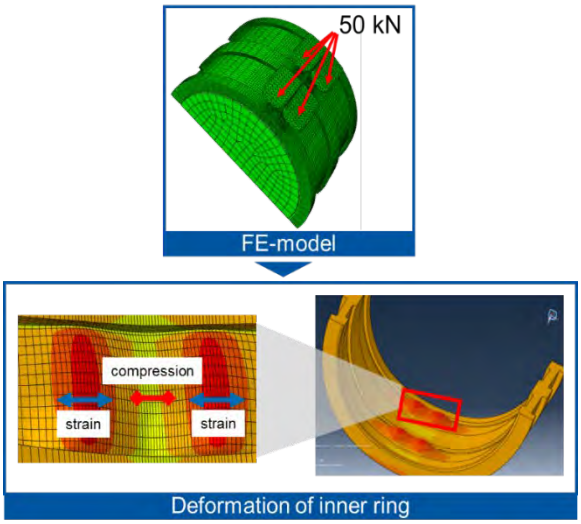

Figure 5: FE-model for the illustration of inner ring deformation.

Figure 6 shows the inner ring of the planetary bearing with the circumferential grooves as well as two out of 56 strain gauges for both bearing inner rings. The strain gauges beneath the raceway are spread over the circumferential angle of each bearing row to get a statement on the radial load distribution in the planetary shaft direction on the one hand, and on the circumferential load distribution of each row on the other hand. Since bearing ring creep between the planet shaft and the planetary bearing inner ring cannot be excluded, a feather key has been integrated to protect sensors and cables. All measuring signals located at the planetary bearing lead to rotating measurement amplifiers which are mounted at the pitch tube of the main gearbox.

Figure 6: One inner ring of the planetary bearing with circumferential grooves for the integration of strain gauges.

In each bearing row the strain gauges are connected as full bridges. The configuration leads to three measurement positions in the loaded zone of the bearing row (A, B, and C), presented in Figure 7. Position A is located where the cylindrical rollers come into the loaded zone, position B is located in circumferential direction of the planet carrier and at position C the rollers leave the loaded zone. The angle between all positions is 60°, so in total 120° of the loaded zone is covered. One of the three planets has been equipped with the described measurement technology to determine the planetary bearing loads of each row. As the equipped planet is rotating in the planetary stage, also a statement on bearing loads with regard to the ring gear circumferential angle is possible. The right side of Figure 7 is a view from the WT-rotor in downwind direction and shows the definition of the circumferential ring gear angle used in the following diagrams.

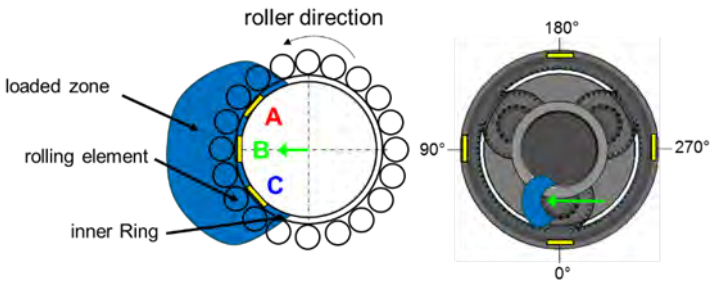

Figure 7: Measurement positions A, B and C at the planetary bearing inner ring (left) and circumferential ring gear angle (right)

The measurement positions beneath the raceways of the planetary bearing inner rings are illustrated in *Figure 8*. The bearing row numbers are used in the following diagrams. Bearing rows 1 and 2 are at the downwind and bearing rows 3 and 4 at the upwind side of the planetary stage.

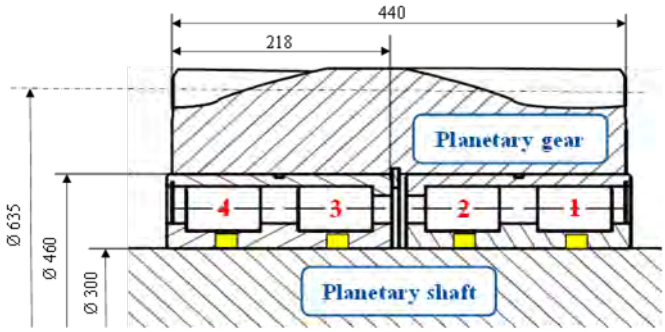

Figure 8: Multi-row planetary bearing with measurement positions (yellow squares) at the planetary bearing inner ring.

Regarding the measurement of the load distribution of the gears, strain gauge measurements at the 30° tangent to the tooth root contour. The ring gear has been equipped at four teeth (0°, 90°, 180° and 270°, see Figure 7). The sun gear has been equipped at two rotating teeth with a distance between the teeth of two tooth spaces. Each equipped tooth has six measurement positions across the face width of the loaded flank to measure tensile stresses, as you can see it exemplary for the two sun gear teeth in Figure 9. Due to the arrangement of the Wheatstone bridges at the sun gear, an opposing electrical polarity results when the teeth are engaged. When tooth 1 is engaged, a positive electrical signal and when tooth 2 is engaged, a negative signal occurs.

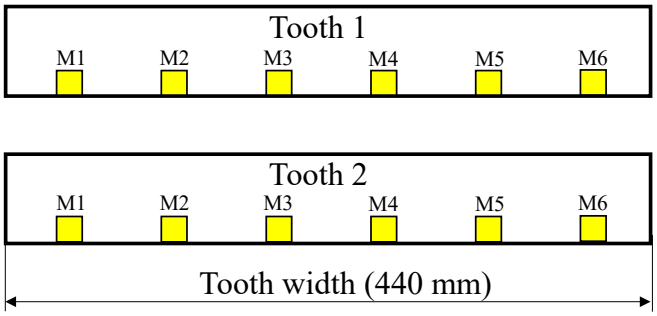

Figure 9: Six measurement positions (M1-M6) at each of the two equipped sun gear teeth.

All applied Wheatstone bridges are in full bridge configuration with temperature compensation. Despite a constant gearbox oil sump temperature of approximately 50 °C for all tests, small signal offsets occurred. These offsets have been corrected on the basis of an unloaded operation point as presented in the following chapter.

4. Data analysis – Bearing and gear loads

An extensive measurement campaign has been performed. Different tests on the one hand with a static combination of wind loads and on the other hand in HiL operation with different wind speeds and turbulence intensities have been carried out. The results presented in this paper are part of the static wind load measurement campaign. Typical time courses of rotor speed and torque for one of these tests is shown in *Figure 10*. To determine the mentioned signal offset due to temperature influence, all tests are starting with a time period in which all loads are zero (0 s to ~200 s). Afterwards the wind loads of the tested operation point have been ramped up.

Figure 10 shows that exemplary for the rotor torque (~200 s to ~410 s). At approximately 500 s the rotor speed has been ramped up to approximately 11 rpm which has been the final speed for the tested operating point. All evaluations of this paper have been performed for static wind loads and constant rotor speed to reduce complexity.

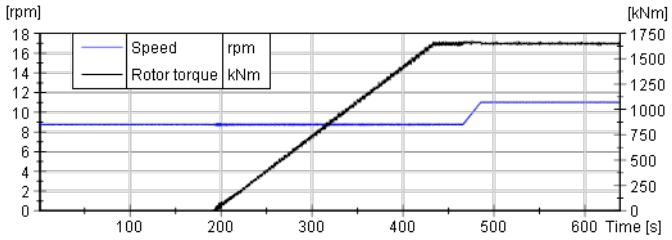

Figure 10: Typical time courses of rotor speed and torque.

In the following chapter, the offset corrected raw data of one bearing and one sun gear strain is presented and checked for plausibility. The data evaluation is presented. Regarding the gears the approach will lead to an interpretable load distribution across the face width. For the bearing rows different possible illustration forms for interpreting the load distribution between the bearing rows and also the load distribution for the circumferential bearing row angle will be shown.

4.1. Data analysis – bearing loads

Figure 11 shows the offset corrected raw data of one bearing strain. Comparing the upper diagram of Figure 11 with *Figure 10* one can see the increasing strain signal when ramping up the wind loads at 200 s. As we zoom into the evaluation range starting at 500 s (lower half of *Figure 11*) the exact curve shape can be checked for plausibility. The strain signal is constantly switching from positive to negative values. With regard to the presented FE-model (Figure 5) this is plausible: the rollers pass the measuring position and create alternatively a strained zone (roller is directly over the measuring position) and a compressed zone (measuring position is between two rollers). The occurrence of the strain peaks is in line with the theoretical cycling frequency.

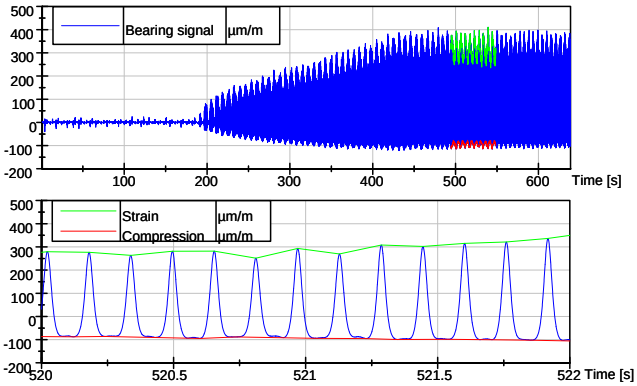

Figure 11: Time course of a bearing strain.

The strain peaks were determined with envelope curves (green and red). Afterwards all peak values have been transferred to roller forces with the calibration factor obtained for each measurement position during the calibration procedure. Regarding this application, 100 µm/m corresponds to about 10 kN roller force. For the illustration of the load distribution between the bearing rows, as the angular position of the planet carrier has been permanently tracked, the roller forces can be drawn over the circumferential ring gear angle/the position of the equipped planet inside the planetary stage, illustrated in Figure 12 for the operation point of 100 % torque (1650 kNm) without any non-torque loads (NTL). Therefore the roller forces of the measurement positions A (red), B (green) and C (blue) illustrated in Figure 12 have been averaged over 10 rotations of the planet carrier.

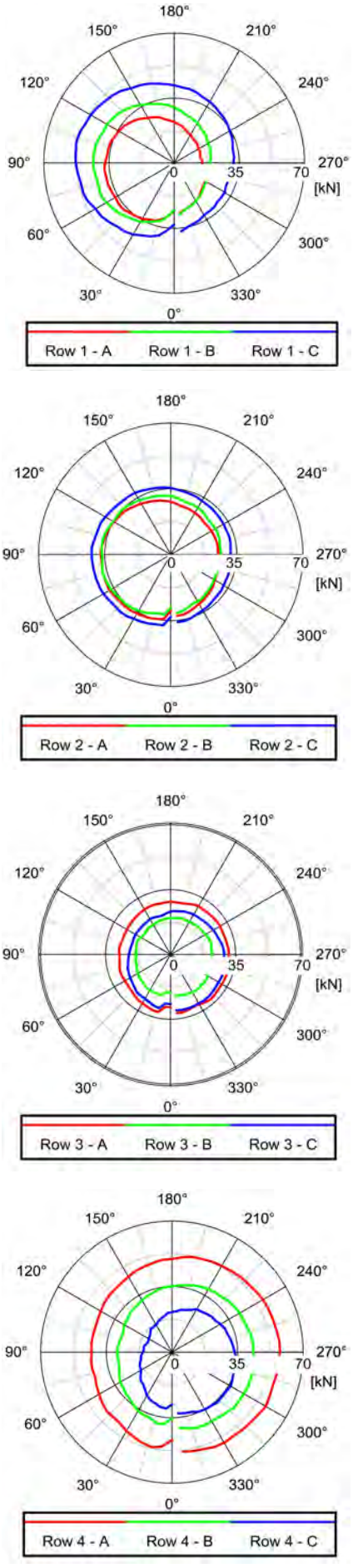

Figure 12: Roller forces (position A, B and C) over circumferential ring gear angle for all bearing rows (1-4).

Different effects regarding the load distribution of the planetary bearing can be recognized:

Different loading between all bearing rows:

The size of the circle correlates with the averaged value of roller force. As have been expected, due to the tilting moment resulting from the axial forces of the gear contact at the ring and sun gear, the circles of the outboard rows (1 and 4) are bigger, thus they experience higher forces. In this state, the bearing arrangement will suffer from inefficient use of the available material [10].

Angular movement of loading zone in planetary shaft direction:

For the comparison of the circles for one bearing row, i.e. for bearing row 4 (last diagram in Figure 12), one can notice that there is a different amount of loading for each measurement positions A, B, C. Measuring position A (red) has the highest roller loads. This effect is the other way round for bearing row 1, thus measuring position C has the highest roller loads. The reason for this is the helical planets [13]. Caused by them, the loading zone moves angularly when going along the planetary shaft direction (see Figure 13).

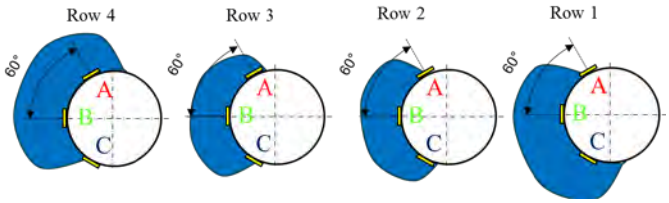

Figure 13: Schematical angular movement of loading zone in planetary shaft direction.

Uneven load distribution for ring gear circumferential position:

If the circles are concentric, an optimal load distribution in regard to the circumferential ring gear position is achieved. Bearing row 4 shows a clear shift to the 270° direction, whereas bearing row 1 has a shift to the 90° direction. This is mainly caused by the forces in the gear contacts as they strongly alternate for the circumferential ring gear position, see explanation in chapter 4.2 and Figure 15.

4.2. Data analysis – gear loads

Figure 14 shows the offset corrected raw data of two sun gear measurement positions (M1 of tooth 1 and M1 of tooth 2 in one tooth signal). Again comparing the upper diagram of Figure 14 with *Figure 10* one can see the increasing strain signal when ramping up the wind loads at 200s. Due to the arrangement of the Wheatstone bridges (see chapter 3) the positive strain values (lower half of Figure 14) have been obtained from tooth one, negative values from the second equipped tooth at the sun gear. The occurrence of the strain peaks is in line with the theoretical meshing frequencies. Again, the strain peaks were determined with envelope curves.

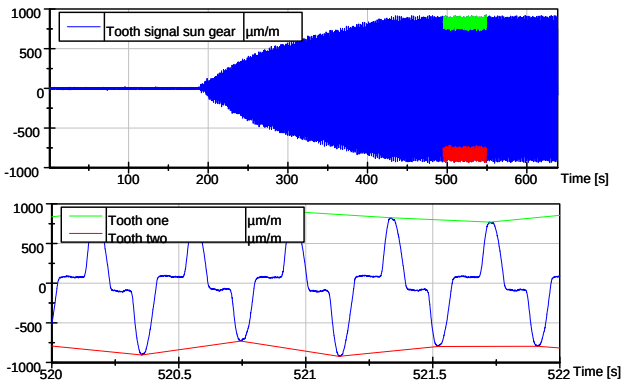

Figure 14: Time course of a sun gear strain.

As the circumferential position of the equipped sun gear teeth has been tracked, the load distribution across the face width, thus from measurement position 1 to 6, can be illustrated for the circumferential ring gear position, see Figure 15 for the operation point of 100 % torque without any NTL.

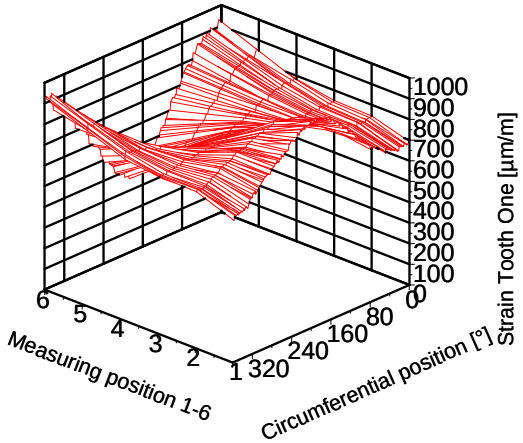

Figure 15: Load distribution across the face width of a sun tooth over the circumferential ring gear position.

One can clearly see, that the load distribution across the face width is strongly alternating over the circumferential ring gear position. For example at approximately 180° the point of load application of the resulting contact force moves to measuring point 1 (upwind position/rotorside), whereas for the 0° position the point of load application moves to measuring point 6 (downwind position/generatorside). Manufacturing tolerances of the gears, fits, bearing clearance, gear tooth modifications and the wind loads [12] can have an impact on the load distribution across the face width and consequently can be the reason for the alternating loads. Based on measurement data the impact of alternating load distribution of the gears on the planetary bearing loads is discussed in the following chapter.

5. Effect of gear loads on bearing loads

Explained for Figure 3 the eccentricity of resulting contact forces at the gears can have a significant impact on the bearing row loads. For the operation point with 100 % torque (1650 kNm) without NTL Figure 16 shows the impact for the 90° and 270° circumferential angle. The component length (abscissa of the diagram in Figure 16) starts on the upwind/rotor side (0 mm) and illustrates the width positions at the bearing rows and gears within the planetary stage. To compare the load distributions, the resulting bearing row forces have been approximated with a calculation model based on formulas of Harris/Mignot [14]. In this calculation an averaged bearing clearance (≈ 160 µm) determined from fit and inner- and outer ring temperature measurements has been taken into account. Regarding the 270°-position, the curve of the gear strains (blue and green) both have a negative gradient, so the points of load application of the resulting gear forces moved to the upwind side (to the left). The resulting bearing row forces (red) are following this trend. This behaviour nicely matches with the considerations made for the "One-side" configuration explained for Figure 3. The gradient of the sun gear strains (blue) at the 90°-position is small, whereas the gradient of the ring gear strains (green) is positive. The points of load application of the resulting gear force at the ring gear toothing moved to the right and bearing row 1 has the highest bearing row force with approximately 350 kN. On a particular note, bearing row 3 at ~175 kN has a very low bearing row force. One reason for that is clearly that the load due to the tilting moment resulting from the axial forces have smaller impact on the inboard rows. An interim conclusion is, that in respect with the load distribution of the gears, the global trend of the bearing row load distribution behaves as expected. The next chapter will show, the same comparison between gear and bearing load distribution for an operation point with 100 % torque and additional NTL.

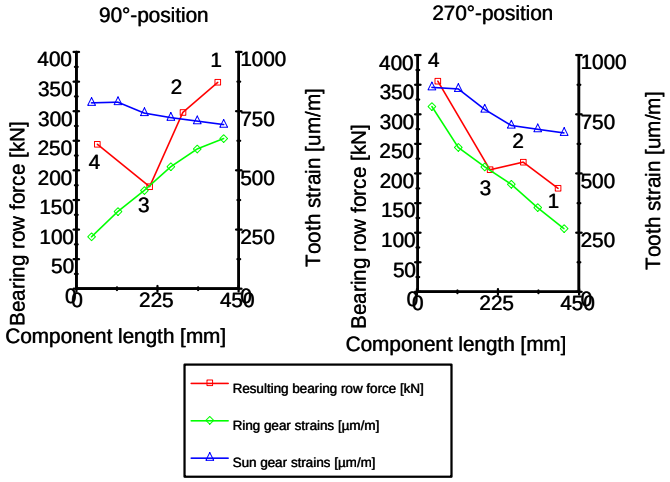

Figure 16: Effect of gear loads on bearing loads, 100% torque without NTL.

6. Effect of wind loads on gear and bearing loads

For a useful lifetime approximation of a multi-row planetary bearing one has to know the bearing loads resulting from different input loads of the wind turbine. To analyze the effect of wind loads on the bearing loads, in the following chapter a comparison between the 100% pure torque (1650 kNm) operation point and an operation point with additional NTL will be shown. An overview about the compared operation points (OP) is provided in the following Table 1.

Table 1: Overview of the compared operation points (OP)

OP	Torque (Mx)	Yaw Moment	Tilt Moment	Thrust	Shear Force	Rotor Weight
1	1650 kNm	0 kNm	0 kNm	0 kN	0 kN	0 kN
2	1650 kNm	0 kNm	500 kNm	330 kN	0 kN	-490 kN

Operation point 1 is the 100% pure torque as it has been applied to obtain the results above. For the second operation point additional static NTL in the form of a tilting moment, thrust and the rotor weight have been applied. All applied NTL are in the range of a typical loading with regards to loads at field operation, but are relatively low compared to the design loads of the gearbox. Both tests have been performed for a rotor speed of 11 rpm. Figure 17 shows that the additional NTL almost have no impact on the load distribution of the gears (blue and green curves). The deviations are in the scale of measurement inaccuracy (see error bars in Figure 17). Nevertheless an increase from ~350 kN to ~390 kN of the resulting bearing row force of row 1 is noticeable. This leads to the conclusion, that, for the shown operating point, the measured gear loads cannot explain the increase of ~10 % of the resulting bearing row force. For prototype gearboxes the measurement of the bearing row load distribution is not mandatory from the certification point of view [11] and validated simulation models for this kind of configuration barely exists. It is thus questionable if such loading conditions can be discovered during the gearbox development. Possible reasons for the increase are the misalignment and deformation of surrounding components (i.e. planet carrier, planet, planetary shaft or ring gear).

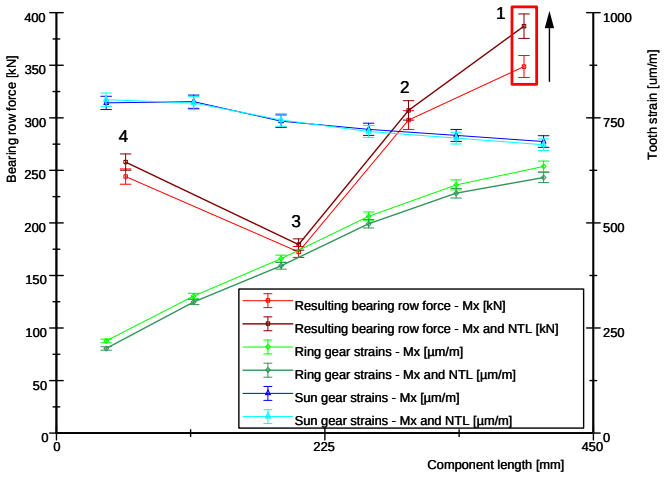

Figure 17: Effect of gear loads on bearing loads for the 90° position, comparison of 100% torque operation point (Mx) and an operation point with Mx and NTL.

7. Summary and Outlook

A substantial share of the WT downtime results from damages which come from the planetary bearings [4]. The diminished reliability causes additional maintenance costs. The presented 4 MW system test bench allows to examine the influence of wind turbine input loads on the load distribution of the planetary gears and an overdetermined multi-row planetary bearing of a multi-megawatt WT under reproducible laboratory conditions. In this paper a full approach has been shown whereby it is possible to determine the bearing loads of a multi-row planetary bearing and to correlate it with the gear and WT input loads. The effect of an alternating point of load application at the gears on the load distribution of the planetary bearings has been shown. The comparison of an operation point with 100 % pure torque with an operation point with additional NTL leads to the conclusion that during gearbox development and prototype testing, unexpected and overlooked additional bearing row loading can occur. As planetary bearings regularly fail, it is necessary to double-check whether the NTL can lead to an additional load increase on the planetary bearing which needs to be taken into account during the design process.

The shown evaluation approach has already been automated to a large extent. In the future, the quantified effect of the WT input loads on the loads of the planetary gear and bearing loads can thus be demonstrated in its entirety. In addition to the described measuring technology, further measuring signals such as the displacement and deformation of the planet carrier as well as the displacement of the planetary gear were recorded. A correlation of the input loads / local loads of gearing and bearings with the displacement and deformation states within the planetary stage is striven for. As the bearing clearance of the planetary bearing is determined from fit and inner- and outer ring temperature measurements, further investigations will show the influence on the load distribution of the planetary bearing rows.

Acknowledgment

The authors would like to thank the German Federal Ministry for Economic Affairs and Energy for the financial support of this work. They also thank the German Research Association for Power Transmission Engineering (FVA e.V.), Siemens AG, Schaeffler AG and all other companies involved in the research project.

Supported by:

Federal Ministry for Economic Affairs and Energy

on the basis of a decision by the German Bundestag

References

[1] A. Crowther et. al., Sources of time-varying contact stress and, Wiley Online Library (wileyonlinelibrary.com), (2011)

[2] K. G. Scott et al., Effects of Extreme and Transient Loads on Wind Turbine Drive Trains. AIAA Technical Conferences, Boston, University of Strathclyde, Glasgow, UK. (2013)

[3] S. Sheng: Wind Turbine Gearbox Reliability Database, Condition Monitoring, and O&M Research Update. Golden, Colorado, GRC Annual Meeting, (2015)

[4] E. Hidding: Design For Reliability. GE Renewable Energy, (2016)

[5] S. Sheng, Report on Wind Turbine Subsystem Reliability ─ A Survey of Various Databases, National Renewable Energy Laboratory (2013)

[6] C. Liewen et. al., New infrastructure and test procedures for analyzing the effects of wind and grid loads on the local loads of wind turbine drivetrain components, Proceedings of DEWEK 2015, 19/20 May 2015, Bremen, Germany, 12th German Wind Energy Conference, (2015)

[7] S.Wellenberg et. al, Real-time simulation of aeroelastic rotor loads for horizontal axis wind turbines, The Science of Making Torque from Wind 2014, [DOI: 10.1088/1742-6596/524/1/012071], (2014)

[8] U. Jassmann et. al., An Extended Inertia and Eigenfrequency Emulation for Full-Scale Wind Turbine Nacelle Test Benches, IEEE International Conference on Advanced Intelligent Mechatronics (AIM), Busan, Korea, (2015)

[9] S. Reisch et. al., Challenges and Oppertunities of fukk size nacelle testing of wind wurbine generators, Proceedings of MPT2017-Kyoto, The JSME International Conference on Motion and Power Transmissions, Kyoto, Japan, (2017)

[10] P. Flamang et. al., Stresses and load distribution factors in bearings: a tool to compare bearing alternatives, Dresdner Maschinenelemente Kolloquium, (2003)

[11] DIN EN 61400-4:2013-10, Windenergieanlagen - Teil 4: Auslegungsanforderungen für Getriebe von Windenergieanlagen (IEC 61400-4:2012); Deutsche Fassung EN 61400-4, (2013)

[12] H. Link et. al., Gearbox Reliability Collaborative Project Report: Findings from Phase 1 and Phase 2 Testing, Technical Report NREL/TP-5000-51885, (2011)

[13] W. LaCava et. al., NREL Gearbox Reliability Collaborative: Comparing In- Field Gearbox Response to Different Dynamometer Test Conditions, (2011)

[14] L. Mignot et. al., Analysis of Load Distribution in Planet-Gear Bearings, AGMA Technical Paper, (2010)

Influence of slip on the formation of White Etching Cracks on a two-disc test rig and a kinematic study on a full-scale bearing

F. Gutiérrez Guzmán[1], M. Oezel[2], J. Guenther[1], G. Jacobs[1], G. Burghardt[1], C. Broeckmann[2] and T. Janitzky[2]

[1] *Institute for Machine Elements and Machine Design, RWTH Aachen University, francisco.guzman@ime.rwth-aachen.de*
[2] *Institute for Materials Applications in Mechanical Engineering, RWTH Aachen University*

Abstract – A common cause for maintenance and downtime in multiple fields of the mechanical transmission industries are premature rolling bearing failures due to white etching cracks (WEC). This failure mode is characterized by three-dimensional cracks, bordered by regions of altered microstructure, which eventually lead to a cracking or spalling of the raceway. In a previous study, WEC tests were carried out using cylindrical roller thrust bearings. Through ultrasonic analysis, it was shown that the WEC are mainly located in the region under negative slip. In a next step, the main tribological conditions had been transferred on a two-disc test rig using inner rings from radial cylinder roller bearings. These efforts have successfully recreated WEC on a two-disc test rig under rolling contact loading without additional loading such as hydrogen pre-charging. This paper summarizes the state of the investigations regarding the influence of the slide-roll ratio (SRR) and the lubrication regime on the WEC formation on the two-disc test rig. The tests have confirmed that the WEC formation is influenced not only by the SRR, but also by the type of slip (+/-). Furthermore, the tests confirmed that a WEC failure is promoted under boundary lubrication conditions. In order to verify if high sliding conditions may occur in loaded radial roller bearings, which can be found in wind turbine gearboxes, large size roller bearing tests were conducted under transient conditions. The determined cage and roller slip provide an insight into operating conditions, which can promote the WEC formation and could be found in wind turbine gearboxes.

Keywords: Roller Bearings – Rolling contact fatigue – White etching cracks – Axial Cracks

1. Introduction

A common challenge in multiple fields of the mechanical driveline technology are premature rolling bearing failures caused by the so-called white etching cracks (WEC). This failure mode has been identified as a main failure mode in the wind energy industry and can lead to bearing failure at 5-20 % of the nominal life [1]. This damage pattern is characterized by sub-surface crack networks within regions of altered microstructure, which ultimately lead to axial cracking or spalling of the bearings raceway. These altered regions are resistant to etching and are called white etching areas (WEA) due to their white appearance under reflected light.

Although the white etching areas had been well characterized by different microscopy techniques [13, 31], the relevant drivers and formation mechanisms are still under debate. Some authors propose that the cracks are the precursor of the WEA [4, 9, 42], while other authors have suggested that the crack initiation and propagations is a consequence of the formation of WEA [2, 3, 43]. Nevertheless, this phenomenon has been considerably studied over the course of the last years and it has been found to affect different bearing types, steels and heat treatments [11]. Besides a local hydrogen ingress [30] other WEC influence factors such as lubricant composition [1, 5, 6], sliding conditions [1, 7, 8], tensile stresses [1, 9] and electrical effects [10, 41] are currently being discussed.

In order to confirm proposed influent drivers and to assess individually the influence of single contact parameters, such as the type of slip +/-, on the formation of WEC, more experimental data is needed. Experimental investigations on model test rigs offer – compared to testing on a component level – an improved control of the contact conditions. However, WEC reproduction on a model test rig without additional loading such as hydrogen pre-charging has been successful only in few instances [8, 43].

Recently, the influence of possible WEC drivers were individually tested on a four-disc test rig using specimens made from martensitic hardened 100Cr6 steel [8, 18]. The authors investigated the influence of slide roll ratio (SRR) and slip type on the formation of WEC. The rolling contact fatigue (RCF) tests showed that a WEC formation is favored by high SRRs (|30%|) and when the test roller surface velocity is higher than that of the load rings.

It is well known – that besides the continuous heathcoat slip in spherical roller and ball bearings – slip can occur in the unloaded zones of cylindrical radial bearings during operation at loads below the minimum load [1]. Furthermore, specific circumstances such as high-dynamic accelerations [14], load impacts [16] or over-lubrication [24] can also result in high SRRs at the roller-raceway interfaces. Furthermore, it has been stated that high-load and slipping conditions can occur in wind turbine gearboxes [25] during normal wind turbine operations. Recently, in studies using cylindrical roller bearings under operational conditions similar to the ones found in wind turbines, it has been proven that cage and roller slip can lead to WEC formation [24, 29]. In both studies WEC were reproduced in outer rings by combining low load conditions – and the herewith associated cage and roller slip – with high loads conditions. However, the link between field failures, testing on component level and testing on model level is still insufficient.

In recognition of this, a multi-scale approach is needed. In this work, the influence of the SRR and the type of slip (+/-) on the formation of WEC was assessed using a two-disc test rig and inner rings from radial cylinder roller bearings made of martensitic hardened 100Cr6 (1.3505 / SAE 52100) steel without an artificial hydrogen pre-charging. Within the scope of this work, microstructural analysis of the failed components were carried out in order to confirm the occurrence of the transformed microstructure associated with WEC-formation. Furthermore, the likelihood of the occurrence of highly loaded sliding conditions on a large size cylindrical radial roller bearing, which can be found in high-speed stages of wind turbine gearboxes, was investigated on a bearing test rig by measuring the load and determining both cage and roller sliding under transient conditions.

The aim of this work is to show the applicability of a two-disc test rig – using bearing components – for investigating the influence of WEC drivers individually and to give an insight into the influence of the lubrication conditions and both SRR and slip type in the WEC formation. Moreover, the experimental investigations confirm that similar sliding conditions can occur in radial cylinder roller bearings.

2. Techniques and experimental methods

2.1. Lubricants

For the tests on the two-disc test rig a mineral oil with a viscosity grade of ISO VG 100 – with a kinematic viscosity of 103.78 mm²/s at 40°C – was used. This lubricant has been used in previous studies and has led to WEC formation in a reproducible manner [12, 19]. Table 1 shows the results of the elemental composition analysis. The specific

chemical components from this off-the-shelf fully formulated gearbox oil are not publically available.

Table 1: Elemental analysis of the lubricant - Measured by ICP.

S	P	Zn	Ca	Mg
8343 ppm	512 ppm	616 ppm	39 ppm	1950 ppm

In order to investigate the kinematic behavior of radial bearings under conditions representative for wind turbine gearboxes, a fully-synthetic polyalphaolefin (PAO) oil, approved for wind turbine gearboxes, was used. This lubricant has a nominal viscosity grade 320 mm²/s at 40°C.

2.2. Two-Disc test rig

In this work, rolling contact tests were performed on a two-disc test rig (Figure 2-1), which resembles a disc-disc tribometer. Two inner rings from radial cylinder roller bearings of type NU2208-TVP2 and NU208-TVP2 both made from martensitic hardened 100Cr6 steel are used as test specimens. The freely adjustable SRR is set by varying the speed ratio of the servomotors. The static load of the rings is applied using a loading lever, which is connected both to the upper shaft and to the electrically powered load unit. The lubrication of the test specimens and the support bearings is carried out by a circulating immersion lubrication system. The oil temperature can be adjusted using an electric heater. Testing is carried out until either a predefined number of contact load cycles is reached or a vibration level, normally caused by pitting or spalling, surpasses a set threshold.

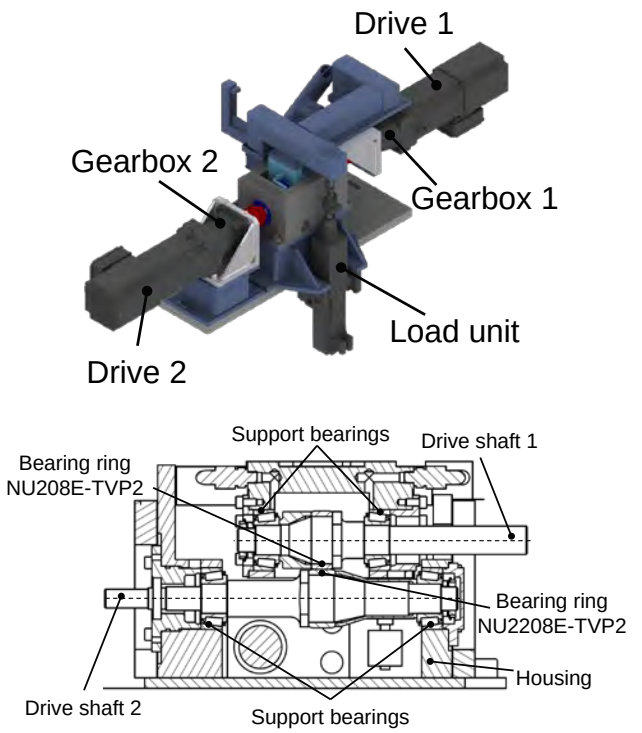

Figure 2-1: Two-Disc test rig with test rings from bearings of type NU2208 and NU208.

2.3. Radial bearing test rig

The rolling bearing measurements conducted in this study were performed using a radial bearing test rig, Figure 2-2, which is able to simulate loading conditions found in wind turbine gearboxes. The test bearing of Type NU2330-E-M1/C3 is arranged overhung and is driven by an asynchronous motor. The dynamic radial load on the bearing is applied by a hydraulic load unit, which consists of a servo-hydraulic cylinder, a load cell, control system and the required fixation components. The lubrication of the test bearing with a constant oil flow rate is carried out through a closed lubrication circuit. This arrangement allows an oil supply at a defined flow rate and the variation of the oil level and oil temperature. Furthermore, the mass temperature of the test bearing's outer ring can be adjusted using electric heaters. The rolling elements, as well as the inner and outer ring are made from typical bearing steel.

In order to accurately register the bearing's kinematic behaviour and consequently confirm the occurrence of high sliding in the loaded test bearing under transient conditions, the angular speed of the bearings inner ring (ω_{Ir}), cage (ω_C) and rolling elements (ω_R) are measured. The angular speed of the bearings inner ring is equal to the speed of the shaft and consequently of the motor. Its value can therefore, be directly obtained from the engine speed sensor. The measurement of the angular speed of the bearing cage is carried out by a fixed inductive sensor, which detects the gaps of a toothed disc (Figure 2-3) that has been attached to the bearing cage.

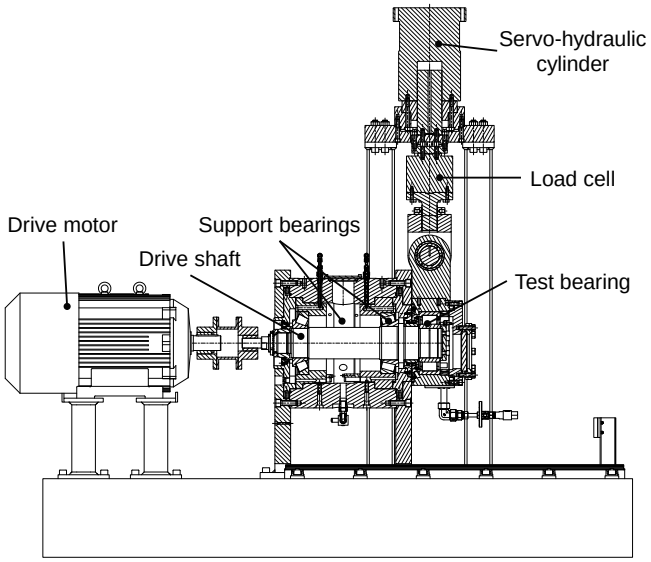

Figure 2-2: Dynamic radial bearing test rig with test bearing of type NU2330.

The measurement of the angular speed of the rolling elements takes place by measuring the voltage change in an inductive coil as a roller – with a magnet attached on its face side – rotates in operation. This measuring principle has already been successfully implemented in previous investigations [26].

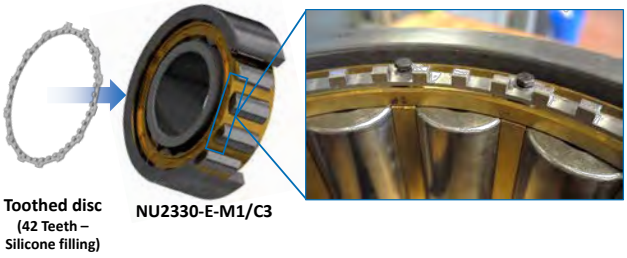

Figure 2-3: Bearing modification for the measurement of the cage speed.

2.4. Calculation methods and radial bearing kinematics

In this work, the specific lubrication film thickness λ is used as a quantitative indicator of the lubricating conditions, which prevails in the point of contact of the two-disc test rig. The λ-value, defined in Eq. 1, is determined using the lubrication film thickness h_{min} – according to DOWSON and HIGGINSON [15] – and the measured surface roughness $R_{a,1,2}$.

$$\lambda = \frac{h_{min}}{\sqrt{R_{a,1}^2 + R_{a,2}^2}} \qquad (1)$$

It has been proposed that while values of $\lambda \leq 1$ indicate boundary lubrication conditions, λ-values ≥ 3 indicate full fluid lubrication conditions [7].

It has been proved that the rolling contact fatigue (RCF) is strongly influenced by the presence of sliding [20, 21]. A criterion to describe the ratio of the sliding ($U_{sliding}$) and the rolling velocity ($U_{rolling}$) in the raceway surface is the so-called slide roll ratio (SRR), which is defined in Eq. 2.

$$SRR = \frac{U_{Sliding}}{U_{Rolling}} = 2 \cdot \left(\frac{U_1 - U_2}{U_1 + U_2}\right) \cdot 100\ \% \qquad (2)$$

Apart from conditions under pure rolling (0 % SRR) a tangential traction force is transmitted between the contact surfaces. This force is caused by the sliding friction between the contacting surfaces due to the different magnitude of the surface motion vectors. Further studies have demonstrated that the RCF is influenced not only by the magnitude but also by the direction of the tangential traction force [22]. The contact surface, which is running with the lower surface velocity – "follower" –, experiences a traction force vector in the direction of the surface motion vector. On the other hand, the contact body with the higher surface velocity – "driver" – experiences a traction force vector opposed to the direction of the surface motion vector. Previous literature [21, 22, 23] has used the terms negative slip (follower) and positive slip (driver) to describe this contact conditions.

The rolling-sliding conditions in the roller-raceway interfaces of cylindrical radial bearings are defined by the geometry of the bearing and the angular speeds of the inner ring (ω_{Ir}), the cage (ω_C), and the rolling elements (ω_R) (Figure 2-4).

In this context, a distinction should be drawn between cage and roller slip in cylindrical radial bearings (Eq. 3).

$$S_{cage/roller} = \left(1 - \frac{\omega_{Cage/roller,measured}}{\omega_{Cage/roller,nominal}}\right) \cdot 100\% \qquad (3)$$

Cage slip describes the status whereby the actual measured angular speed ($\omega_{C,measured}$) of the cage and roller assembly differ from the nominal cage angular speed ($\omega_{C,nominal}$) predicted from epicyclical considerations (Eq. 4).

$$\omega_{Cage,nominal} = \frac{\omega_{Ir}}{2} \cdot \left(1 - \frac{d_{Ro}}{d_{Ra} + d_{Ro}}\right) \qquad (4)$$

Analogous to this, roller slip describes the instance in which a roller rotates in its own axis with an angular speed lower than the one calculated by the following kinematic equation (Eq. 5).

$$\omega_{Roller,nominal} = -\frac{\omega_{Ir}}{2} \cdot \left(\frac{d_{Ra} + d_{Ro}}{d_{Ro}} - \frac{d_{Ro}}{d_{Ra} + d_{Ro}}\right) \qquad (5)$$

It has been shown that the amount of roller slip during one rotation of the cage can be described as a function of the rollers radial position [24, 25, 26]. This is explained by the fact that the radial clearance of cylindrical radial bearings leads to a formation of a load zone, which is defined, among others, by the magnitude of the applied radial load [37]. Within the load zone, the frictional drive force – applied between the rolling elements and the rotating raceway – overcomes the drag. This leads to an acceleration of the rollers until the rotational speed reaches – under ideal conditions – its nominal value. However, in some situations, the nominal value is not reached and slips between the contact surfaces can be observed [26].

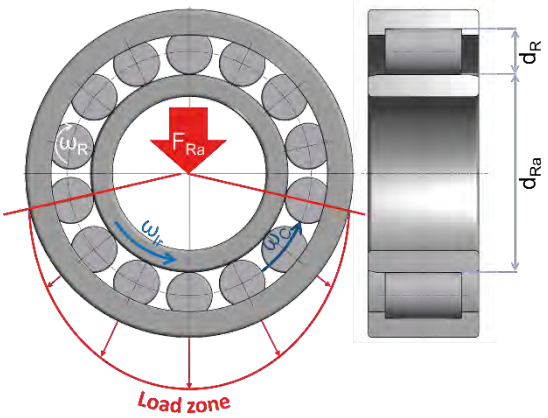

Term	Description
ω_{Ir}	Angular speed – Inner ring
ω_C	Angular speed – Cage
d_R	Diameter – Roller
d_{Ra}	Diameter – Inner ring raceway
F_{Ra}	Radial load

Figure 2-4: Load distribution and the outer raceway bearing kinematics.

The focus of this work is to verify that high sliding conditions can occur on loaded roller-raceway interfaces of a large size cylindrical radial roller bearing under transient operating conditions. Therefore, the following considerations are restricted to the sliding conditions present within the load zone. For the purpose of comparability, the SRR is used to characterize the conditions in the roller-raceway interfaces. The SRR between the rotating raceway – inner ring – and the roller is determined relative to the inner ring (Eq.6).

$$SRR = \frac{U_{Sliding}}{U_{Rolling}} = 2 \cdot \left(\frac{U_{Inner\ ring} - U_{Roller}}{U_{Inner\ ring} + U_{Roller}}\right) \cdot 100\ \% \qquad (6)$$

2.5. Two-Disc test conditions

Ultrasonic investigations on cylindrical roller thrust bearing (Type 81212) washers have been successfully implemented in order to recognize WEC at early stages [12]. Herewith it has been shown that significantly more damage could be found in the washer's inner band (blue spots, Figure 2-5). This bearing type is characterized by a SSR which increases in proportion to the distance to center of the raceway (0 % - pure rolling) and therefore, achieves it maximum (12 %) at the outermost point of the contact zone. As a criterion for prognosis of WEC location, a hypotheses based on an energetic approach has been proposed [17]. The so-called kinetic friction energy accumulation shows its maximum in region of overrolled surface, which runs under negative slip (around 8 % SRR – related to the washer) and correlates with the observed area of WEC formation.

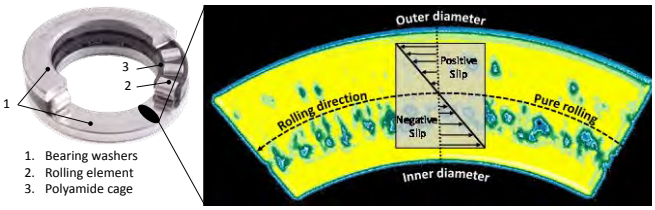

Figure 2-5: Ultrasonic measurements from part of the washer and bearings (washer) kinematics [12].

Based on these observations, eight tests were carried out in the two-disc test rig with the aim of assessing the influence of the lubrication regime and SRR on the WEC formation (Table 2). Furthermore, the kinematics of the two-disc test rig allow the assessment of the influence of the slip type on each test simultaneously.

In this work, the bearing ring NU208-TVP2 runs under negative slip – i.e. "follower" – and the bearing ring NU2208-TVP2 under positive slip – i.e. "driver". Based on previous investigations on two- and four-disc test rigs [7, 8, 18, 19], two different test series were carried out. Whereas for the first test series λ-values > 3 were chosen, the second test series was conducted under boundary lubrication ($\lambda < 1$).

The aim of the first test series was to evaluate the influence of the SRR on the formation of WEC while minimizing the amount of solid contact. Three different SRRs (0 %, 8.3 % and 12.7 %) were chosen, by taking into account the aforementioned kinematic conditions of axial thrust bearings from type 81212.

In the second test series, the lubricating conditions of previously conducted tests on axial thrust bearings from type 81212 were resembled [12, 19]. It is worth noting, that it has been stated that planet bearings, which typically also suffer from WEC, can run under low λ-values and therefore also under boundary/mixed lubrication conditions [35].

It should be noted, that the reduction of the λ-values was achieved in a first step by reducing the rotational speed of the bearing rings (tests 5

and 6) and subsequently – with the objective of reducing the test time – by pre-selecting bearing rings according to their arithmetic mean surface roughness R_a. In order to promote the WEC formation and shorten the test time, the second test series was carried out with an increased contact pressure (1.4 GPa) and oil temperature (100 °C). This approach was chosen based on reports, which propose that a high contact pressure can reduce the test time [17] – although is not necessary for creating WEC [1, 10] – and that WEC formation is favoured by temperatures in the range of 100 °C [7].

In addition to the SRRs, resulting from the axial thrust bearing's kinematics it has been proposed that transient events in wind turbine gearboxes can lead to SRRs from up to 110% [1]. Therefore, tests 6-8 were designed to simulate these conditions and were carried out with higher SRRs.

Table 2: Test conditions on two-disc test rig.

Test #	Contact Stress (Hertz)	Oil temperature	Shaft speed (NU208)	Shaft speed (NU2208)	SRR	Specific film thickness λ
1	1.2 GPa	60 °C	2200 rpm	2200 rpm	0 %	10.3
2			2024 rpm	2200 rpm	8.3 %	15.4
3			1012 rpm	1100 rpm	8.3 %	7.1
4			1936 rpm	2200 rpm	12.7 %	19.1
5	1.4 GPa	70 °C	88 rpm	100 rpm	12.8 %	0.78
6		100 °C	79 rpm	100 rpm	23.5 %	0.24
7			988 rpm	1220 rpm	21.0 %	0.72
8			1107 rpm	1287 rpm	15.0 %	0.71

2.6. Radial bearing test conditions

In order to assess the influence of transient operating conditions in the kinematic behaviour of the test bearing, the cage and roller slip under comparable stationary operating conditions must be known. Therefore, the first step was to determine both the cage and roller slip under constant load, rotational drive speed, temperature and oil level for 120 seconds. The selected conditions can be found in Table 3.

Table 3: Stationary test conditions on radial bearing test rig.

Hertzian Pressure [MPa]	850
Oil temperature [°C]	23
Shaft speed [rpm]	1500
Radial load [kN]	50
Oil level	Shaft's rotational axis

The applied load of 50 kN leads to a Hertzian pressure of 850 MPa in the inner ring and was chosen based on investigations carried out in [26] using the same test rig, bearing type and lubricant. The study showed that a load of 50 kN is required in order to achieve a cage slip of approximately 0 % under following conditions: ϑ_{oil}= 70 °C, n_{Ir} = 1500 rpm and an oil level reaching the centre line of the lowest rolling element. The bearing experiences hereby a load approximately 87 % higher than the minimum load, which is approximately 26.7 kN (according to the manufacturer's approximation formula [28]). Furthermore, it has been proposed that loads under 1000 MPa could be relevant for WEC initiation [29]. The selected rotational speed of 1500 rpm is – according to [27] – typical for bearings on high-speed shafts of wind turbine gearboxes. For the purpose of comparability with the second test under transient operating conditions, the oil was not preheated; therefore, the oil temperature at the beginning of the test is equivalent to the room temperature (approximately 23 °C). This results in an increased operating viscosity, which according to [26] increases the roller slip while decreasing the cage slip. Furthermore, the oil level was increased up to the rotational axis of the shaft (Figure 2-2). According to [26] increasing the oil level tends to increase the roller slip. Systematic investigations on the influence of the rotational speed, radial load, operating viscosity and oil level on both cage and roller slip can be found in [26]. It is well known, that slip occurs in operating points in which the radial load falls short of the minimum load, such as in wind turbines in idling operation mode [26]. Moreover, it has been suggested that a sudden engagement of the wind turbine to the electrical grid results in load ramp being applied to bearings, which are already running at synchronisation speed [26].

On the other hand, a premature engagement can lead to accelerations and decelerations processes [1]. In order to assess the likelihood of such transient speed and load operations leading to high sliding conditions under load a test cycle – consisting of one speed ramp with a subsequent load ramp – was defined as follows:

- Bearing load is held constant (50 kN).
- Inner ring rotational speed is at the beginning of the test at approximately zero.
- The cage stands almost still (~ 0 rpm).
- The bearing is accelerated with a defined speed ramp (1500 rpm at 314 rad·s^{-2}).
- Inner ring rotational speed is held constant (1500 rpm).
- Test bearing is unloaded (0 kN).
- The bearing is loaded with a defined load ramp (50 kN at 100 kN/s)

The selected conditions can be found in Table 4.

Table 4: Transient test conditions on radial bearing test rig.

	Speed ramp Step 1	Load ramp Step 2
Starting shaft speed [rpm]	~ 0	-
Final shaft speed [rpm]	1500	-
Starting radial load [kN]	-	~ 0
Final radial load speed [kN]	-	50
Ramp time [s]	0.5	0.5
Radial load [kN]	50	-
Shaft speed [rpm]	-	1500
Oil level	Shaft's rotational axis	Shaft's rotational axis

3. Results and discussion

3.1. Two Disc test

3.1.1. Experimental results

The results of the tests are shown in Table 5. The conducted tests are divided into two groups with different lubrication conditions. Test 1 through 4 were carried out with λ-values > 5 and therefore, within the full fluid lubrication regime. These tests were stopped after $40 \cdot 10^6$ cycles and showed no macroscopic signs of surface damage. Following metallographic inspections on selected test specimens showed no evidence of WEC. These results correlate with the results reported in other studies, in which a WEC formation on two-disc test rigs has not been achieved without hydrogen pre-charging [32].

On the other hand, the tests of the second test series (Test 5 through 8) were conducted under boundary lubrication conditions (λ < 1). In this test series, three rings running under negative slip (NU208) showed

spalling and one ring running under positive slip (NU2208) showed axial cracks. Figure 3-1 shows example images of surface damages. The subsequent metallographic inspections proved that the rings from test 6 and 8, which experienced negative slip, failed due to extensive white etching cracks. Although extensive serial sectioning and subsequent metallographic analysis were conducted in the ring from test 6, which experienced positive slip and failed due to axial cracks, WEC could only be found isolated and not connected to the axial crack. The similarities in the macroscopic damage pattern (Figure 3-1) lead to the assumption that test 7 failed due to WEC formation. Confirmation through metallographic investigation is, however, still pending.

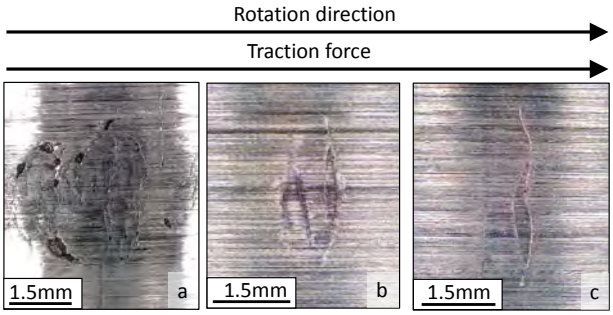

Figure 3-1: Images of the ring track for test 6 (a), 7 (b) and 8 (c).

3.1.2. Metallographic Investigations

In order to reveal the microstructure of the bearing rings used in the two-disc test rig metallographic investigations were conducted. Samples were cut from regions transverse to the over-rolling direction, in regions where a surface damage was macroscopically visible. All samples were mounted in warm embedding resin, ground and mechanically polished. Subsequently, the samples were etched in 3 % Nital solution to detect the altered microstructure associated with cracks. In addition to the light optical microscopic analysis, scanning electron microscopy (SEM) was performed to obtain detailed information about the microstructure of the white appearing areas.

White etching areas associated with cracks were found in rings running under negative slip from tests 6 and 8 (see Table 2). Figure 3-2 shows a detailed light optical microscopic image of the cross section prepared from the "follower" ring of test 8.

Large WEA/WEC networks, extending up to a depth of about 450 µm, were found below the raceway. In this particular plane, the crack network is located in the subsurface region. The orientation of the WEA/WEC is mainly parallel to the surface. Similar characteristics have been found in axial thrust bearings tested on a FE8 test rig [12]. It should be noted, that the dark appearing areas in Figure 3-2 are most likely artefacts resulting from the etchant trapped in the crack network.

Subsequent SEM investigation of the WEA marked as (a) in Figure 3-2 is shown in Figure 3-3. It can be seen, that the white etching area in this figure is concentrated at the bottom side of the crack. On this side of the crack, a breakdown of the carbide-matrix structure into a fine-grained structure (within the white appearing area) is observed. According to [31, 33, 34] diffraction patterns of areas with similar characteristics, reveals a body-centred cubic nano-crystalline ferrite structure. On the other hand, the undamaged microstructure on the upper side of the crack is characterised by a martensitic structure with chromium rich spherical carbides.

Table 5: Test results – Two-disc tests.

Test #	Load Cycles [10^6]		Surface Damage		Results from section preparation	
	Follower	Driver	Follower	Driver	Follower	Driver
1	40.9	40.9	No	No	No WEC	No WEC
2	37.6	40.9	No	No	No WEC	No WEC
3	39.3	42.7	No	No	N.A.	N.A.
4	35.5	40.3	No	No	N.A.	No WEC
5	10.5	12.0	No	No	No WEC	No WEC
6	28.5	36.1	Spalling	Axial cracks	WEC	Axial cracks + WEC
7	48.6	60.0	Spalling	No	Pending	N.A.
8	38.5	44.7	Spalling	No	WEC	N.A.

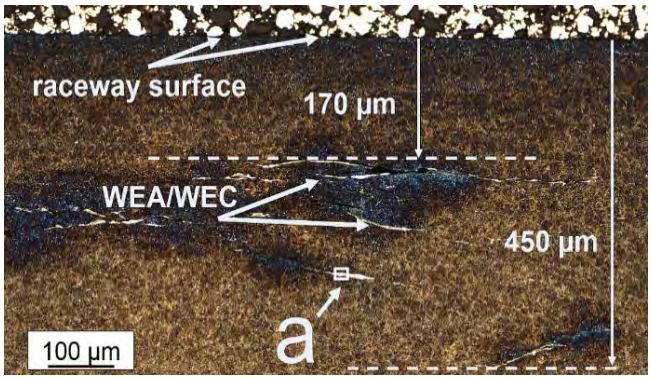

Figure 3-2: Light optical micrograph of the etched cross section prepared from the ring running under negative slip (Test 8). The plane of projection is perpendicular to the over-rolling direction.

Further detailed imaging of the WEA affected area (marked as (b) in Figure 3-3) is shown in Figure 3-4. Higher magnification of the deformed area shows that the WEA itself is not homogeneous and consists principally of two different areas with different grain size. Within the observed field, the crack seems to be bordered by a fine transformed microstructure. This area is clearly distinguishable from the underlying zone, which contains coarser grains. However, both areas appear white under reflected light, due to their etching resistance, and contain sheared and partially deformed spherical carbides.

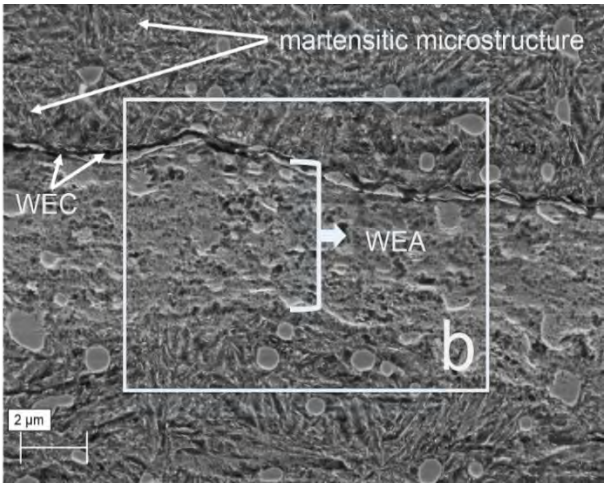

Figure 3-3: SEM investigation of the white appearing area indicated as (a) in Figure 3-2 showing the structure of the white appearing area on one side of the crack.

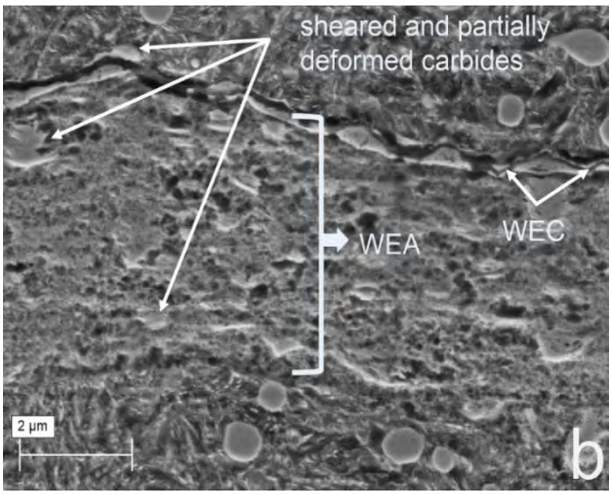

Figure 3-4: Detailed image of the area indicated as b in Figure 3-3 revealing sheared and dissolved spherical carbides within the deformed area.

3.1.3. Discussion

Rolling contact fatigue tests conducted in the two-disc test rig showed that the type of slip and the lubrication regime influence the formation of WEC. The formation of WEC was mainly observed in the raceway areas under negative slip. Metallographic investigations of the failed rings show an inhomogeneous structure of the WEA with respect to the grain size. Similar observations have been made in [2, 31]. Furthermore, SEM investigation of the WEA reveals a carbide degradation process taking place within the WEA. This is assumed to be mainly involved in the WEA formation [1, 13, 31]. It is remarkable that the nano-crystalline structure is only spreading out at one side of the crack, which is located beneath the surface. Recent SEM and TEM (transmission electron microscopy) investigations carried out in [43] support these observations.

The higher tendency towards the development of crack networks under negative slip could be attributed to two mechanism. It has been shown, that a volume element under negative slip is exposed to a higher material stress, resulting from the Hertzian pressure, the traction force and the temperature in the contact zone [23]. In addition, it is well established that negative slip favours the surface crack growth, and propagation [22, 38]. It has been shown in numerous studies that, a crack formed on the surface under negative slip grows faster than a crack formed on the surface under positive slip [21, 22, 39]. As previously described in [21], this effect can be traced back to the lubricant penetrating the crack causing a rise in the hydraulic pressure – upon a contact body entering the contact zone – and ultimately leading to a further crack growth. A detailed description of crack growth and propagation mechanisms can be found in [21, 38]. However, it should be noted that metallographic sectioning carried out in [9, 12, 27, 29, 35] has revealed strong indications for subsurface WEC initiation and propagation in some specific applications.

Furthermore, the tests running under full fluid lubrication showed no signs of WEC formation. This is consistent with experimental results on a four-disc test rig in which WEC were found on tests running under boundary lubrication (λ in the range of 0.06-0.7) [8]. Furthermore, the author suggested that under boundary lubrication conditions the extent of the WEC damage increases as the lambda value decreases. This is supported by a study providing evidence that the location of the WEC affected area in angular contact ball bearings and cylindrical roller thrust bearings correlates with local mixed lubrication [7]. The stronger development of the WEC under boundary lubrication could be attributed to two key aspects. According to [1, 17] the aforementioned observations might be consistent with hydrogen diffusion into steel, which has been confirmed as a WEC driver [1, 7, 13, 19]. It has been shown, that the decomposition of the lubricant due to catalytic reactions with nascent steel surfaces in sliding contacts can lead to the generation of atomic hydrogen [40]. In addition, the amount of generated hydrogen correlates with the amount of wear-induced nascent steel surface [40], which in a simplified approach, can be assumed to increase as the lambda value decreases [1]. A more detailed description of hydrogen absorption from the lubricant can be found in [1, 17]. Furthermore, the lubrication regime can influence the previously described mechanism of crack growth in rolling/sliding contacts. According to [21], the traction force acting on the contact surfaces is greatly reduced under full fluid lubrication. Hence, there is no significant lubricant penetration into the surface crack, limiting not only the crack propagation but also the liberation of highly diffusible hydrogen at the crack tips. However, it should be noted that WEC formation had been recently observed in cylindrical roller bearings running under full film lubrication [24].

3.2. Radial bearing test rig

The aforementioned hypotheses gives an insight into the formation of WEA/WEC under high-sliding loaded conditions, however, the question remains open whether this conditions can occur in cylindrical roller bearings and consequently in wind turbine gearbox bearings, where WEA/WEC formation had been observed. In order to give an insight into the effects of transient operating conditions in the kinematic behaviour a speed ramp and a load ramp were applied to the bearing of type NU2330-E-M1/C3.

In the first step a stationary bearing test was conducted with the objective of determining the cage and roller behaviour. As expected, the radial load within the load zone effectively develops a traction drive force between the roller and the raceway. As a result of this, the roller overcomes the drag and reaches its nominal speed i.e. minimal roller slip. On the other hand, the drag force resulting from viscous losses in the lubricant, friction between the rollers and the cage [36] and the decreasing traction force beyond the load zone leads to a deceleration of the roller and, therefore, to an increase of the roller slip up to 50 %. Figure *3-5* shows these effects as a function of the time (Figure *3-5*, top) and of the angular position of the roller relative to the shaft axis (Figure *3-5*, bottom).

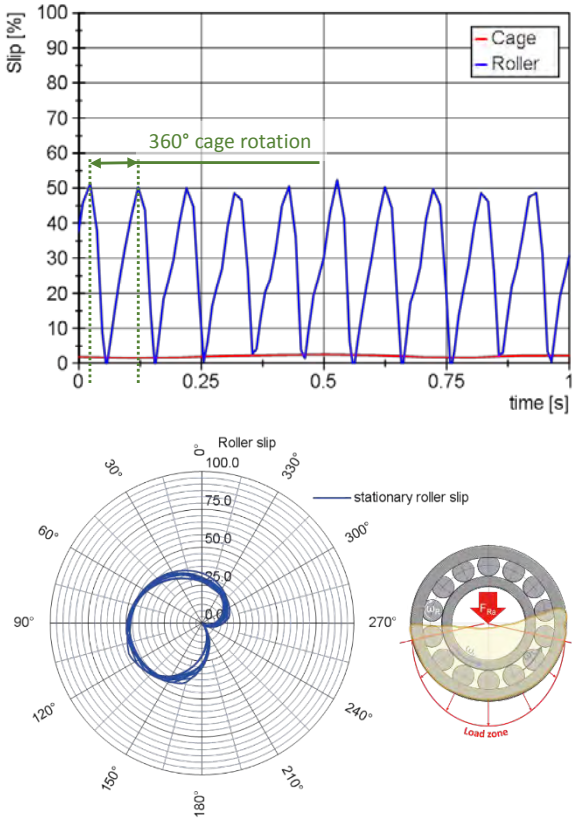

Figure 3-5: Measured cage and roller slip under stationary operating conditions.

Analogous to this, Figure 3-6 shows the kinematic response of the bearing to the speed ramp under constant load. It becomes evident that high cage and roller slip occur during and after the speed ramp.

This high-slip phase – caused by the rapid acceleration – appears in spite of the prevailing radial load of 50 kN (850 MPa). The slip state diminishes over time is, however, observable for over 10 seconds (approximately 250 shaft rotations). For the purpose of comparing the kinematic response of the roller over time, two time intervals (of one second each) of this test are plotted as a function of the angular position of the roller relative to the shaft axis (Figure 3-6 - bottom).

The first interval (green) is set about one second after the speed ramp is concluded. At this point, the roller slip varies between 50 % (86 % SRR) and 85% (157 % SRR) – within and beyond the load zone respectively – while the cage slip has a mean value of about 50%. The second time interval (orange) starts seven seconds after the speed ramp is concluded. It can be seen that the roller slip has decreased up to 25 - 70 % (38 - 120 % SRR) – within and beyond the load zone respectively.

Furthermore, Figure 3-6 shows that the angular position of the point where the minimum roller slip is achieved, changes for about 15 °. This may be due to the higher initial roller angular speed at the entry into the load zone evident from the lower roller slip, which prevails during the second interval. From this measurements, it can be concluded that the speed ramp under constant load leads to high-sliding conditions under moderate loading.

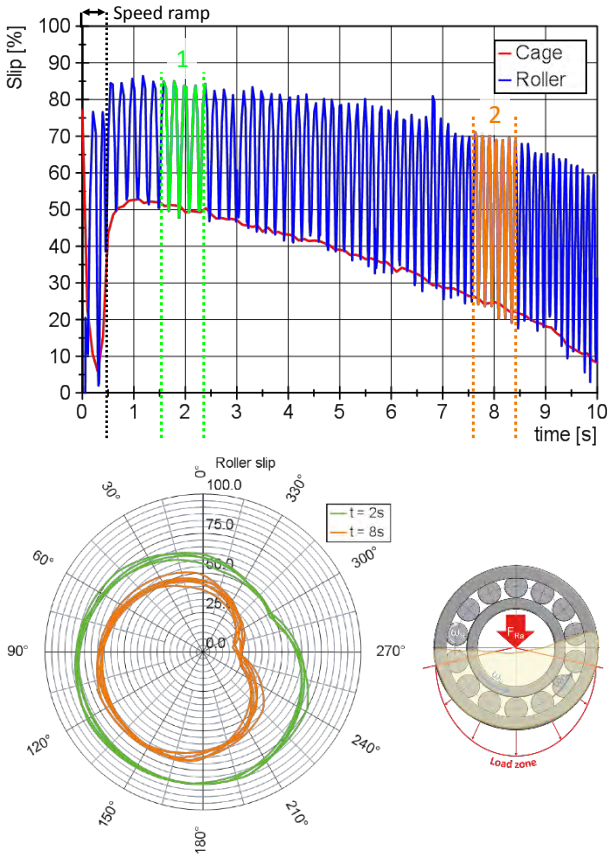

Figure 3-6: Measured cage and roller slip during and after a speed ramp.

The second step of the load cycle consists of the in section 2.6 described load ramp. The analysis of kinematic response (Figure 3-7) of the bearing is analogous to the analysis described above.

During and immediately after the load ramp high cage and roller slip can be observed. The kinematic response of the bearing is, however, significantly smoother than the one caused by the speed ramp. This state diminishes over time and after one second a quasi-stationary state is reached. At this point, the roller slip varies between 0 % and 55 % (0 - 59 % SRR) – within and beyond the load zone respectively – while the cage slip has a mean value of about 5 %. This state is comparable to the one observed under stationary operating conditions (Figure 3-5). It should be noted, that the tested bearing did not show any damages such as smearing.

The cage and roller slip measurements conducted during and immediately after the ramps indicate that under the investigated conditions, high-sliding conditions can be observed in the loaded cylindrical roller bearings. The measurements suggest that the kinematic response of the tested bearing differs according to whether a speed ramp or a load ramp is applied. In the conducted tests the speed ramp leads to a roller slip of up to 50 % – within the load zone – and a cage slip of up to 50 %, whereas the load ramp leads to a state comparable to the one observed under stationary operating conditions (roller slip of approximately 0 % within the load zone).

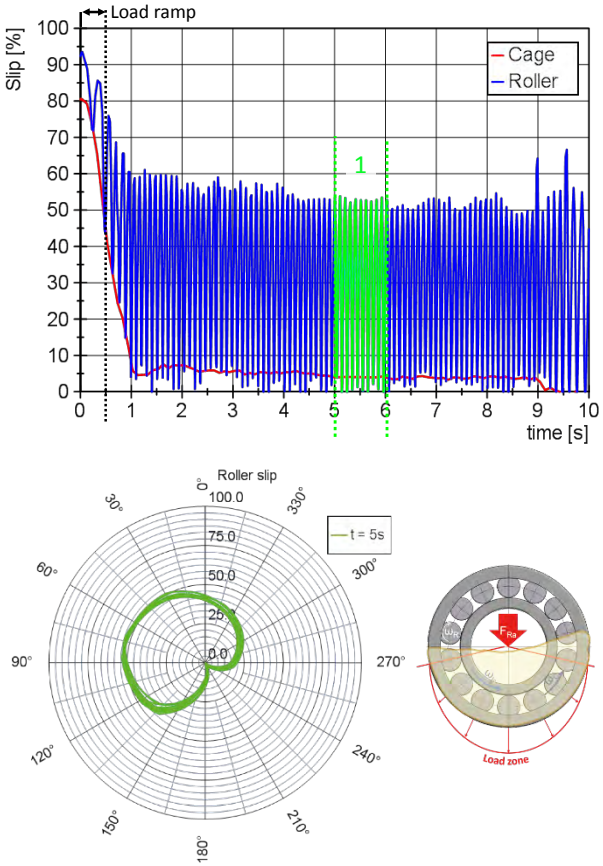

Figure 3-7: Measured cage and roller slip during and after a load ramp.

In summary therefore, it can be said that transient operating conditions can lead to high-sliding conditions in loaded cylindrical roller bearings, which could promote the WEA/WEC-formation. However, systematic investigations regarding the kinematic response of the bearing to different ramp types and the prevailing lubrication conditions still need to be conducted, particularly concerning the question which turbine operation conditions, configurations and situations can lead to critical sliding, load and lubrication conditions, which promote the WEA/WEC-formation.

4. Conclusion

This work confirms that WEC can be generated on a two-disc test rig – using bearing components – under rolling contact loading without additional loading such as hydrogen pre-charging or electric current. Following conclusions can be drawn from the conducted tests:

- The prevailing lubrication conditions during the two-disc test rig tests seem to have a dominant influence on the formation of WEC under rolling contact. Several tests performed under full fluid lubrication ($\lambda > 3$) did not show any surface or sub-surface damage after the pre-defined running times, whereas WEC formation occurred on tests running under boundary lubrication conditions ($\lambda < 1$).
- Maintaining a roughly constant SRR and increasing the λ-value from 0.2 to 0.7 leads to an increase of the running time

by 70 %. However and despite the expectations, by decreasing the SRR from 21.0 % to 15 % and maintaining the same λ-value, the running time decreased by 20 %.

- The type of slip influences the extent of the WEA/WEC damage. Test rings that experienced negative slip showed large WEA/WEC networks, which spread mainly parallel to the raceway surface. On the other hand, the rings running under positive slip showed considerably less WEA/WEC.
- SEM investigations of the WEA/WEC show inhomogeneous regions with respect to the grain size. Close-up imaging of the plastically deformed area shows sheared and partially deformed carbide precipitations within the WEA.
- The observed crack seem to be bordered with fine structure containing a distinct interface to the area with coarser grains. Furthermore, detailed imaging of the WEA shows the deformed area spreading out only at one side of the crack.

Furthermore, the observations from this work confirms that transient operating conditions can lead to sliding conditions within the load zone of large size cylindrical radial roller bearing.

- During the bearing tests, high values of cage and roller slip (up to 50 % - 85 % respectively) were achieved in the loaded bearing (850 MPa) by applying a speed ramp (314 rad·s^{-2}). The amount of cage and roller slip diminishes over time can be, however, observed over several seconds.

Although the results are yet to be confirmed statistically and further studies are needed to validate these initial observations, this work provides an insight into different WEA/WEC drivers and whether these conditions can be observed in large size cylindrical roller bearings and consequently in wind turbine gearboxes.

5. Acknowledgements

The research project FVA 707 II (IGF-Nr. 17904) was supported by the Federal Ministry of Economic Affairs and Energy (BMWi) on the basis of a decision by the German Bundestag. The authors would like to thank the *Forschungsvereinigung Antriebstechnik e.V.* for the financial support of the research project FVA 663 II and the helpful advice on the research projects FVA 707 I & II and FVA 663 II.

Supported by:

Federal Ministry for Economic Affairs and Energy

on the basis of a decision by the German Bundestag

FVA Forschungsvereinigung Antriebstechnik e.V.

6. References

[1] M. H. Evans: An updated review: white etching cracks (WECs) and axial cracks in wind turbine gearbox bearings, Materials Science and Technology 32 (2016), 1133-1169, DOI: 10.1080/02670836.2015.1133022.

[2] H. Harada, T. Mikami, M. Shibata, D. Sokai, A. Yamamoto and H. Tsubakino: Microstructural changes and crack initiation with white etching area formation under rolling/sliding contact in bearing steel, ISIJ International, 45 (2005) 1897-1902 DOI: 10.2355/isijinternational.45.1897.

[3] A. Greco, S. Sheng, J. Keller and A. Erdemir: Material wear and fatigue in wind turbine systems, Wear, 302 (2013) 1583-1591, DOI:10.1016/j.wear.2013.01.060.

[4] K. Hiraoka, M. Nagao and T. Isomoto: Study on flaking process in bearings by white etching area generation, Journal of ASTM International, 3-5 (2006) 14059, DOI: 10.1520/JAI14059.

[5] W. Holweger, M. Wolf, D. Merk, T. Blass, M. Goss, J. Loos, S. Barteldes and A. Jakovics: White etching crack root cause investigation, Tribology Transactions 58 (2014) 56-59, DOI: 10.1080/10402004.2014.942938.

[6] J. Franke, W. Holweger, H. Surborg, T. Blass, J. Fahl, T. Elfrath, T. Abe and D. Merk: Influence of Tribolayer on rolling bearing fatigue performed on a FE8 test rig, TAE 19th international colloquium tribology, Ostfildern, Germany, 2014, 1-13.

[7] A. Ruellan, F. Ville, X. Kleber, A. Arnaudon and D. Girodin: Understanding white etching cracks in rolling element bearings: the effect of hydrogen charging on the formation mechanisms, Journal of Engineering Tribology, 228 (2014) 1252-1265, DOI: 10.1177/1350650114522452.

[8] B. Gould and A. Greco: The influence of Sliding and Contact severity on the Generation of White Etching Cracks, Tribology Letters (2015) 60:29, DOI: 10.1007/s11249-015-0602-6.

[9] J. Lai and K. Stadler: Investigation on the mechanisms of white etching cracks (WEC) formation in rolling contact fatigue and identification of a root cause for bearing premature failure, Wear (2016), 364-365, 244-256, DOI: 10.1016/j.wear.2016.08.001.

[10] J. Loos, I. Bergmann and M. Goss: Influence of currents from electrostatic charges on WEC formation in rolling bearings, Tribology Transactions 59 (2016), 865-875, DOI: 10.1080/10402004.2015.1118582.

[11] K. Stadler, J. Lai J and R. H. Vegter: A review: the dilemma with premature white etching crack (WEC) bearing failures, Bearing Steel Technologies: 10th volume, Advances in Steel Technologies for Rolling Bearings (2015) 487-508, DOI: 10.1520/STP158020140046.

[12] H. K. Danielsen, F. Gutiérrez Guzmán, K.V. Dahl, Y.J. Li, J. Wu, G. Jacobs, G. Burghardt, S. Fæster, H. Alimadadi, S. Goto, D. Raabe and R. Petrov: Multiscale characterization of White Etching Cracks (WEC) in a 100Cr6 bearing from a thrust bearing test rig, Wear (2016) 370-371, 73-82, DOI: 10.1016/j.wear.2016.11.016.

[13] M.H. Evans: White Structure flanking failure in bearings under rolling contact fatigue, PhD thesis, University of Southampton, 2013.

[14] Forschungsvereinigung Antriebstechnik: *"Winkelbeschleunigung-Lagerverhalten*", Issue 637, 2015, Nr. 341 I.

[15] D. Dowson and G.R. Higginson: Elasto-Hydrodynamic Lubrication. Oxford: Pergamon Press 1977.

[16] Y.S. Kang, R.D. Evans and G. L. Doll: Roller-Raceway slip simulations of wind turbine gearbox bearings using dynamic bearing model, STLE/ASME 2010 international joint tribology conference, San Francisco, CA, USA, October 17-20, 2010, ASME, 407-409.

[17] W. Kruhöffer and J. Loos: WEC Formation in Rolling Bearings under Mixed Friction: Influences and "Friction Energy Accumulation" as Indicator, Tribology Transactions (2016), 1-14, DOI: 10.1080/10402004.2016.1183250.

[18] B. Gould and A. Greco: Investigating the Process of White Etching Crack Initiation in Bearing Steel, Tribology Letters (2016), 62: 26, DOI: 10.1007/s11249-016-0673-z.

[19] F. Gutiérrez Guzman, M. O. Oezel and P. T. Pinard: Are WECs reproducible on test benches with realistic operational conditions?, Bearing World International Bearing Conference, Hannover, Germany, 2016, 24-27.

[20] Y. Murakami, M. Kaneta and H. Yatsuzuka: Analysis of Surface Crack Propagation in Lubricated Rolling Contact, ASLE Transactions (1985), 28:1, 60-68, DOI: 10.1080/05698198508981595.

[21] M. Kaneta, H. Yatsuzuka and Y. Murakami: Mechanism of Crack Growth in Lubricated Rolling/Sliding Contact, ASLE Transactions (1985), 28:3, 407-414, DOI: 10.1080/05698198508981637.

[22] N. Soda and T. Yamamoto: Effect of Tangential Traction and Roughness on Crack Initiation/Propagation During Rolling Contact, ASLE Transactions (1982), 25:2, 198-206, DOI: 10.1080/05698198208983081.

[23] K. Sommer, R. Heinz and J. Schoefer: "*Verschleiß metallischer Werkstoffe- Erscheinungsformen sicher beurteilen*", 1. Auflage (2010), Vieweg+Teubner Verlag, Springer Fachmedien Wiesbaden GmbH 2010, ISBN: 978-3-8351-0126-5.

[24] J. Loos: Factors increasing the risk of WEC-formation in large size bearings with full film lubrication. Bearing World International Bearing Conference, Hannover, Germany, 2016.

[25] B. Gould, A. Greco and J. Keller: Investigation of bearing axial cracking: benchtop and full-scale test results. Conference for Wind Power Drives, CWD 2017, Aachen, Germany.

[26] Forschungsvereinigung Antriebstechnik: "*Schädlicher Wälzlagerschlupf*", Issue 1124, 2015, Nr. 663 I.

[27] M.H. Evans, A. D. Richardson, L. Wang, and R. Wood: Serial sectioning investigation of butterfly and white etching crack (WEC) formation in wind turbine gearbox bearings, Wear (2013), 302(1-2), 1573–1582, DOI: 10.1016/j.wear.2012.12.031.

[28] N.N.: Catalogue Large Size Bearings, Schaeffler KG; 036815632-0000/GL1/DD/2009063, 2009-11.

[29] K. Engelen, A. Kakaroglou and V. Aul: WEC reproduction on large size roller bearings. Conference for Wind Power Drives, CWD 2017, Aachen, Germany, 13-26.

[30] T. Kawamura and H. Mikami: Development of Long Life Grease NA103A for Automotive Components, NTN Technical Review (2007) vol. 75, S. 116–123.

[31] A. M. Diederichs, A. Schwedt, J. Mayer and T. Dreifert: Electron microscopy analysis of structural changes within white etching areas (2016), Materials Science and Technology, 1–11, DOI: 10.1080/02670836.2016.1139030.

[32] A. Ruellan: Tribological analysis of White Etching Crack (WEC) failures in rolling element bearings, INSA de Lyon 2014.

[33] M.-H. Evans, J. C. Walker, C. Ma, L. Wang and R. Wood: A FIB/TEM study of butterfly crack formation and white etching area (WEA) microstructural changes under rolling contact fatigue in 100Cr6 bearing steel, Materials Science and Engineering: A 570 (2013), pp. 127–134, DOI: 10.1016/j.msea.2013.02.004.

[34] A. Grabulov, R. Petrov and H. W. Zandbergen: EBSD investigation of the crack initiation and TEM/FIB analyses of the microstructural changes around the cracks formed under Rolling Contact Fatigue (RCF), International Journal of Fatigue 32 (2010) 3, pp. 576–583, DOI: 10.1016/j.ijfatigue.2009.07.002.

[35] M. H. Evans, A. D. Richardson, L. Wang, R. Wood and W.B. Anderson: Confirming subsurface initiation at non-metallic inclusions as one mechanism for white etching crack (WEC) formation, Tribology International (2014), 75, 87-97, DOI: 10.1016/j.triboint.2014.03.012.

[36] B. A. Tassone: Roller bearing slip and skidding damage, Journal of Aircraft, Vol. 12, No. 4 (1975), pp. 281-287, DOI: 10.2514/3.44445.

[37] N.N.: RKB Bearing Industries – Technical review: Machined Brass and Pressed Steel Bearing Cages: a Comparative Study, 2011.

[38] M. Kaneta and Y. Murakamit: Effects of oil hydraulic pressure on surface crack growth in rolling/sliding contact, Tribology International 20 (1987), 210-217, DOI: 10.1016/0301-679X(87)90076-4.

[39] M. N. Webster and C. J. J. Norbart: An Experimental Investigationof Micropitting Using a Roller Disk Machine, Tribology Transactions(1995), 38:4, 883-893, DOI: 10.1080/10402009508983485.

[40] M. Kohara, T. Kawamura and M. Egami: Study on Mechanism of Hydrogen Generation from Lubricants, Tribology Transactions 49 (2006), 53-60, DOI: 10.1080/05698190500486324.

[41] F. Gutiérrez Guzmán, M. O. Oezel, G. Jacobs, C. Broeckmann, G. Burghardt, and T. Janitzky: Formation of white etching cracks in oil-lubricated rolling contacts due to electric current, Antriebstechnisches Kolloquium, ATK 2017, Aachen, Germany, 27-43.

[42] J. Lai, K. Stadler and D. Vaes: Tensile stress – One root cause for bearing premture failure with white etching cracks, Antriebstechnisches Kolloquium, ATK 2017, Aachen, Germany, 15-26.

[43] S. Li, Y. Su, X. Shu and J. Chen: Microstructural evolution in bearing steel under rolling contact fatigue, Wear (2017), 380-381, 146-153, DOI: 10.1016/j.wear.2017.03.018.

An Experimental Study regarding Maintainability of a Rolling Bearing Arrangement Equipped with a Ring Lubricator for Oil Supply

Matthias Müller[1], Stephan Tremmel[2]

[1] *Engineering Design, Friedrich-Alexander-Universität Erlangen-Nürnberg (FAU)/ mueller@mfk.fau.de*
[2] *Engineering Design, Friedrich-Alexander-Universität Erlangen-Nürnberg (FAU)/ tremmel@mfk.fau.de*

Lubrication plays a decisive role in performance and operating costs of rolling bearings. Oil lubrication, which initially may be more expensive than grease lubrication, can provide longer maintenance intervals and reduce total cost of ownership, especially in case of unfavourable operating conditions. In this context, oil lubrication including a simple designed ring lubricator for oil supply, might be an economic choice for industrial operators. This paper comprises results of oil analyses obtained within a 6 000-hour long-term test featuring an oil lubricated rolling bearing arrangement equipped with a ring lubricator for oil supply. Periodically taken oil samples show changes in oil condition during the period of operation and reveal impacts on the oil caused by the ring lubricator. Crucial design criteria of a ring lubricator influencing operating characteristics of the ring and thermal behaviour of the rolling bearing are presented and evaluated regarding effects on service life of oil. Based on the data provided by the oil analyses accompanied by a final optical inspection, attainable service life of the oil is specified and compared to the relubrication interval of a grease lubricated bearing running under identical conditions. The central objectives of the presented study are to prove and quantify the benefits of using a ring lubricator in rolling bearing arrangements concerning maintainability compared to a grease lubricated rolling bearing and to identify crucial design characteristics of the ring lubricator influencing service life of the oil.

Keywords – Rolling bearing lubrication, ring lubricator, maintainability, oil sampling, oil life.

1. Introduction

Lubrication is a key factor in achieving maximum performance of rolling bearings. Merely the fact that most of the premature bearing failures are caused by incorrect lubrication points to the complexity and significance of lubrication issues. Moreover, lubrication methods influence operating characteristics and maintenance requirements [1]. Since maintenance is a cost factor it is in the operator's interest to minimise maintenance requirements.

Particularly in case of unfavourable operating conditions, oil lubrication can provide longer maintenance intervals than grease lubrication. Conditions such as high thermal loads or speed factors can significantly reduce the required regreasing interval [2] [3]. Typical applications where these conditions might occur are large electric motors which are used to drive machines such as blowers and pumps (see figure 1).

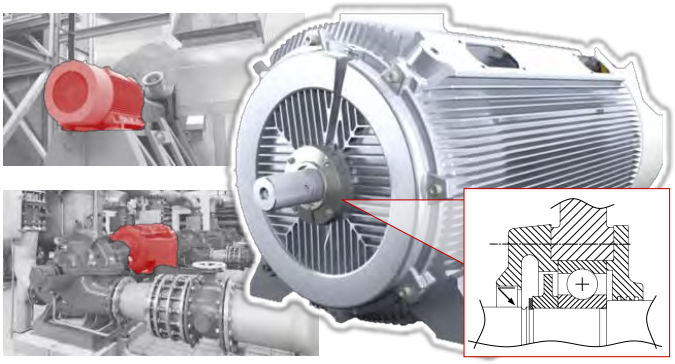

Figure 1: Exemplary range of application for large motors to drive blowers and pumps. Images kindly provided by SIEMENS AG.

In order to keep acquisition costs for the oil lubricated bearing in the range of grease lubricated bearings, the use of a ring lubricator as an oil pump is a promising option. It is characterised by a compact and simple design. Typical characteristics of oil lubrication such as cooling and purging effect and the large amount of stored lubricant suggest a longer maintenance interval to be attainable compared to grease lubrication.

The principle of ring lubricators has been known for a long time. Especially in self-contained journal bearings the ring lubricator has proven its reliability up to today [4]. Nevertheless predicting the behaviour of ring lubricators properly, especially regarding ring dynamics and oil flow, is a complex issue. This results from several design parameters influencing operating characteristics. Moreover, dynamics of oil rings used for rolling bearings react sensitively to the oil flow in the reservoir due to their low weight [5].

Some previous studies on ring lubricators dealt primarily with the potential to increase oil delivery rate for self-contained journal bearings [6] [7] [8]. However, in order to feed rolling bearings with oil, the ring lubricator requires differing operating characteristics, such as lower ring speed and lower oil delivery rates. The reasons for this are lower lubricant requirements for rolling bearings associated with the goal to maximise the service life of the oil [9].

Apart from determining suitable oil delivery rates of the oil ring another key question is, how long the attainable service life of oil operating in a rolling bearing arrangement equipped with a ring lubricator, is. Quantifying service life of the oil enables a comparison to be made with grease lubricated rolling bearings regarding maintainability. For specific applications the gathered insights support decision-making in the problem either to use grease lubrication or oil lubrication featuring a ring lubricator. Further aspects of interest are the extent to which the ring lubricator affects the service life of the oil and the mechanisms causing changes in oil condition induced by the oil ring. Answers to these questions are basic principles for improvements concerning maintainability and resource efficient use of lubricants.

In order to find answers to these questions a long-term test on a specifically designed test rig was performed. Oil samples were periodically taken from two rolling bearing arrangements running simultaneously for a 6 000 hour period. The samples were analysed concerning time-dependent oil conditions. Based on the sampling results and optical inspections at the end of the long-term test, crucial design criteria for ring lubricators and their influence on oil condition are discussed. Moreover, service life of the oil is specified and compared to the relubrication interval of a grease lubricated rolling bearing.

2. Fundamentals

2.1. Lubrication Methods for Rolling Bearings

For rolling bearings three common lubrication methods are used: Grease lubrication, oil lubrication and solid lubrication [1]. The choice which lubrication method is the most suitable depends on operating conditions and specifications. These include for example speed factor, loading, ambient temperature, contamination level, cleanliness and specified maintenance intervals [10].

Solid lubrication is intended to be used under special conditions, such as high temperatures or vacuum applications. Oil lubrication is generally used, if adjacent machine parts, for example gears, are lubricated with oil. Another reason is to use oil as a coolant to keep operating temperatures low. Grease lubrication is the most common lubrication method. About 90 % of all rolling bearings are grease lubricated [11]. The popularity of grease lubrication is attributable to its simple design and handling, exceedingly, if pre-greased bearings are

used. Furthermore grease lubricated bearings prove to be energy-efficient due to low friction torque.

However, the grease relubrication process of rolling bearings can lead to functional restrictions for the driven unit caused by security-related shutdown or reduced rotational speed to avoid churning losses and temperature rise of the bearing. Moreover, the well-known problem of overfilling with grease can lead to bearing failure [3] [12]. The relubrication process becomes more complicated, if accessibility to the bearing is limited. All of these aspects impair maintenance, reliability, and availability of the system and increase maintenance costs.

2.2. Maintenance – A Cost Factor for the Operator

Low maintenance effort plays an increasingly important role for machine operators [12]. Maintenance costs are a proportion of total cost of ownership, generated by a system during its service life. The concept of considering the entire product lifecycle including acquisition costs, operation costs, maintenance costs and disposal costs is gathered under the term "Life Cycle Costing" [13] [14]. The reason why an oil lubricated bearing may be the more economical solution under certain conditions is based on the idea to reduce maintenance costs. Although oil lubrication is characterised by higher acquisition costs due to its technical effort, lower maintenance costs can compensate for these. Hence, after a certain time of operation, total cost of ownership will reach a break-even point. Based on the schematic in figure 2, one can see that after passing the break-even point, oil lubrication is the more economical solution from the operator's point of view.

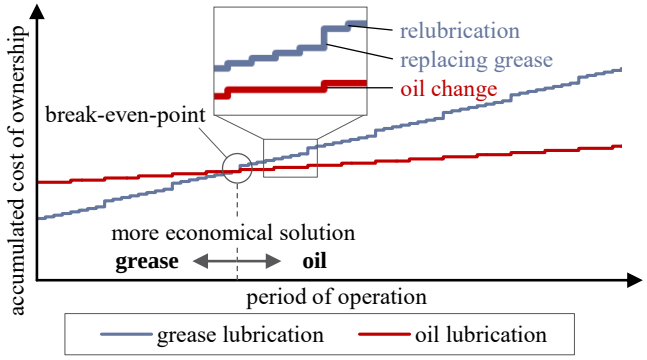

Figure 2: Simplified qualitative comparison between grease and oil lubrication concerning cost trend over period of operation.

Starting with the acquisition cost, for both lubrication methods the cost of ownership raises gradually among the period of operation. The steeper trend in the grease curve is traced back to the more frequent maintenance procedures, composed of relubrication and replacing grease. In some cases, the latter procedure is recommended in order to completely remove used grease from bearing and housing [2]. Of course, the diagram shows only one scenario amongst many. When or whether oil lubrication is the more economical solution must be assessed in each individual application depending on aspects like accessibility, personnel costs, and downtime costs of the system.

2.3. Test Bearing Arrangement

To satisfy the requirements in terms of low acquisition costs whilst ensuring long maintenance intervals, the use of a ring lubricator offers an advantageous option. It is characterised by a simple design without electric pumps and a high amount of lubricant stored in the housing.

The key components of the bearing arrangement are the rolling bearing, the shaft, the oil sump, the oil ring and the oil reservoir positioned underneath (see figure 3).

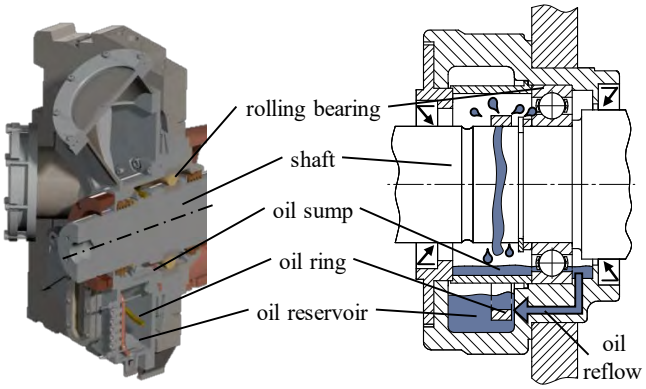

Figure 3: Prototype bearing arrangement and its design.

The ring lies loosely on the shaft and is driven by friction force as the shaft rotates. Immersing into the oil reservoir, the spinning ring delivers oil to the oil sump where the roller bearing dips in. Most of the oil reaching the oil sump adheres to the inner surface of the ring and is stripped by the shaft. Additionally, oil separated from the peripheral and lateral surfaces of the ring by centrifugal force collects partially in the oil sump. Bores in the oil sump enable the oil to reflow into the reservoir. The mode of operation can be described as combination of oil sump lubrication and circulating oil lubrication. It is characterised by continuous oil flow between the oil sump and the oil reservoir, enabling the oil to calm and to cool before recirculating.

2.4. Test Rig

In order to perform extensive experiments with the bearing arrangement, a test rig was developed. The test rig features two test bearings referred to as "test bearing I" and "test bearing II". Both test bearings are mounted on a common shaft and operate at same speed and load (see figure 4 a). A support bearing is arranged symmetrically between the test bearings impinging defined radial loads. The simulation of various thermal conditions is realised by heating elements being placed in the shaft and the bearing plate. In this way, oil viscosity as a crucial parameter influencing performance of the ring lubricator can be set. Furthermore the oil delivery rate reaching the oil sump and temperatures which are important to capture bearing performance, can be measured. Sight glasses on the bearing housings enable to analyse ring movement, oil distribution around the ring and foam generation in the oil (see figure 4 b and c).

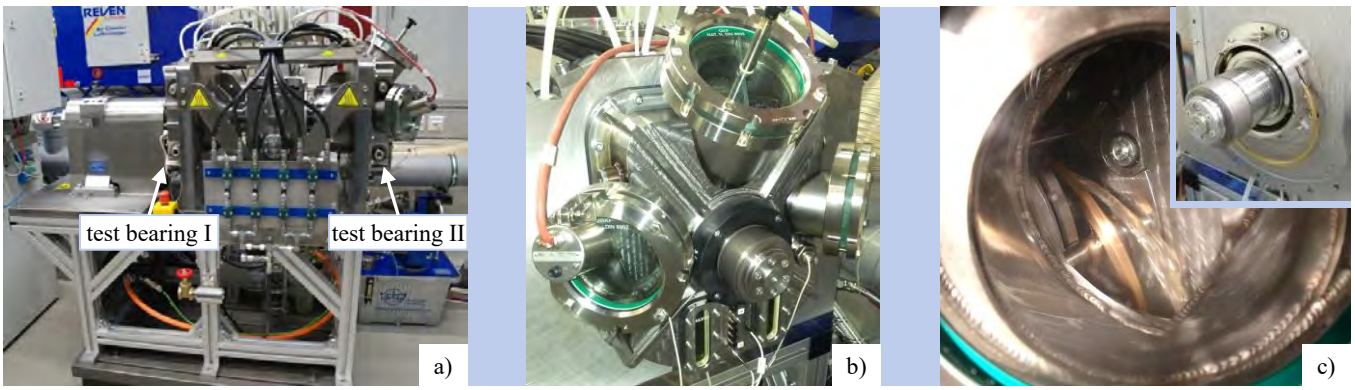

Figure 4: a) Test rig featuring two test bearings; b) Exterior view of one test bearing; c) View of the ring lubricator in operation and without front housing.

2.5. Impacts on Service Life of the Oil

The properties of oil are important for the operation of rolling element bearings. However, these properties do not remain constant in the course of service life. The oil ages due to various stresses occurring in operation. The main parameters influencing oil life are impurities, thermal stress, mechanical stress and oxidative stress. Oil conditions can be determined by means of several parameters, such as content of wear debris, additive concentration, viscosity, acid number and oxidation [15]. Typical trends of some of these parameters are shown in figure 5.

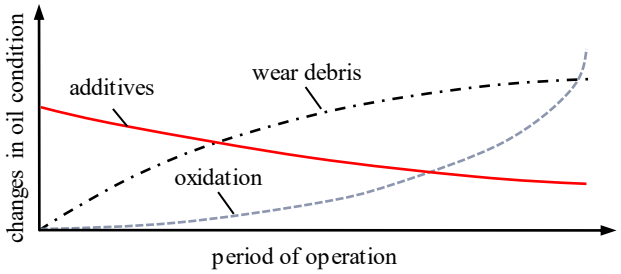

Figure 5: Trends of some parameters determining oil condition according to [15].

The parameters may influence system behaviour to a greater or lesser extent. For example, an increase of viscosity can reduce efficiency of tribological systems, whereas a decrease of viscosity may lead to damage due to insufficient lubricant film formation. Acids promote corrosion and may damage other components [16] [17].

2.5.1. How the Ring Lubricator May Affect Service Life of the Oil

In order to interpret the results obtained by the oil analyses, it is necessary to assess the potential impact the ring lubricator may have on service life of the oil. In this context, impurities, thermal stresses and oxidative stresses may be important. Mechanical stress affecting the oil condition is primarily caused by the shearing and squeezing processes occurring in the contact zones between raceways and rolling elements. By comparison, mechanical stress occurring in the contact zones of a ring lubricator is low and therefore negligible.

However, the ring lubricator may have influence on impurities due to ring wear. Oxidative stresses in terms of foam formation may be influenced by oil distribution around the ring and circulation index. Circulation index may also induce thermal stress by influencing cooling time for the oil in the reservoir. Friction and flow losses occurring in the ring-shaft and ring-oil contact zones may also affect thermal stress on the oil.

The mentioned influencing parameters are determined by operating properties of the ring. These include ring dynamics, flow formation in the reservoir and oil delivery. The properties may actually influence one another. Ring dynamics are characterised by ring speed and ring deflection. Operating properties are finally influenced by the defined specifications and the parameters set for ring lubricator design such as ring dimensions, reservoir geometry, ring immersion depth and axial ring guidance [9]. The explained causal connection concerning possible impacts on service life of the oil induced by the design parameters of the ring lubricator is illustrated in figure 6.

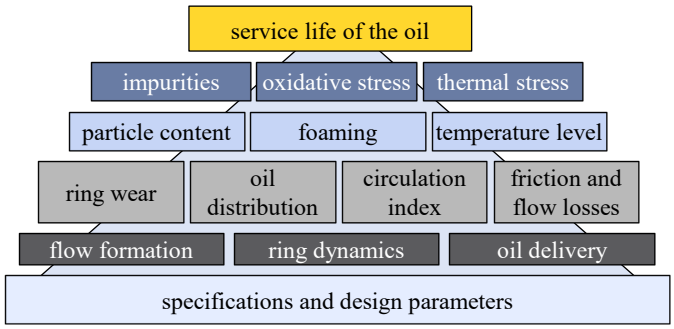

Figure 6: Parameters influencing service life of the oil using a ring lubricator.

2.5.2. Impact of Oil Delivery Rate on Thermal Behaviour

The following example clarifies the impact of the oil delivery rate of the ring lubricator on the thermal behaviour of the test bearing. The diagrammed results were obtained during preliminary tests in order to identify suitable ring dimensions for the long-term test. Figure 7 displays the oil delivery rate of two oil rings having different inner diameters (210 mm and 235 mm). Additionally, the limit of axial oil flow through the rolling bearing (6220 designation) is depicted. In order to determine the limit of axial oil flow through the bearing, software was used which has been developed within the scope of FVA project no. 474 II [18].

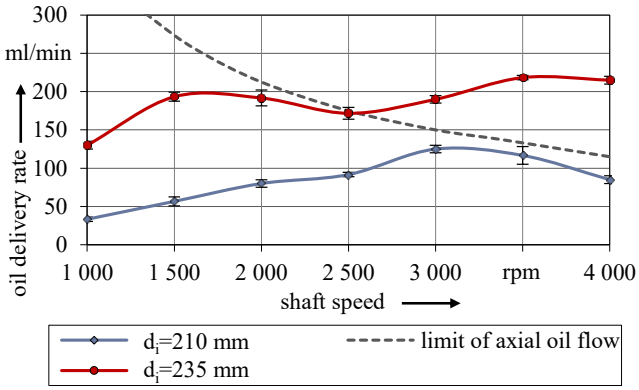

Figure 7: Comparison between two oil rings regarding oil delivery rate considering limit of axial oil flow through the rolling bearing.

The data shows an increase of oil delivery rate by using the larger oil ring by a range of 50 % to approximately 300 %. The higher oil delivery rate can be traced back to the higher ring weight causing less slip between shaft and ring and leading to higher ring speed. Figure 8 displays temperature differences between steady-state temperatures of the rolling bearing once fed with oil by the smaller ring and once fed with oil by the larger ring. For the temperature difference ΔT applies:

$$\Delta T = T_{b,d_i=235\ mm} - T_{b,d_i=210\ mm} \quad (1)$$

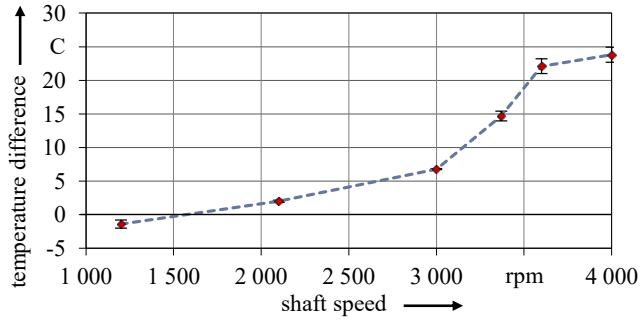

Figure 8: Measured temperature differences of the rolling bearing caused by variation of the ring inner diameter.

At lowest shaft speed, the rolling bearing fed with oil by the larger ring runs slightly cooler. The larger amount of lubricant causes more cooling performance. However, temperature differences rise with shaft speed causing the bearing fed with oil by the smaller ring to run cooler. The temperature difference even reaches up to 24 °C at maximum shaft speed. Between 3 000 rpm and 3 400 rpm there is a significant increase in temperature difference. If one compares the limit of axial oil flow through the rolling bearing with oil delivery rate of the larger ring, the reason becomes clear: From 2 500 rpm, oil delivery of the ring lubricator exceeds the limit of axial oil flow through the bearing. Consequently, the oil accumulates in front of the bearing. The immersion depth rises till reaching equilibrium of the oil delivery rate of the ring and oil flow rate through the bearing. The increased immersion depth promotes foaming and causes splashing losses which lead to an increase of bearing temperature. Both, the rise of temperature as well as foaming promote oil degradation and reduce service life of the oil.

3. Long-Term Test

3.1. Experimental Methodology

A 6 000 h long-term test was performed in order to gather insights concerning the attainable service life of the oil by using a ring lubricator and to identify design criteria influencing oil degradation.

3.1.1. Test Setup and Operating Conditions

Two different designs of the ring lubricator, which have proven to be appropriate in previous studies, were installed running simultaneously under identical operating conditions. The two designs differ concerning the way of axial ring guidance: The first design is characterised by a circumferential groove in the shaft, guiding the ring in axial direction (dynamic ring guidance). The second design contains the guiding elements as integral parts of the housing (static ring guidance). Schematics of the studied designs are shown in figure 9.

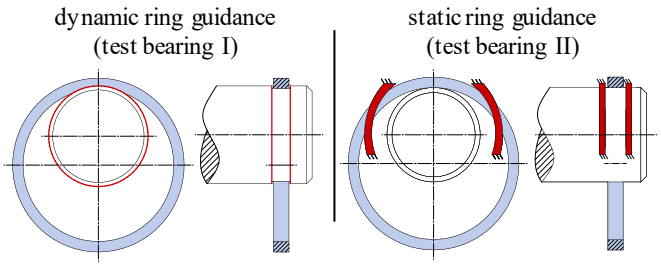

Figure 9: Studied designs for axial ring guidance concerning long-term behaviour.

Surface roughness and material of the oil rings comply with the DIN 322 standard intended for oil rings used in journal bearings [19]. Due to lower oil flow rates being required for rolling bearings, ring width was chosen to be smaller than specified in [19]. Based on the results of preliminary tests and considering manufacturing aspects, the following dimensions were chosen for both rings:
D_i x h_r x w_r = 210 mm x 6 mm x 6 mm.

Deep groove ball bearings (6220 designation) which are a common bearing type for large electric motors are used in the long-term test. The test rig operated constantly at 3 000 rpm shaft speed based on a bipolar machine connected to 50 Hz mains supply. In order to simulate the rotor weight, radial load was set to 5 kN for each test bearing. The bearing plates were heated in order to keep temperature in the load zone of both bearings constantly at 90 °C. The high temperature level promotes oil aging and enables to shorten testing time [20]. Ambient temperature varied slightly from 21 °C to 24 °C during the long-term test. Considering the used mineral oil type ISO VG 46, bearing speed, bearing temperature and bearing type, viscosity ratio equals κ = 1.2. The test setup and operating conditions for the long-term test are summarised in table 1.

Table 1: Test setup and operating conditions.

		test bearing I	**test bearing II**
test setup	ring material	brass	brass
	ring axial guidance	dynamic	static
	ring dimensions	210 x 6 x 6 mm	210 x 6 x 6 mm
	bearing type	6220	6220
	oil type	mineral oil ISO VG 46	mineral oil ISO VG 46
	oil volume	1.5 l	1.5 l
operating conditions	n_s	3 000 rpm	3 000 rpm
	F_r	5 kN	5 kN
	T_b	90 °C	90 °C
	T_a	21 °C – 24 °C	21 °C – 24 °C
	κ	1.2	1.2

3.1.2. Oil Sampling

Oil samples were taken from the oil reservoir of each bearing in a four-week interval till reaching an operating period of 4 032 h. The final sample was taken after an operating period of 6 000 h. Including a reference sample taken from the fresh oil, eight samples determine time-dependent oil condition of each bearing over the entire period of operation.

The oil was extracted using a syringe with a tube attached. Packaged and sealable sampling containers prevented contamination of the oil in the period between sampling and analysing. In order to ensure that the oil samples are comparable and representative, the oil was consistently extracted during operation and at the same position in the middle of the oil reservoir close to the oil ring and the oil reflow.

For determining oil condition, it is necessary to detect impurities and to specify the physical and chemical behaviour of the oil. The various methods which were applied to the oil samples in order to obtain the required information are listed in the following table.

Table 2: Standards and equipment used for the oil analysis.

analysis method	**parameter**	**standard**	**measuring device**
viscosimetry	kinematic viscosity	ASTM D7279	ISL Houillon Viscosimeter
emission spectrometry	element content	ASTM D5185	Optima 5300V ICP-OES
titration	neutralisation value	ASTM D974	Metohm Photometer 662
infrared spectroscopy	oxidation	ASTM E2412	PerkinElmer Spectrum One

3.2. Analysed Parameters Determining Oil Condition

The parameters in focus must be chosen according to the oil type and the materials the oil comes in contact with. In the case of the test bearings, each including a ring lubricator and mineral oil, the following parameters prove to be suitable: Wear debris, additive content, viscosity at 40 °C and 100 °C, oxidation and neutralisation number.

Composition of wear debris depends on the used components and the materials they are made of. If contained in the oil, copper, zinc and tin can clearly be assigned to the oil ring because it is made of brass. Iron indicates wear debris which may arise from the rolling bearing, the shaft surface the ring operates and the surfaces for axial ring guidance. Chrome can be assigned to the rings and the balls of the rolling bearing, which is made of 100Cr6 steel. Boron and phosphor originate from additives which are used in order to improve lubricant properties. Boron compounds serve as friction modifier when exposed to mixed friction conditions. Phosphor compounds serve as anti-wear agent by forming a wear-resistant coating on the surface [21].

Figure 10 gives an overview of the parameters which were analysed during the long-term test.

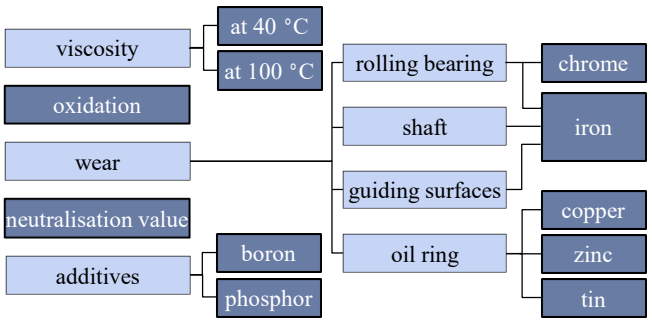

Figure 10: Analysed parameters determining oil condition.

3.3. Sampling Results

In the following, the results of the oil analyses are presented, broken down by elements indicating wear debris, additives, viscosity, oxidation and neutralisation value.

3.3.1. Wear Debris

The trends of wear debris contained in the oil of test bearing I (dynamic ring guidance) and test bearing II (static ring guidance) are shown in this section. Typical warning values* serving as references are given for each element and highlighted by means of a horizontal dashed line in the diagram. Warning values are general guiding values and certainly cannot apply to every single application, especially if dealing with prototypes. However, they provide reference values, which are obtained by thousands of samples, and support the evaluation of the oil analyses.

The following three charts show data indicating ring wear, starting with copper in figure 11, followed by tin in figure 12 and finally zinc in figure 13. Since data from the 2 016 h sample of test bearing I was implausible the values are not displayed. However, the trend of the remaining values is quite evident.

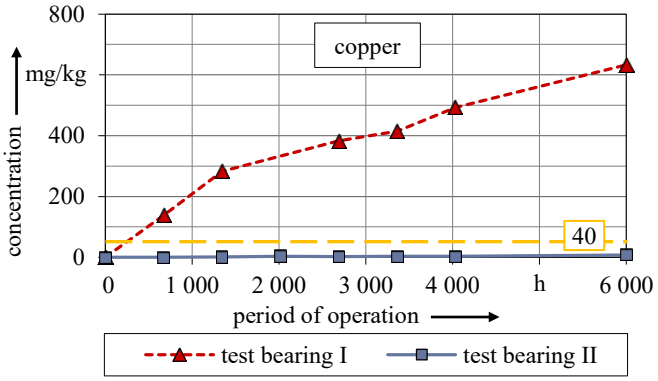

Figure 11: Copper concentration over period of operation.

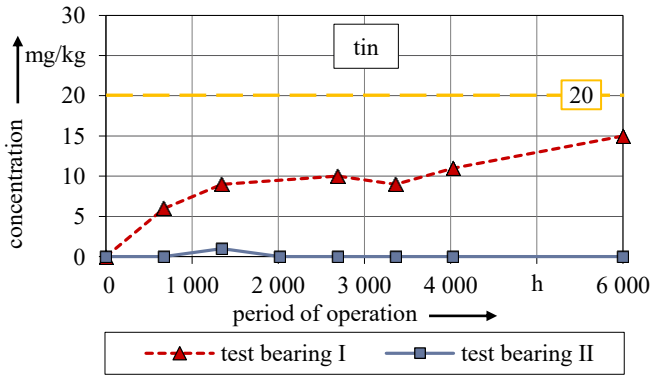

Figure 12: Tin concentration over period of operation.

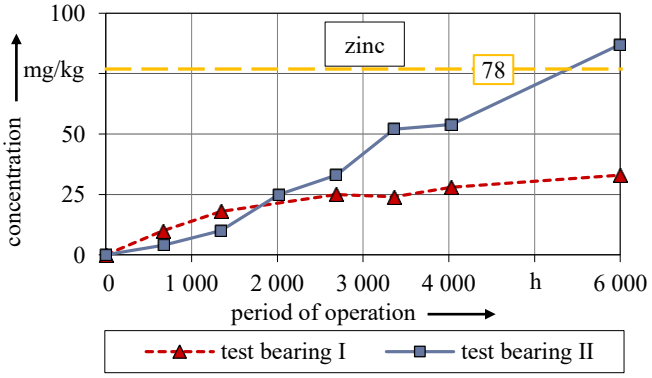

Figure 13: Zinc concentration over period of operation.

The data shows significant differences between both test bearings concerning content of wear debris. For test bearing II much lower values were measured regarding copper and tin. For each test bearing trends for copper and tin content are quite similar: For test bearing II the values nearly remain constant at a very low level, whereas for test bearing I the contents of both elements increase over time. The copper content even reaches a concentration of more than 600 mg/kg and exceeds the warning value by far.

For zinc it is the other way around: The zinc content of test bearing II even exceeds the warning value, whereas value of test bearing I remains below at approximately one third of the level of test bearing II. From the start up to a 2 000 h period of operation, trend of both test bearings is quite similar. Afterwards, the zinc content of test bearing II rises continuously, whereas the zinc content of test bearing I rises considerably slower.

The data in figure 14 shows the trend of iron content. Iron wear debris may potentially originate from the rolling bearing, the surfaces for axial ring guidance and the shaft surface.

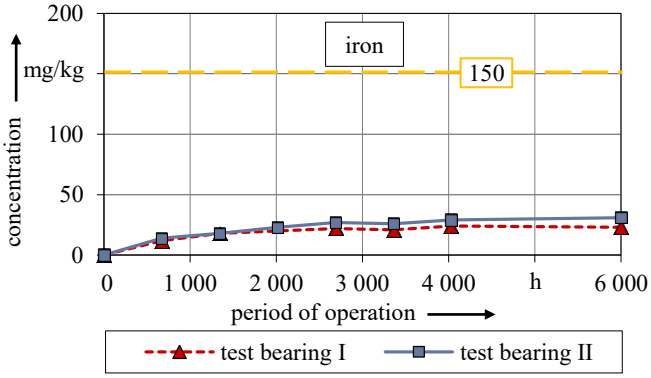

Figure 14: Iron concentration over period of operation.

The samples of both test bearings show nearly the same trend concerning iron content: The increase of concentration is less pronounced over the period of operation reaching approximately constant values towards the end of the long-term test. Both maximum values at 6 000 h period of operation are clearly below the warning value and close to each other. The accumulated value of test bearing I is 23 mg/kg, the accumulated value of test bearing II is 31 mg/kg.

As a further indication for wear debris arising from the rolling bearing, data of chrome concentration is shown in figure 15.

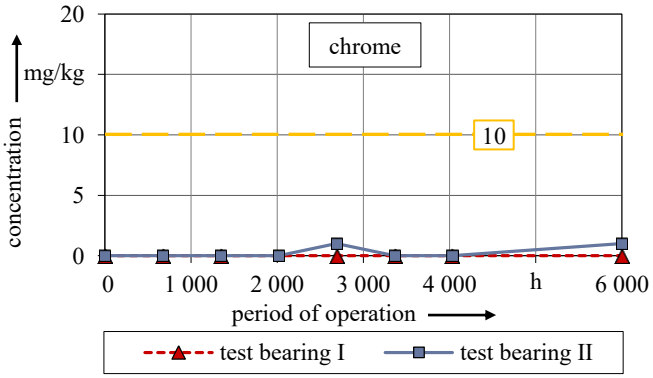

Figure 15: Chrome concentration over period of operation.

Chrome is hardly detectable in the oil of both test bearings. Values for test bearing I are zero over the entire period of operation. The maximum chrome concentration in the oil of test bearing I fluctuates between zero and 1 mg/kg and is therefore negligible.

*provided by OELCHECK GmbH

3.3.2. Additives

Data of some additive elements is shown in the following two diagrams. Figure 16 illustrates measuring data of boron.

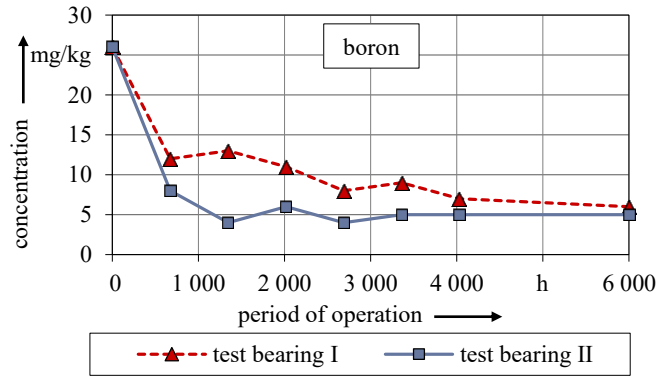

Figure 16: Boron concentration over period of operation.

At the beginning, the trend of boron content shows a major drop for both test bearings, being more pronounced in case of test bearing II. After that significant drop, the boron content of test bearing I decreases slightly. The boron content of bearing II stays nearly constant over the remaining period of operation. At the end of the long-term test values are very close to each other. In the oil of test bearing I, the boron content is reduced by about 77 %, in the oil of test bearing II the boron is reduced by about 81 % at the end of the long-term test.

Measuring data of phosphor over the period of operation is shown in figure 17.

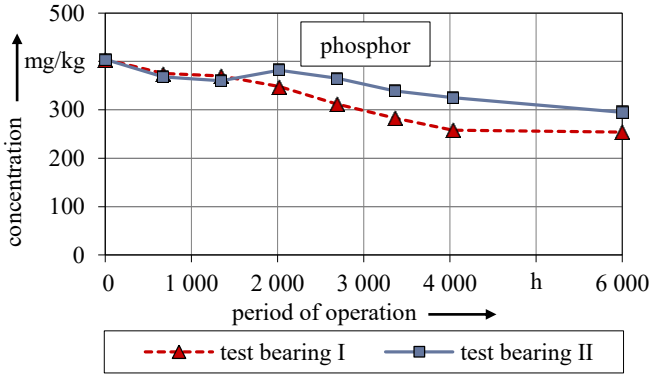

Figure 17: Phosphor concentration over period of operation.

At the end of the long-term test phosphor of bearing I is reduced by about 37 %. The reduction of phosphor content in case of bearing II is about 27 %.

3.3.3. Viscosity

In figure 18 measured kinematic viscosities are displayed at 40 °C and 100 °C.

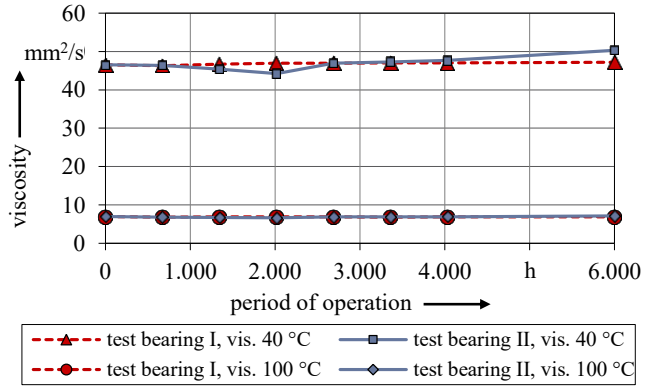

Figure 18: Viscosity over period of operation.

At lower temperature of 40 °C, changes in viscosity tend to be more volatile than at temperature of 100 °C. Table 3 gives an overview of the initial and final values of viscosity at 40 °C and 100 °C. It can be seen that the oil viscosity of test bearing II slightly increases during the long-term test.

Table 3: Changes in viscosity during the long-term test.

		test bearing I	**test bearing II**
kinematic viscosity *v* at 40°C	initial value	46.5 mm²/s	46.5 mm²/s
	final value	47.2 mm²/s	50.3 mm²/s
	change	**+1.5 %**	**+8.2 %**
kinematic viscosity *v* at 100°C	initial value	7.0 mm²/s	7.0 mm²/s
	final value	7.0 mm²/s	7.1 mm²/s
	change	**±0.0 %**	**+1.4 %**

3.3.4. Oxidation

Measured oxidation over period of operation is shown in figure 19.

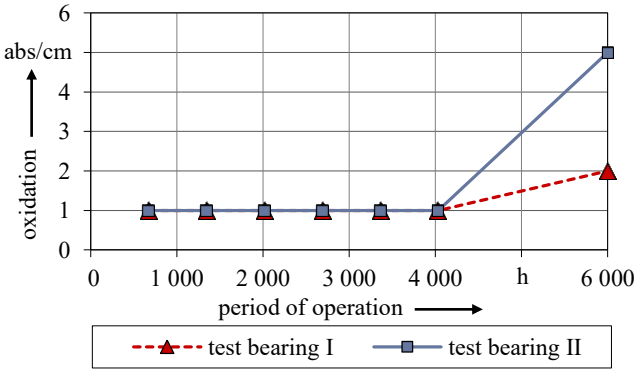

Figure 19: Oxidation over period of operation.

From the beginning up to the 4 032 h sample, the oxidation number remains constant for both test bearings. Both samples, each taken at 6 000 h period of operation, show an increase in oxidation. For test bearing II oxidation rises faster than for test bearing I. At the end of the long-term test, the value for test bearing I is 2 abs/cm. For test bearing II, it is more than twice as high (5 abs/cm).

3.3.5. Neutralisation Value

Finally, neutralisation values of both test bearings are displayed in figure 20.

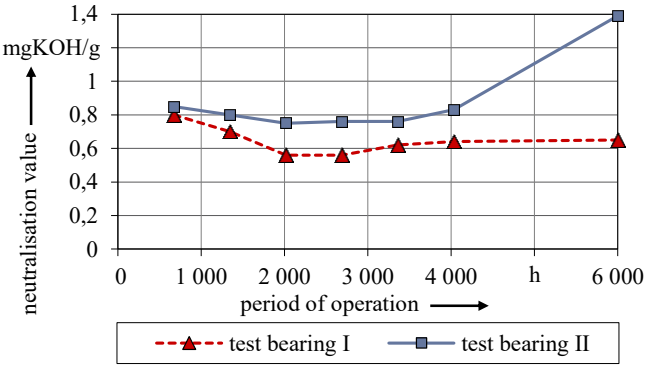

Figure 20: Neutralisation value over period of operation.

One can observe that the neutralisation value initially decreases. After a certain time remaining constant, values rise again. This U-shaped curve is typical for trend of neutralisation value [16].

However, the drop of neutralisation value for test bearing I is more pronounced than for test bearing II. Although the value for test bearing I rises again, it stays below the value of the first sample taken at 672 h period of operation. The value of test bearing II increases significantly after remaining constant for a certain time. At the end of the long-term test it is more than twice the value of test bearing I.

3.4. Discussion

In the following, the presented results are discussed. In order to evaluate the attainable oil change interval, the measured values were analysed in the context of sampling results and optical inspections.

3.4.1. Wear Behaviour

The differences in the content of copper and tin between the two test bearings are quite apparent. Respectively, the level of oil ring wear of test bearing I must be significantly higher than of test bearing II. For test bearing I, the copper content of the first sample already exceeds the warning value. At the end of the long-term test, the copper content of bearing I is about 80 times higher than of bearing II. Consequently, design of axial ring guidance has a major impact on ring wear. The results can be confirmed by means of the optical inspection, which was performed after the long-term test. The oil ring of test bearing II showed no signs of wear, whereas the oil ring of test bearing I exhibited visible traces of material loss at one of the two lateral faces. The inner and outer peripheral surfaces of both rings showed no signs of wear as well as the shaft surfaces the rings operated. The conditions occurring in the long-term test obviously promote forming of a hydrodynamic fluid film between ring and shaft. This lubricant film prevents solid contact and protects components against wear.

Zinc is detected in the oil of both test bearings. Due to the initial value of zinc being zero, it does not originate from an additive such as ZnDDP which is added to some oils in order to reduce wear [21].

At the end of the long-term test, zinc content in the oil of bearing II is more than twice as much as the zinc content in the oil of test bearing I. These sampling results initially imply ring wear in test bearing II to be higher than ring wear in test bearing I. However, these results do not correspond to the measured contents of copper and tin which contrary imply ring wear in test bearing I to be higher. The latter assumption was furthermore confirmed by the optical inspection of the oil rings: The oil ring which had run in test bearing II showed no signs of wear, revealing that zinc content in test bearing II is not caused by wearing.

Based on those findings, zinc content must arise rather from a chemical reaction than a mechanical stress. As zinc is a base metal, a chemical reaction, induced by acids, might lead to zinc measured in the oil. A similar effect is observed in [17] where zinc dissolves from a brass disc into the oil without the presence of any tribological stress.

Taking into account the measured neutralisation values, one can observe that values differ between both test bearings. Higher values imply stronger acidification and therefore a higher amount of zinc dissolving into the oil. This relation could roughly be observed in the context of the long-term test and is displayed in figure 21.

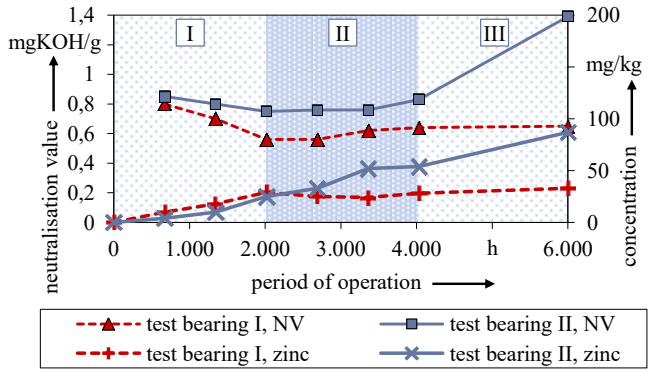

Figure 21: Neutralisation value and zinc concentration over period of operation.

In order to explain the results, the diagram is divided into three sections. From the start up to a 2 000 h period of operation, zinc contents rise likewise for both test bearings (section I). At the end of section I, the measured neutralisation value of test bearing I remains at a lower level than the neutralisation value of test bearing II. This issue influences the trends of zinc concentration in section II where neutralisation values nearly remain constant but at different levels.

Whereas the higher acidification of the oil in test bearing II provokes zinc furthermore dissolving from the oil ring, zinc content in the oil of test bearing I nearly remains at a constant level. It is expected that higher acidification results in a more pronounced dezincification.

For test bearing II the last two samples in section II (3 360 h and 4 032 h) show nearly the same zinc content leading to the conclusion that in this period of time, acidification is too low in order to furthermore dissolve zinc from the oil ring. The same applies to test bearing I from the 2 000 h sample up to the end of the long-term test as a result of the constant neutralisation value. In section III, neutralisation value of test bearing II significantly rises again. As expected, zinc content increases during this period as well.

Even though zinc as an alloy component is dissolved from the surface of the oil ring, the residual copper matrix seems to be either stable enough or so thin that it is not measurable in the oil of test bearing II.

A fundamental insight gathered during the long-term test is that the high amount of copper and tin measured in the oil of test bearing I obviously doesn't influence the wear behaviour of the rolling bearing. The same applies to the increased zinc content measured in the oil of test bearing II. Neither the oil of test bearing I nor the oil of test bearing II shows critical iron or chrome content. Iron contents of both test bearings show typical trends for content of wear debris at a low level (see figure 5). The origin of iron is probably a matter of abrasion occurring particularly on the surfaces which guide the ring in axial direction (see figure 22).

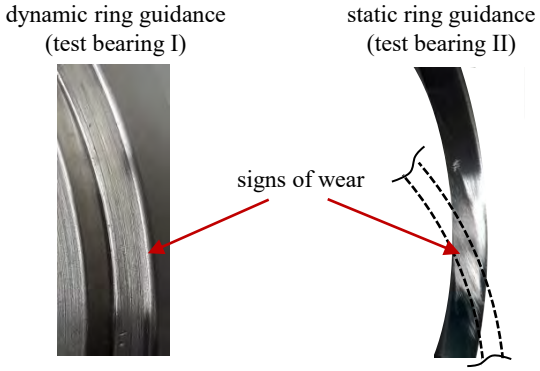

Figure 22: Signs of wear at the surfaces for axial ring guidance.

In both cases, signs of wear are weakly pronounced but visible. While in case of dynamic ring guidance, the surface tends to be polished, the surface in case of static ring guidance tends to roughen. These different wear patterns might be traced back to different lubrication conditions, caused by kinematics and relative speed between ring surface and guiding surfaces. In accordance with the amount of iron measured in the oil, the wear volume of both surfaces is similar. Consequently the design of axial ring guidance has minor impact on wear behaviour of steel components.

In contrast, the wear behaviour of the oil ring is significantly influenced by the way of axial guidance. Considering the kinematic relationship between the axial contact zones which is characterised by a superimposed radial and tangential motion, the edge of the shaft (polished area in figure 22) might strip the lubricant of the ring to a certain extent. As a consequence, solid contact and wear occurs. Considering static ring guidance, the motion between ring lateral faces and guiding surfaces is primarily characterised by a tangential motion associated with lower relative speed which reduces tribological stress in the contact.

3.4.2. Additive Decomposition

Measured contents of additives show typical trends in terms of decreasing values over period of operation. Differences between the test bearings are not significant. Percentage decrease of boron is clearly higher than of phosphor. This may be traced back to the fact that anti-wear additives require high pressures to be activated [21].

However, conditions occurring in the rolling bearings are characterised by low loads ($P/C = 0{,}04$) resulting in a small consumption of anti-wear additives. The slightly higher consumption of phosphor in case of test bearing I might be traced back to the more unfavourable contact conditions occurring in the surfaces of axial ring guidance.

Boron compounds are used for friction modifiers. This additive type forms weak bonds on the metal surface in order to improve friction behaviour in mixed friction contacts [21]. Both trends of boron content indicate that this process primarily takes place at the beginning of the long-term test. The slightly slower decrease of boron in case of test bearing I may be attributed to higher tribological stress in the axial contact surfaces of dynamic ring guidance which decelerates layer forming.

The results concerning content of wear debris of the rolling bearings indicate that additive decomposition has no influence on wear behaviour because there is no relation between additive content and wear debris visible. Naturally, the result applies to conditions which occurred during the long-term test, characterised by moderate rolling bearing load. Higher rolling bearing load would probably lead to higher additive consumption caused by higher contact stress.

3.4.3. Change of Viscosity

Change of viscosity has impact on both the performance of the rolling bearing and the performance of the ring lubricator.

An increase in viscosity results in mechanical power losses and rising temperatures occurring in the rolling bearing. If viscosity decreases, the fluid films in the contacts appearing in the rolling bearing become thinner. This situation may possibly cause damage to the rolling bearing, particularly if solid contact between bearing inner or outer ring and the rolling elements occurs [1].

In the case of the ring lubricator, viscosity influences on the one hand the lubricant film between shaft and the ring, on the other hand the thickness of the oil film adhering to the ring surface. Both aspects influence oil delivery rate of the ring lubricator as follows: The higher the viscosity is, the higher is the tangential force acting on the ring resulting in higher ring speed and, to a certain extent, higher oil delivery rate. Additionally, fluid film thickness increases with higher viscosity, also resulting in a higher oil delivery rate. In section 2.5.2 it has been shown that if oil delivery rate exceeds the limit of axial oil flow through the rolling bearing, its temperature will rise. Previous studies have shown, that under extreme conditions, roughly characterised by a temperature-induced drop of viscosity to one tenth of the nominal value at 40 °C, oil delivery rate may reach an unfavourable low level, resulting in a poor oil exchange between the oil sump and the oil reservoir [22].

However, the viscosities of the oil in both test bearings show no significant change which could result in a considerably impact on the performance of the rolling bearing or the ring lubricator. Moreover, no irregularities such as rising temperatures of the oil or the bearing could be observed during the long-term test.

Nevertheless, viscosity of the oil in bearing II increases slightly towards the end of the long-term test. This trend of an increasing viscosity is a sign of oil aging, induced by thermal oxidative stress, making oil molecules to conjoin and form molecular chains. This process of conjoining molecules obviously dominates another typical oil aging process which is characterised by a decrease of viscosity due to mechanical shearing and squeezing [16]. This issue can be traced back to the moderate mechanical load but high thermal stress occurring in the test bearings.

3.4.4. Thermal-Oxidative Degradation

The results of viscosity measurement correspond with the trends of oxidation and neutralisation number towards the end of the long-term test (see figure 19 and figure 20). Comparing values of the last two samples of test bearing II, one can see that oil oxidation and neutralisation value increase considerably due to thermo-oxidative aging. The oxidation value increases by a factor of four, the neutralisation value by a factor of approximately two. The lower oxidation and neutralisation values measured in the oil of test bearing I do not correspond to the expected trend: Due to lower ring speed in test bearing II which is caused by the additional drag force between the ring and the static guiding surface aeration in the oil and foaming are much lower compared to those observed in test bearing I (see figure 23).

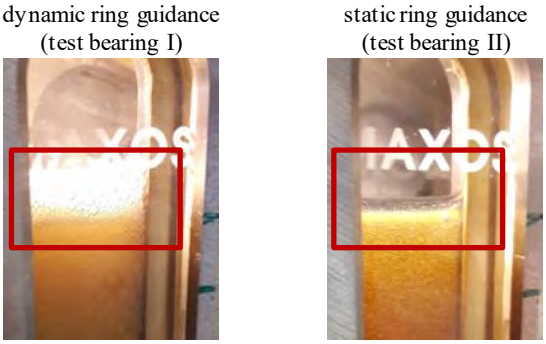

Figure 23: Comparison between test bearing I and test bearing II concerning foam formation in the reservoir.

However, foaming promotes oil oxidation. This also applies to copper which has a catalytic effect [17]. These two requirements promoting oil degradation are fulfilled for bearing I. Consequently, both oxidation and neutralisation values should be above the values of test bearing II.

Nevertheless, the inspection of the components at the end of the long-term test exhibited explicit signs of chemical and/or physical degradation processes in the oil of test bearing I. A varnish-type covering adhering to the surfaces with which the oil comes into permanent contact with was visible (see figure 24).

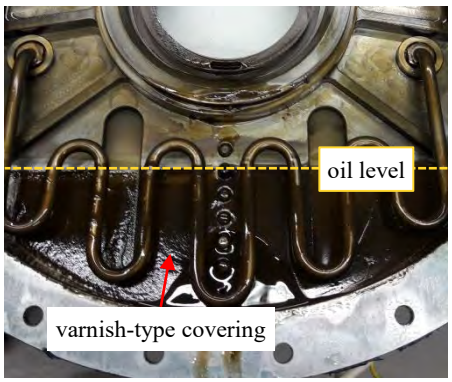

Figure 24: Coverings on the inner surface of the oil reservoir of test bearing I.

The deposit consists of several insoluble substances such as long-chained oxidation products [17]. Further constituents forming the covering may be degradation products of additives [16]. The reason why the oil samples of test bearing I do not reflect the results obtained by the inspection, cannot be clarified. It may be that precisely because the insoluble ageing products settled on the inner surface of test bearing I, they could not be proved within the oil sampling. This fact highlights that performing an optical analysis is a crucial part of assessing the oil condition.

3.5. Attainable Service Life of the Oil

3.5.1. Service Life of the Oil among Test Conditions

Due to high copper contents, the oil of test bearing I exceeded its service life at an early stage. Consequently, in order to evaluate the attainable oil change interval of a rolling bearing arrangement equipped with a ring lubricator, the focus was on the results obtained by the samples taken from test bearing II.

As mentioned in section 3.4.4, the 6 000 h oil sample taken from test bearing II yields a significant increase of oxidation and neutralisation value. However, the values haven't reached a critical level, yet.

Nevertheless there is a considerable change in oil condition. Considering the general trend of oxidation stated in figure 5, the oxidation rate is a non-linear function. Referred to the considered period of operation, predicting the future trend as well as defining a critical value for oxidation is not possible. For this purpose time-consuming experiments which take bearing failure and statistical matters into account are required. Corresponding DIN standards have already been specified for grease. These include DIN 51819 and DIN 51821.

In order to evaluate an oil change interval, neutralisation value and zinc content prove to be suitable criteria. Acidification might have impact on components such as the oil ring. As mentioned before, acidification might promote the extraction of zinc out of the oil ring material. However, the results indicate that the finely divided zinc in the oil as well as the lack of zinc in the peripheral regions of the oil ring do not have any negative impact on the bearing arrangement. According to DIN EN ISO 4263 standard, the reference value of 2.0 mgKOH/g is specified, in order to determine oil oxidation life characteristics. However, at the end of the long-term test, the neutralisation value is 1.4 mg KOH/g and therefore still beyond that reference value.

Nevertheless, acidification due to thermal-oxidative aging is intended to be the determining criterion regarding the attainable oil change interval. Since the acid products of oil degradation influence the zinc content and maybe further components possibly being used in future applications such as gaskets and sealing compounds, warning value of zinc (see figure 13) is used, in order to attain a conservative approach concerning service life of the oil. According to the measured data and the conditions in terms of the long-term test, the resulting oil change interval is therefore specified with 5 000 h.

3.5.2. Scenarios Influencing the Specified Service Life of the Oil

Since thermal degradation is the determining criterion for attainable service life of the oil, general limits for the oil life of mineral and synthetic oil are shown in figure 25.

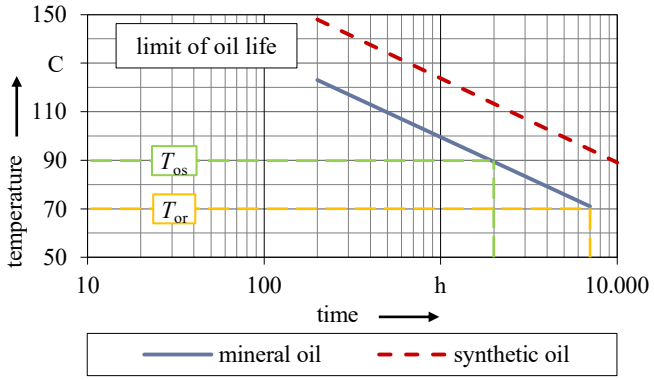

Figure 25: Limits of oil life for mineral and synthetic oils according to [23].

As mentioned in section 2.3, the test bearing features two zones containing the oil: The oil sump where the bearing dips in and the oil reservoir the oil ring immerges. In order to determine the service life of the oil in the test bearing, oil temperatures and oil volumes in both zones have to be considered. The oil temperatures measured during the long term test as well as the volume ratio are shown in table 4.

Based on these values, the combined oil life in the test bearing is calculated considering the conditions occurring during the long-term test. The combined oil life value includes retention time of the oil in each zone.

Table 4: Values determining combined oil life under the conditions occurring during the long-term test.

	oil sump	**oil reservoir**
oil temperature	90 °C	71 °C
oil life	2 000 h	7 000 h
volume ratio	1 : 36.5	
combined oil life	6 867 h	

The value of combined oil life shows that due to the high volume ratio, oil life primarily depends on the temperature in the oil reservoir. Since the oil reservoir is placed at a certain distance to the rolling bearing and the bearing plate, oil temperature in the reservoir is significantly lower than in the oil sump. If the acidification of the oil had not caused zinc dissolving from the ring, service life of the oil in the test bearing II would probably have equaled combined oil life and consequently attain approximately 7 000 h.

As stated in figure 25, oil life will be halved if temperature rises by 10 K. The principal validity of this empirical formula has already been confirmed in several studies, e. g. [16] [17]. As mentioned, the long-term test has been performed with heated bearing plates. Assuming 10 °C lower oil temperature and weakened acidification, service life of the oil may even attain 10 000 h. As stated before, oil temperature in the reservoir has no major influence on combined oil life providing that oil temperature doesn't exceed limit temperature of the oil. If ambient conditions provide clean and dry environment so that thermal-oxidative aging is the limiting factor, service life might rise furthermore by using a synthetic oil (see figure 25).

3.6. Comparison with a Grease Lubricated Rolling Bearing

The before specified service life of the oil is now compared with the specified relubrication interval of a grease lubricated roller bearing running under identical conditions. The calculation was performed using SKF BEARING CALCULATOR. The input parameters are listed in table 5 as well as the resulting grease relubrication interval yielding 1 120 h. This value stays well underneath the service life of the oil serving in test bearing II, which was specified with 5 000 h.

Table 5: Input parameters concerning calculation of the relubrication interval.

input parameters	
bearing type	6220
n_s	3 000 min^{-1}
F_r	5 kN
rotating ring	inner ring
T_b	90 °C
$\boldsymbol{t_r}$	**1 120 h**

The main reasons for this result are the different temperatures the lubricants are exposed to. However, ambient conditions, especially bearing temperature, are equal for both rolling bearings. The result clarifies the essential benefit regarding maintainability by using a ring lubricator. Related to the entire service life of the oil, the time of contact between the oil and the "hot spots" of the bearing arrangement, including the rolling bearing and the oil sump, is quite short. In contrast, grease remains continuously in the heat-affected zone close to the rolling bearing.

4. Conclusions

The periodic oil sampling during the 6 000 h long-term test showed that the attainable service interval of a rolling bearing arrangement equipped with a ring lubricator can exceed the relubrication interval of a grease lubricated rolling bearing actually several times. Howev-

er, it was also shown that the essential requirement in order to achieve this fact is an appropriate ring lubricator design.

The comparison between two different configurations of the ring lubricator (test bearing I and test bearing II) indicated ring lubricator design to significantly affect service life of the oil. The better result was obtained with the ring lubricator design used in test bearing II, revealing that especially ring wear, oil delivery rate and foaming induced by the ring lubricator influence oil condition. According to the presented results, an appropriate ring lubricator design is basically characterised by static axial ring guidance, low ring speed and an oil delivery rate which is below the limit of axial oil flow through the rolling bearing. Taking into account these principles of ring lubricator design, the impact on the oil regarding wear debris and thermal-oxidative degradation can be minimised.

According to the sampling results accompanied by optical inspections, the attainable service life of the oil of test bearing II was conservatively specified with 5 000 h. The limiting criterion was zinc content exceeding the warning value towards the end of the long-term test. It is assumed that zinc originates from the oil ring made of brass. Since signs of wear were neither found on the ring surface nor measured in the oil (e. g. copper), zinc seems to have dissolved from the oil ring, induced by acidification of the oil. Acidification has been proven by measuring neutralisation value of the oil. Another metal detected in the oil was iron. However, the measured concentration was low and clearly underneath the general warning value. An optical inspection revealed that iron wear debris must have originated from the surfaces of axial ring guidance which showed slight signs of wear. Since the chrome content was zero, wear debris originating from the rolling bearing could be excluded. However, in order to furthermore fulfil the potential of the ring lubricator, wear behaviour of the surfaces guiding the ring in axial direction has to be improved.

Comparing the result with the relubrication interval of a grease lubricated rolling bearing, service life of the oil is approximately five times the amount. The main reason for this is traced back to lower thermal stress occurring in the bearing arrangement equipped with the ring lubricator. In comparison with grease lubrication, the retention time of the oil in the heat-affected zone around the rolling bearing is considerably shorter.

It can be summarised that in some circumstances such as high thermal stress acting on the rolling bearing or cost intensive maintenance procedures, the use of a ring lubricator reduces operating costs by significantly extending maintenance intervals. The findings gathered in this study contribute to furthermore improve maintainability of rolling bearings and to use lubricants more efficiently by installing a ring lubricator for oil supply whose design and operating characteristics meet the demands for maximum service life of the oil.

Notation

abs	absorption
C	dynamic load rating
ΔT	temperature difference
d_i	ring inner diameter
F_r	radial load
h_r	ring height
κ	viscosity ratio
l	litre
v	kinematic viscosity
NV	neutralisation value
n_s	shaft speed
P	dynamic equivalent load
T_a	ambient temperature
T_b	bearing temperature in the load zone
T_{or}	oil temperature in the oil reservoir
T_{os}	oil temperature in the oil sump
t_r	relubrication interval
w_r	ring width
ZnDDP	zinc dialkyldithiophosphates

References

[1] Schaeffler Technologies AG & Co. KG (Hrsg.): Schmierung von Wälzlagern. Technische Produktinformation TPI 176 D-D. Schweinfurt: FAG, 2013.

[2] VEM motors GmbH: Montage-, Bedienungs- und Wartungsanleitung. Version 05.2012, Wernigerode, 2012.

[3] WEG Equipamentos Elétricos S. A.: Drehstrommotoren für explosionsgefährdete Bereiche. Installations-, Betriebs- und Wartungsanleitung. REF. 660 – DE, 2010.

[4] R. C. Elwell, E. R. Booser: Lubricating Journal Bearings with Oil Rings. Machine Design, vol. no. 61 (1989), issue no. 25, pp. 111-115.

[5] S. Bradshaw, J. Hawa, J. Salerno: Factors Affecting Oil Ring and Slinger Lubricant Delivery & Stability. 43rd Turbomachinery & 30th Pump Users Symposia (Pump & Turbo 2014), 23.-25.09.2014, Houston.

[6] G. E. Innes, D. Dowson, C. M. Taylor: A loose-ring lubricator model. Proceedings of the Institution of Mechanical Engineers, Part C: Journal of Mechanical Engineering Science, vol. no. 213 (1999), issue No. 3, pp. 199-209.

[7] K.R. Brockwell, D. Kleinbub: Performance characteristics of the oil ring lubricator – an experimental study. Tribology Series vol. no. 11 (1987), pp. 587-595.

[8] H. Heshmat, O. Pinkus: Experimental Study of Stable High-Speed Oil Rings. Journal of Tribology, vol. no.107 (1985), issue no. 1, pp. 23-31.

[9] M. Müller, S. Tremmel: Design Criteria for Oil Ring Lubricators to Improve Maintainability of Rolling Bearings. Society of Tribologists and Lubrication Engineers (Eds.), STLE 71th Annual Meeting and Exhibition, 15.-19.05.2016, Las Vegas.

[10] J. Brändlein et al.: Die Wälzlagerpraxis. Handbuch für die Berechnung und Gestaltung von Lagerungen. 3. Auflage. Mainz: Vereinigte Fachverlage, 2009.

[11] Lugt, P. M.: Grease Lubrication in Rolling Bearings. Chichester: Wiley, 2013.

[12] A. Schmidt: Abgedichtete, einreihige Schrägkugellager für geringen Wartungsaufwand. Sonderausgabe Konstruktion: Special Antriebstechnik (2017) issue no. 1, pp 28-29.

[13] A. G. Coenenberg, T. M. Fischer, T. Günther: Kostenrechnung und Kostenanalyse. 8. Auflage. Stuttgart: Schäffer-Poeschel Verlag, 2012.

[14] VDI 2884: Purchase, Operating and Maintenance of Production Equipment Using Life Cycle Costing (LCC). Berlin: Beuth Verlag, 2005.

[15]. W. J. Bartz: Einführung in die Tribologie und Schmierungstechnik: Tribologie, Schmierstoffe, Anwendungen. Renningen: expert, 2010.

[16] A. Krieger: Alterung von Schmierstoffen im Zahnradprüfstand und in Praxisgetrieben. Ph.D. thesis. TU München, 2004.

[17] O.-C. Göhler: Alterungsuntersuchungen und Methoden zur Alterungsvorhersage für umweltverträgliche Schmierstoffe in neu gestalteten Tribosystemen. Ph.D. thesis. RWTH Aachen, 2007.

[18] Forschungsvereinigung Antriebstechnik: Axiale Öldurchflussmengen. Axiale Öldurchflussmengen durch Wälzlager verschiedener Bauformen. Final report research project no. 474 II, issue 1009, 2012.

[19] DIN 322: Gleitlager – Lose Schmierringe für allgemeine Anwendung. Berlin: Beuth, 1983.

[20] DIN 51444-2: Prüfung der Alterungsbeständigkeit nach Baader, Prüfung bei 110 °C. Berlin: Beuth, 2001.

[21] W. J. Bartz: Additive für Schmierstoffe. Renningen: expert, 1994.

[22] M. Müller, S. Tremmel: Die Schmierstoffversorgung von Wälzlagern mittels loser Schmierringe – ein Ansatz zur Reduktion des Wartungsaufwands unter schwierigen Betriebsbedingungen. Dresdner Maschinenelemente Kolloquium 2015. Dresden, Germany 8.-9. December 2015, pp. 519-538.

[23] F. Eckhardt: Stationäre Zahnradgetriebe: Schmierung und Wartung. Mobil Oil AG, 1987.

Radially Preloaded Cylindrical Roller Bearings –Operating Performance and Optimized Preload

Roman Böttcher, Gerhard Poll

Institute of Machine Design and Tribology (IMKT), Leibniz Universität Hannover, boettcher@imkt.uni-hannover.de

Abstract – Intentionally applied preload can extend bearing life and can help to avoid damages due to slip. Although preloads are widely utilized with angular contact bearings, preloaded cylindrical roller bearings are rarely used in industrial applications. Besides their advantages, preloaded bearings can tend to increase their preload in a self-reinforcing way which leads to limitations regarding their application.

The performance of different preloaded cylindrical roller bearings (NU2212, NNCF5012 and NU2256) is described by means of characteristic values that were developed from experimental data. The characteristic values are examined regarding indications for instationary and self-reinforcing behavior as well as application limits.

A method for the estimation of radial preloads optimized for maximum bearing fatigue life is presented that is easy to use and requires only minimal computing time. The method is derived by an evaluation of a multitude of calculation results obtained with an iterative calculation of the load distribution in the bearing. The estimation formula presented in this paper is valid for rigid structures surrounding the bearing and provides a higher accuracy than the methods previously published by other authors mentioned in this paper.

Keywords –radial preload, CRB, clearance, temperature behavior , load distribution

1. Introduction

Rolling element bearings can be used with preload either to increase stiffness and bearing capacity while operating with high loads or to avoid damage due to slip in partial load conditions [1, 2, 3]. Preload resp. negative clearance is usually applied axially on angular contact bearings (e.g. tapered roller bearings (TRB) in wheel bearings of commercial vehicles, angular contact ball bearings (ACBB) in main spindles of machine tools and deep groove ball bearings in electric motors). Although the benefits of bearing preload can also be obtained on cylindrical roller bearings (CRB), only precision spindle bearings (double row CRB) in machine tools are operated with light radial preload in larger numbers in order to increase stiffness and therefore accuracy [4].

The actual value of bearing clearance during operation - positive as well as negative - is influenced by the initial bearing clearance and mounting conditions as well as temperature gradients between inner and outer ring. Temperature gradients result from friction losses inside the bearing or heat flow from the surrounding system [5]. Shaft bearings normally run with an inner ring temperature higher than the outer ring temperature which leads to smaller clearance during operation than at stop [6, 7]. Temperature gradients and therefore bearing clearance values depend on operating conditions and system characteristics and can vary autonomously and even in a self-reinforcing way especially during start-up of the bearing system.

The preload in all types of preloaded bearing systems can rise in a self-reinforcing loop until the bearing is damaged due to excessive contact pressure [8] or high temperatures resp. resulting unfavourable lubrication conditions [9, 10]. Temperature gradients resp. preload forces and bearing temperatures were investigated primarily for axially preloaded bearing systems by means of experiments [9] and thermal-mechanical simulations [11-15] for a variation of operation conditions and initial preload forces. STEIN and TU calculated for axial preloaded ACBBs that the preload increases during operation when the rotational speed and initial preload rises, possibly until self-reinforcing transient conditions occur [11]. The number of studies regarding the behavior of radially preloaded CRB is smaller; furthermore they concentrate mostly on precision bearings for machine tools and rather small preloads [4, 10, 16, 17]. Systematic investigations regarding a broad variation of preloads for CRB as well as operating conditions of common drive systems seem to be missing. OPITZ observed for double-row CRB of machine spindles that the decrease of clearance during operation intensifies with increasing rotational speed as well, but is less pronounced with decreasing initial clearance [4]. HAMPP measured bearing temperatures for CRB with varying inner geometry and initial clearance and preload [17]. The temperature rises especially for full complement bearings when the clearance is reduced.

An external radial force acting on a rolling element bearing is normally transferred only by few rolling elements. The number of loaded rolling elements resp. the size of the loaded zone of the stationary ring depends on the amount of elastic deformation under load and the bearing clearance [18].

To calculate the rolling element loads Q, a nonlinear equation system has to be solved that follows the equilibrium between the forces inside the bearing and the external radial force F_{rad} [19].

$$F_{\mathrm{rad}} = Q_{\max} \sum_{n=1}^{Z} \left(1 - \frac{1}{2\varepsilon}[1 - \cos\psi_{\mathrm{n}}]\right)^{1/q} \cos\psi_{\mathrm{n}} \qquad (1)$$

$$, \text{with } \psi_{\mathrm{n}} = \mathrm{n}\frac{2\pi}{Z} \qquad (2)$$

The expression contains the total number of rolling elements Z, the maximum rolling element load $Q_{\max}$, as well as the influence factor of load ε that describes the propagation of the loaded zone [20]. The latter two variables depend on the radial deflection of the bearing and have to be determined continuously while solving equation (1) iteratively [16, 21]. Faster methods to calculate rolling element loads with less computing time exist, too, e.g. by approximation of load distribution integrals [22] or approximation of maximum rolling element loads [23].

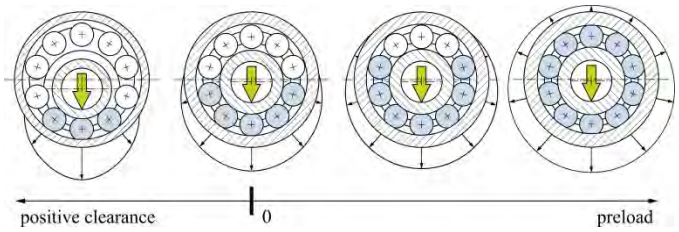

Figure 1:Illustration of load distribution in a rolling element bearing under radial load as a function of bearing clearance

The number of loaded rolling elements rises with a decrease of bearing clearance until the load zone extends over the whole circumference of the bearing, see Figure 1. Starting at positive values of clearance, the maximum rolling element load therefore decreases when the clearance is reduced until a minimum contact load on the highest loaded rolling element is reached. The maximum contact load will rise again with further decreasing clearance especially when all rolling elements are loaded. Correspondingly, the bearing life will rise with decreasing positive clearance until a maximum is reached at defined preloads (ε=0,7 [20, 24]) and it will decline with further reduction of clearance [23].

OSWALD et al. [23] studied the calculated bearing fatigue life as a function of radial bearing clearance of different radial bearings for various radial loads resp. contact pressures while assuming rigid supporting structures. To be able to compare experimental or theoretical fatique

life results obtained with different parameter combinations, the actual value of bearing life was set into relation to the calculated life at zero clearance (life factor *LF*) in a first step, see also [25]. The bearing life resp. the life factor *LF* shows a dependency on rolling element diameter: Higher preloads are needed to reach the maximum bearing life for larger rolling elements. To allow for a direct comparison of different bearing sizes, the influence of rolling element diameter was subsequently eliminated by introducing a dimensionless internal clearance G_r' .

$$G_r' = \frac{G_r}{D_R} \tag{3}$$

The calculated bearing life as a function of bearing clearance also depends on load or more exactly on the deflection under load: With rising external radial load, higher values of preload are needed to reach the maximum of bearing fatigue life. Therefore, the dimensionless clearance was further scaled by OSWALD et al. to achieve comparability. The dimensionless clearance G_r' was expanded by the ratio of the reference contact pressure at zero clearance S'_{max} and the contact pressure S_{max} for the actual radial load at zero clearance.

$$\widehat{G_r'} = \frac{G_r}{D_R}\left(\frac{S'_{max}}{S_{max}}\right)^2 \tag{4}$$

By means of the dimensionless internal diametral clearance number $\widehat{G_r'}$, the curves of different bearing sizes and radial loads could be matched and subsequently fitted in sections. The computed array of curves has a common maximum of bearing life at $\widehat{G_r'}$=-0.0013 with a life factor of 1.15 compared to bearings with zero clearance.

2. Approach

2.1. Experimental investigation of the temperature behavior of preloaded CRB

Different bearings were operated with various clearance values - positive as well as negative – under radial load to explore the temperature behavior and the possible occurrence of self-reinforcing temperature gradients. The bearings were lubricated with injected oil. The tests were started from room temperature under full load. To evaluate the operating performance, the temperature of the inner and outer ring, the temperature of the oil supply and drain as well as the motor current as a quantity proportional to the frictional moment of the system were measured and recorded during the experiments.

A single bearing test rig which was originally designed to investigate the influence of misalignment on the performance of rolling element bearings was modified to examine the thermal behavior of preloaded CRB. Its feature of adjustable misalignment was used to avoid tilting and skewing of the inner ring against the outer ring during the temperature tests presented hereafter. Figure 2 offers a side view of the test rig with its main components.

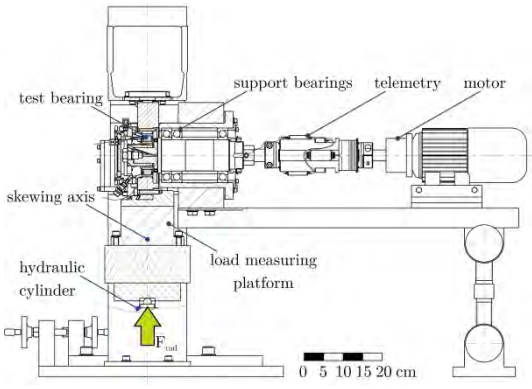

Figure 2:side view single bearing test rig

The outer ring of the test bearing was mounted with an interference fit. The outer ring housing was designed by means of FE-simulations in such a way that the outer ring raceway was evenly supported around its circumference as well as in axial direction. The housing is connected to the test rig over a load sensing platform which allows for a measurement of the bearing forces. A hydraulic cylinder was used to apply a radial force to this arrangement.

The bearing clearance after mounting c_M was set by conical sleeves supporting the inner ring of the bearing on the driven shaft of the test rig. The diameters of raceways and rollers were measured to calculate the actual clearance resp. preload after mounting. The value of total clearance during operation could be determined based on the temperature gradient between inner and outer ring calculated from the bearing temperatures.

To investigate the temperature behaviour of CRB with different clearance or preload values, the test bearings were operated until stationary conditions or predetermined temperature limits were reached. Figure 3 shows a typical trend of bearing temperatures measured during the beginning of a test with a CRB with positive clearance. The temperature of the inner ring T_{IR} as well as the outer ring temperature measured in the loaded zone $T_{OR,180°}$ (measuring position 180°) and on the opposite side of the bearing $T_{OR,0°}$ are plotted for the initial 60 minutes of a test together with the resulting calculated temperature gradient ΔT (secondary y-axis). Figure 3 only shows a part of the test run. The total running time until stationary conditions exceeded the time shown in Figure 3 by far.

The bearing temperature measured at the fitting surfaces of the bearing rings rises quickly and continuously after starting. The trend levels out with advancing test time until stationary conditions are reached (not shown in Figure 3). The temperature gradient rises as well after the start but decreases after a certain time until it approaches its stationary value. The temperature gradient and hence the resulting reduction of clearance is therefore larger during the start-up phase than under stationary conditions.

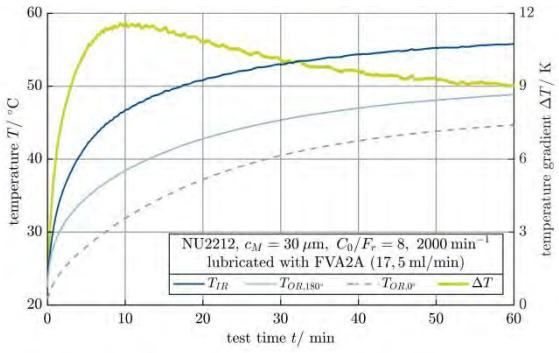

Figure 3:Development of bearing temperatures during start up

The test conditions of the experiment depicted in Figure 3 thus led to a stationary operation of the bearing. Instationary operation, however, would be characterized by a steady increase of temperature gradient and motor current and a progressive development of bearing temperatures, see also [9] and [26].

To evaluate the temperature behavior of CRB with different defined mounting clearance values and under various operating conditions, three characteristic values were extracted from the measured temperatures, if possible:

- stationary, averaged bearing temperature $\overline{T_{stat}}$
- stationary temperature gradient ΔT_{stat}
- maximum temperature gradient ΔT_{max}

The stationary, averaged bearing temperature $\overline{T_{stat}}$ was calculated as the mean value of the inner ring temperature (T_{IR}) and the average of the outer ring temperatures measured during stationary operation at two different positions ([$T_{OR,0°}$+$T_{OR,180°}$]/2). The stationary temperature gradient ΔT_{stat} represents the difference between the inner ring temperature and the averaged outer ring temperatures when the bearing is operated with stationary temperatures, whereas the maximum temperature gradient ΔT_{max} describes the maximum occurring temperature difference during start up. Positive values indicate that the inner ring is warmer than the outer ring.

The results of the experimental investigations will be presented hereafter by means of these characteristic values at first based on the experiments with the bearing type NU2212 ECP. The test conditions are summarized in Table 1. The bearing was lubricated by an injection of oil onto the roller faces and mounted in a massive structure.

Table 1: Operating conditions for tests regarding temperature behavior NU2212

radial load	C_0/F_r	8; 18 and 36
	(F_r/ kN	19.125; 8,5 and 4,25 kN)
rotational speed	n/ min^{-1}	1000; 2000 and 3000
mounting clearance	c_M/ µm	20; 0; -10; -20; -30 and -40
lubrication		FVA2A injected with 17.5 ml/min
start temperature	T_0/ °C	20 (room temperature)

The stationary, averaged bearing temperature $\overline{T_{stat}}$ is shown in Figure 4 over a variation of mounting clearance c_M for different loads and rotational speeds. The test series with the highest radial force and rotational speed used for the investigations regarding temperature behavior had to be stopped before stationary conditions could be reached because a predetermined temperature limit was reached. The limit was set to avoid an operation with mixed lubrication conditions.

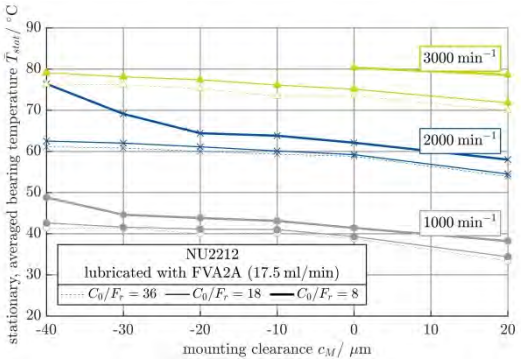

Figure 4: stationary, averaged bearing temperature NU2212

The temperatures for different rotational speeds differ significantly. The bearing temperature rises with increasing speed and load as well as decreasing bearing clearance due to growing frictional losses.

The calculated stationary temperature gradient ΔT_{stat} is plotted as a function of mounting clearance in Figure 5. The secondary y-axis represents the clearance reduction resulting from the temperature gradient Δc_T.

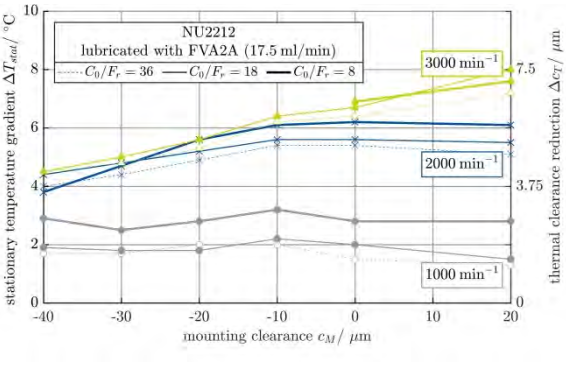

Figure 5: Stationary temperature gradient NU2212

Rotational speed and load have an influence on the temperature difference between inner and outer ring, too, when observing positive clearance: The temperature difference rises with increasing speed and load, whereby the influence of varying speeds is more distinct. The temperature gradient decreases when the mounting clearance is reduced especially for higher rotational speeds. This behavior matches the observations of OPITZ in [4]. The influence of speed and load are less pronounced with decreasing preload for higher speeds and are nearly missing for the highest preload shown in Figure 5.

In addition to the experimental investigations, analyses regarding the distribution of external loads on the rolling element set were performed, see also section 2.2. Figure 6 contains the distribution of calculated roller loads for the highest load used in the experiments with the bearing NU2212. The calculation implies rigid structures surrounding the bearing and the absence of misalignment as well as centrifugal forces.

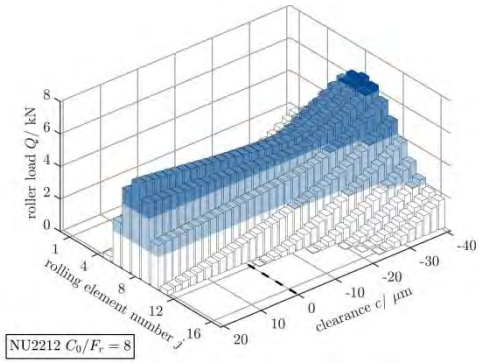

Figure 6: calculated distribution of rolling element loads NU2212

When considering the thermal reduction of clearance Δc_T shown in Figure 5 with the secondary ordinate and the load distribution inside the bearing in Figure 6, all of the rolling elements are loaded even under the deflection of the highest load for values of mounting clearance of about -20 µm and below.

Besides the test steps that had to be stopped due to predetermined temperature limits, stationary conditions could be reached even while using preloads larger than needed for an optimization of bearing fatigue life (see Figure 14). The analysis of the characteristic values (stationary averaged bearing temperature $\overline{T_{stat}}$ and stationary temperature gradient ΔT_{stat}) showed no signs of self-reinforcing effects regarding the temperature gradient or bearing preload. As described before, the temperature gradient can be higher during the start-up phase compared to stationary operation. Indications for an instationary behavior could therefore most likely be found at the maximum bearing temperature ΔT_{max}. It is plotted in Figure 7 for the test parameters used before.

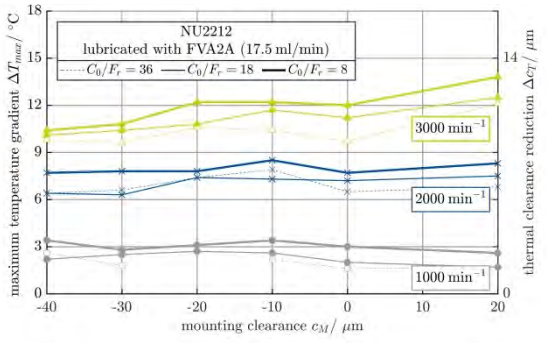

Figure 7: maximum temperature gradient NU2212

Increasing rotational speeds or radial loads lead to rising maximum temperature differences between the inner and outer ring of the bearing. The difference between the temperature gradient during start up and its stationary value, see Figure 5, increases with rising rotational speed, too. Besides the test runs at 3000 min^{-1}, the maximum temperature is nearly unaffected by a variation of bearing clearance. At 3000 min^{-1}, the maximum temperature gradient decreases with declining bearing clearance which resembles the behavior of the stationary temperature gradient.

A self-reinforcing growth of temperature difference between the bearing rings could not be triggered for the test bearing NU2212 at a clearance of -40 µm even with elevated rotational speeds. Although the test runs could not reach stationary conditions due to higher temperatures resulting from the frictional losses at higher speeds, the temperature gradients always decreased after reaching a maximum during the phase of start-up.

Additional tests were performed with a preloaded double-row full complement CRB (NNCF5012) in a nearly identical experimental setup to investigate if the additional friction losses resulting from the contact forces between the rollers can cause instationary behavior. Table 2 summarizes the test conditions. In contrast to the experiments with the CRB NU2212, the oil was injected between the rows of rolling elements through the outer ring.

Table 2: Operating conditions for tests regarding temperature behavior NNCF5012

radial load	C_0/F_r	16; 32 and 64
	(F_r/ kN	18.75; 9.375 and 4.688 kN)
rotational speed	n/ min^{-1}	500; 1000 and 1500
mounting clearance	c_M/ µm	10; 0; -10; -20; -30 and -40
lubrication		FVA2A injected with 35 ml/min
start temperature	T_0/ °C	20 (room temperature)

The characteristic values extracted from the temperatures measured during the test runs show a similar behavior as described before. Figure 8 plots the averaged bearing temperature during stationary operation $\overline{T_{stat}}$ over a variation of clearance.

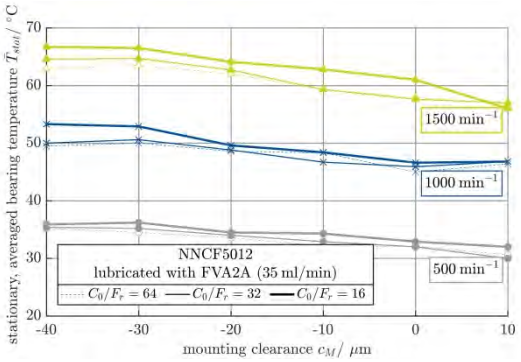

Figure 8: Stationary, averaged bearing temperature NNCF5012

The influence of rotational speed on the bearing temperature is again obvious. The curves of different radial loads differ less than those of the bearing NU2212 with cage. However, the rated radial loads C_0/F_r used to investigate the temperature behavior of the bearing NNCF5012 are smaller. As seen before, the bearing temperature rises with decreasing clearance.

Figure 9 contains a compilation of the calculated roller loads of the bearing NNCF5012 for a variation of bearing clearance and the highest load used for experimental investigation. As stated before, see Figure 6, the calculation only considers static forces between rolling elements and their raceways due to an external radial load. According to Figure 9, all rolling elements are already loaded at clearance values of -10 µm and below even under deflection by the highest load used to investigate the temperature behavior.

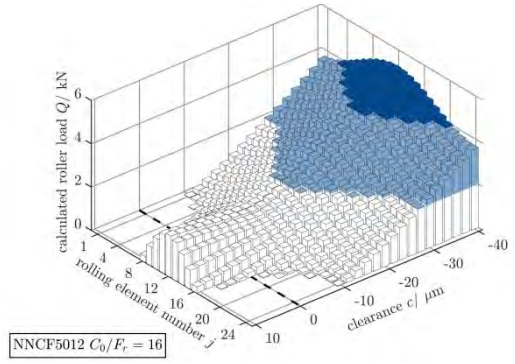

Figure 9: calculated distribution of rolling element loads NNCF5012

The maximum difference between the inner and outer ring temperature ΔT_{max} of one bearing row of the bearing NNCF5012 are shown as a function of mounting clearance c_M in Figure 10. In contrast to the absolute bearing temperature, the temperature gradient decreases significantly with a reduction in positive clearance. With negative mounting clearance (preload), there is no more change in gradient. The reason still needs to be explored. A higher heat transfer via rolling elements with a growing number of contacts could be a possible influence.

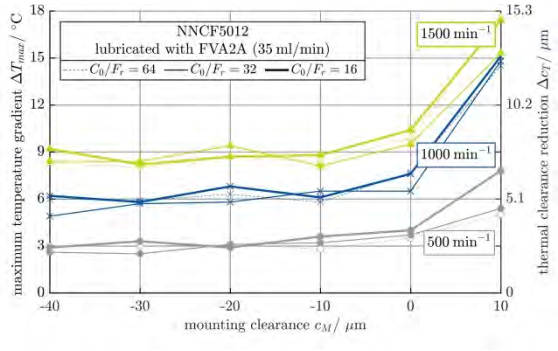

Figure 10: maximum temperature gradient NNCF5012

None of the tests performed with the full complement bearing NNCF5012 under the test conditions listed in Table 2 showed indications for instationary behavior. Besides rising temperatures being able to cause mixed lubrication, the bearing temperatures resp. temperature gradients did not develop critically with decreasing clearance for both bearings with a bore diameter of 60 mm.

In addition to the investigations with smaller bearings and an extensive set of test parameters, sample tests with a large size test bearing NU2256M were performed especially under radial preload. The bearing was operated by help of the large size bearing test rig of the Institute of Machine Design and Tribology in a rotationally symmetric housing under radial load. The operating conditions are listed in Table 3.

The analysis of the test runs showed a temperature behavior similar to the test runs explained before: The stationary temperature gradient decreases with decreasing clearance while the bearing temperature rises. No indications for an instationary behavior could be found.

Table 3: Operating conditions for tests regarding temperature behavior NU2256

radial load	C_0/F_r	6; 12 and 18
	(F_r/ kN	542; 271 and 181 kN)
rotational speed	n/ min^{-1}	500
mounting clearance	c_M/ µm	0; -150 and -300
lubrication		Mobil Vacuoline 533 injected with 3 l/min
start temperature	T_0/ °C	25 (room temperature)

2.2. Calculation of load distribution/ optimized bearing clearance

The theoretical investigation regarding the influence of a bearing clearance variation on the inner load distribution and bearing fatigue life was performed using the bearing calculation software of the FVA LAGER2HP. It was developed and refined in several research projects, see for example [27] and [28] and allows the calculation of e.g. rolling element loads, bearing life and friction losses for different types of bearings and operating conditions. The bearing fatigue life time is calculated using the standardized method described in [29] in consideration of individual rolling element loads as well as the pressure distribution over the contact length of the contact. The inner geometry of the bearings as well as all raceway profiles were measured on existing bearings and were used for the investigations regarding bearing clearance. To obtain finely resolved calculated data for clearance variations, automatic routines were programmed for LAGER2HP. The structures surrounding the bearing were assumed as rigid. Variations of clearance were generated by a simultaneous adjustment of the raceway diameters; rolling element and pitch circle diameters were kept constant.

Figure 11 shows calculated rolling element loads plotted over the circumference of a single-row CRB with cage for a relatively small radial

load. As described in chapter 1, the maximum (central) rolling element force decreases with lowered positive clearance and defined preload due to a broadened load zone. The smallest central roller load occurs with load zone extensions still below 360°. All rolling elements are loaded with further decreasing clearance which leads to an additional load on the rolling elements in the load zone and therefore rising maximum roller loads due to equilibrium conditions.

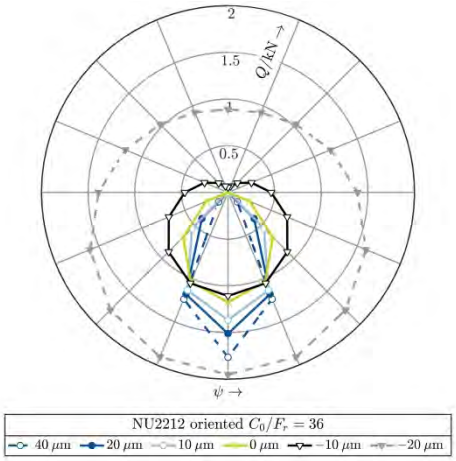

Figure 11:calculated rolling element loads for different clearance values

The maximum contact pressure p_{max} as well as the nominal bearing life L_{10r} were calculated based on the roller load distribution. Both quantities are shown as a function of bearing clearance and radial load in Figure 12 and Figure 13 for the bearing NU2212 utilized before. The development of the values as a function of clearance is highlighted for three radial loads used for experimental investigations as well as the clearance of minimum contact pressure resp. maximum life time and the zero clearance condition.

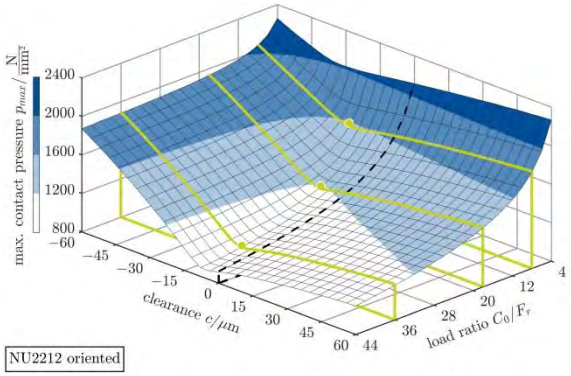

Figure 12:calculated maximum contact pressure for a variation of clearance and load

Starting from values of positive clearance, the maximum contact pressure p_{max} is reduced with decreasing clearance until a minimum is reached. As described before, the value of the optimum preload c_{opt} is load-dependent: Higher preloads are needed to reach minimum contact pressure at the highest loaded rolling element with a rising external load. The maximum contact pressure rises again with a further reduction of clearance beyond the optimum preload and the calculated bearing fatigue life time L_{10r} is decreases as was to be expected and described before. The bearing life for excessive preloads is nearly solely defined by preload and not by external load.

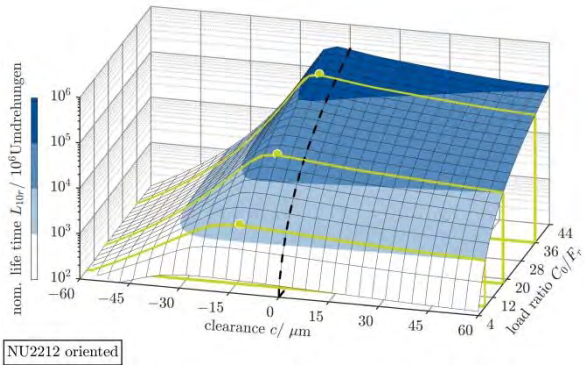

Figure 13:calculated bearing fatigue life for a variation of clearance and load

The values of optimized preload with respect to contact pressure and in relation to bearing fatigue life are plotted in Figure 14 as a function of radial load. They differ from each other: Maximum bearing life time is achieved at smaller values of preload compared to optimized preloads for minimum contact pressure. Latter condition indeed causes lower maximum strains but stresses a larger material volume.

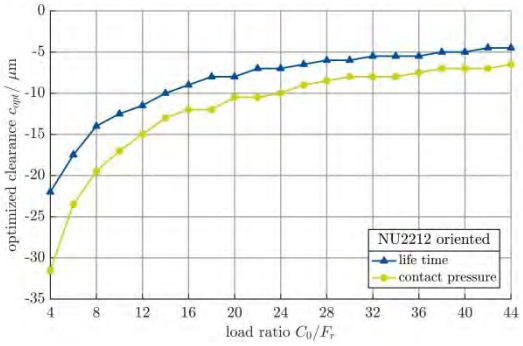

Figure 14:calculated optimized preload

The influence of different sizes and types of CRB on the load distribution and specifically on the value of optimized preload was investigated as well. The bearing life time resp. the life factor in accordance to [23] and [25] are shown in Figure 15 for different CRB with identical inner ring diameter. In the absence of adequate bearings for geometry examination, catalog data regarding the inner geometry were used for the calculations shown below.

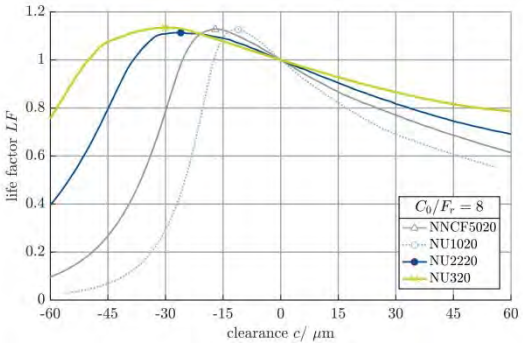

Figure 15:calculated optimized preload for different CRB of 100 mm bore diameter

The influence of rolling element diameter D_R which differs between the investigated bearings, see Table *4*, corresponds to the work of OSWALD et al. Larger values of radial preload are needed to reach maximum bearing life when the rolling element diameter rises.

Table 4: rolling element diameter used in Figure 15

NNCF5020	NU1020	NU2220	NU320
17.5 mm	12 mm	28 mm	40 mm

Hereafter, only the value of the optimized preload regarding bearing life $c_{\mathrm{opt,L}}$ will be observed. It is plotted for one bearing type and different loads as a function of bearing size in Figure 16.

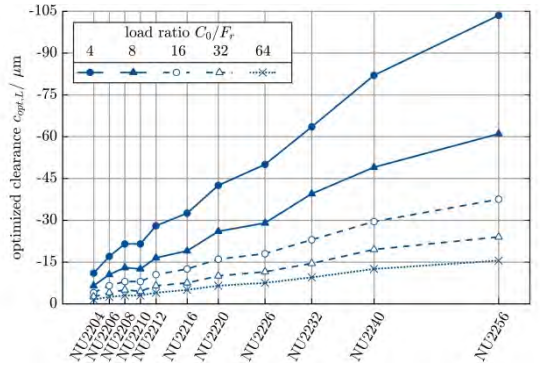

Figure 16:calculated optimized preload for different bearing sizes

Figure 17 shows the same data as before as a function of bearing size but visualizes the dimensionless clearance $c'_{\mathrm{opt,L}}$, see (3) and [23]. Since the value of the dimensionless clearance $c'_{\mathrm{opt,L}}$ can be seen as constant over the rolling element resp. inner ring bore diameter for every load ratio used for calculation, the median was calculated and plotted as well.

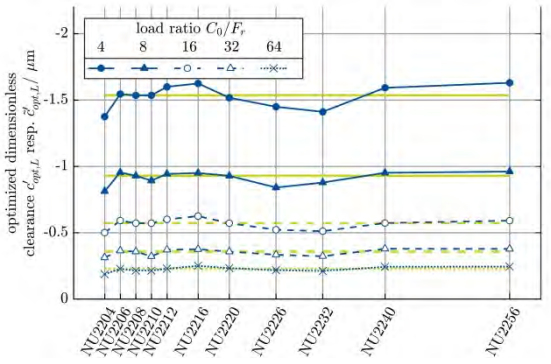

Figure 17: calculated optimized dimensionless preload for different bearing sizes

The relation between the averaged dimensionless clearance and the load ratio was approximated by a power function in the form of $y = ax^b$. The result can be transformed to a formula for the approximation of the absolute value of optimized clearance $c_{\mathrm{opt,L}}$ after resubstituting the dimensionless clearance c'.

$$c^*_{\mathrm{opt,L}} = -4{,}08 \cdot D_{\mathrm{R}} \cdot \left(\frac{F_{\mathrm{r}}}{C_0}\right)^{\sqrt{2}/2} \qquad (5)$$

The values of optimized clearance calculated based on an iterative determination ($c_{\mathrm{opt,L}}$) as shown before in Figure 16 (marked in blue) are opposed those of an approximation by means of equation (5) with a green coloring in Figure 18.

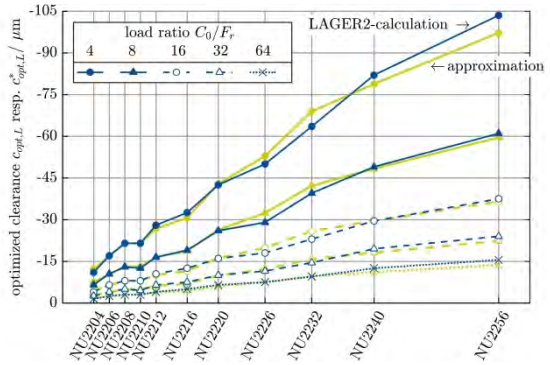

Figure 18: comparison of iteratively calculated and approximated optimized preload for different bearing sizes

The approximation closely matches the iteratively calculated optimized clearance.

3. Conclusions

The analysis of experimental investigations regarding the temperature behavior of preloaded CRB by means of the three characteristic values stationary, averaged bearing temperature $\overline{T_{\mathrm{stat}}}$, stationary temperature gradient ΔT_{stat} and maximum temperature gradient ΔT_{max} was shown. None of the bearings used for investigations (NU2212, NNCF5012 and NU2256) tended to a self-reinforcing growth of preload during the start-up phase even when using initial preloads larger than needed for an optimization of bearing life. The performance of preloaded bearings was only affected negatively at high loads and rotational speeds due to high temperatures when increasing preload.

A method for the estimation of radial preloads optimized for maximum bearing life time was presented that is easy to use and requires only minimal computing time. The method was developed by an evaluation of a multitude of calculation results obtained with an iterative calculation of the load distribution inside the bearing. The estimation formula presented in this paper is valid for rigid structures surrounding the bearing and provides a higher accuracy than the methods published before.

Acknowledgment

The research project was kindly supported by FVA e.V. with funding of the cooperative industrial research (IGF).

References

[1] Fey, H., Schreiner, H.: Vorspannung als mechanisches Doping, Konstruktion, Elemente, Methoden, Vol. 26,No. 3, S. 49-50, 1989.

[2] Osanna, P. H.: Einfluss des Einbauzustandes auf die Lebensdauer von Wälzlagern in Arbeitsspindeln, Maschinenmarkt Würzburg, Vol. 83, Nr. 49, S.942-943, 1977.

[3] Schreiber, H.: Die Steifigkeit des vorgespannten Zylinderrollenlagers, Wälzlagertechnik, No. 1/63, S. 10-16, 1963

[4] Opitz, H. et. al: Untersuchung der Steifigkeit von Lagern für Hauptspindeln in Werkzeugmaschinen, Forschungsberichte des Landes Nordrhein-Westfalen, No. 1784, 1967.

[5] Brändlien, J.: Die Wälzlagerpraxis, Vereinigte Fachverlage GmbH, 3. Edition, 1995.

[6] Stephan, E.: Dimensionierung und Montage von Wälzlagern in Achsgetrieben von Bahnen, VDI-Berichte, 1455, S. 119-136, Tagung Getriebe für Schienenfahrzeuge, 1999.

[7] Albers, A.: Ein Verfahren zur Bestimmung zulässiger Drehzahlen von Wälzlagerungen, PhD thesis, Universität Hannover, 1987.

[8] Mitrovic, R.; Atanasovska, I.; Soldat, N.; Momcilovic, D.: Effects of operation temperature on thermal expansion and main parameters of radial ball bearings, Thermal Science, Vol. 19, No. 5, S. 1835-1844, 2015.

[9] Takabi, J.; Khonsari, M. M.: On the thermally-induced seizure in bearings: A review, Tribology International, Vol. 91, S.118-130, 2015.

[10] Butz, F.: Gestaltung der Loslagerung von Werkzeugmaschinenspindeln, PhD thesis, RWTH Aachen, 2007.

[11] Stein, J. L.; Tu, J. F.: A State-Space Model for Monitoring Thermally Induced Preload in Anti-Friction Spindle Bearings of High-Speed Machine Tools, J. Dyn. Sys., Meas., Control, Vol. 116 No. 3, S.372-386, 1994.

[12] Zenker, L.: Numerische Analyse der transienten Temperatur- und Spannungsverteilung in schnellaufenden Kugellagern, PhD thesis, TU München, 1998.

[13] Stahl, T.: Einfluss von Drehzahl- und Lastkollektiven auf die Entwicklung von Reibmoment und Temperatur in Wälzlagern, PhD thesis, Universität Erlangen, 2011.

[14] Zahedi, A.; Movahhedy, M.R.: Thermo-mechanical modeling of high speed spindles, Scientica Iranica B (Mechanical Enginnering), Vol. 19, S. 282-293, 2012.

[15] Takabi, J.; Khonsari, M. M.: On the thermally-induced failure of rolling element bearings, Tribology International, Vol. 94, S.661-674, 2016.

[16] Wiemer, M.: Theoretische und experimentelle Untersuchung zum Betriebsverhalten vollrolliger Zylinderrollenlager, PhD thesis, Universität Hannover, 1990.

[17] Hampp, W.: Bewegungsverhältnisse in Rollenlagern, PhD thesis Technische Hochschule Stuttgart,1941.

[18] Palmgren, A.: Die Verteilung des Kugeldruckes im Kugellager und ihre Abhängigkeit von der sogenannten Betriebsluft, Die Kugellager-Zeitschrift, No. 3/27, S. 61-67, 1927.

[19] Breuer, M.: Theoretische und experimentelle Bestimmung der Wälzlagersteifigkeit, PhD thesis, Universität Hannover, 1994.

[20] Lundberg, G.: Die dynamische Tragfähigkeit der Wälzlager bei Berücksichtigung der Lagerluft, Forschung auf dem Gebiet des Ingenieurswesens, Vol. 18, No. 4, 1952.

[21] Wang, D.: Berechnung der Wälzlagerreibung aufgrund weiterentwickelter rheologischer Fluidmodelle, PhD thesis, Leibniz Universität Hannover, 2015.

[22] Houpert, L.: An Enhanced Study of the Load-Displacement Relationships for Rolling Element Bearings, ASME Journal of Tribology, Vol. 136, 2014.

[23] Oswald, F. B.; Zaretsky, E. V.; Poplawski, J. V.: Effect of Internal Clearance on Load Distribution and Life of Radially Loaded Ball and Roller Bearings, Tribology Transactions, Vol. 55, No. 2, S. 245-265, 2012.

[24] Bu, C.G.: Radial Clearance is key factor Affecting Roller Bearing Life Prediction in Tri-cone Bit, Advance Materials Research, Vol. 44-46, S. 233-238, 2008.

[25] Harris, T. A.; Kotzalas, M. N.: Rolling Bearing Analysis – Essential Concepts of Bearing Technology, 5. Auflage, Taylor & Francis, 2007.

[27] Breuer, M.: Programm LAGER – Programm zur Berechnung der (Wälz-) Lagersteifigkeit, final report, FVA-research project 184, IGF-Nr. 8093-AiF, No. Nr. 375, 1993.

[28] Wang, D.: Erweiterung der Berechnung der Wälzlagerreibung in FVA-Software, final report, FVA-research project 701I, 2014.

[29] ISO/TS 16281:2008: Rolling bearings - Methods for calculating the modified reference rating life for universally loaded bearings, 11/2011.

Capacitances and Lubricant Film Thicknesses of Oil Lubricated Bearings

Alexander Furtmann[1], Norbert Bader[2], Gerhard Poll[3], Hans Tischmacher[4]

[1] *Institute of Machine Design and Tribology (IMKT), Leibniz Universitaet Hannover, Germany, furtmann@imkt.uni-hannover.de*
[2] *Institute of Machine Design and Tribology (IMKT), Leibniz Universitaet Hannover, Germany, bader@imkt.uni-hannover.de*
[3] *Institute of Machine Design and Tribology (IMKT), Leibniz Universitaet Hannover, Germany, poll@imkt.uni-hannover.de*
[4] *Siemens AG, Process Industries and Drives Division, Large Drives, Nuremberg, Germany, hans.tischmacher@siemens.com*

Abstract – The electrical behaviour of mechanical components like bearings and gears becomes more and more important with an increasing number of drive trains with voltage source inverters that can be the source of harmful parasitic currents. A prediction of these currents requires knowledge of the electrical capacitance of bearings under different operating conditions. The capacitance is not only influenced by the Hertzian contact area and the film-thickness in the contact, but also by the inlet and outlet zone between the rolling elements and the raceways. With the theory of the elastohydrodynamic lubrication, the film-thickness between the discs of a two-disc test-rig are calculated. In combination with the Hertzian contact area this film-thickness is transformed into an electric capacitance. The temperature and pressure behaviour of the lubricant is also considered. Measurements are used to validate the calculation method. In a second step, the method is used to calculate the capacitance of rolling element bearings that consist of multiple EHL contacts. On a bearing test-rig a variation of lubricants, axial and radial loads, speeds and temperatures is tested and used to optimize and validate the calculation method of the capacitance.

Keywords – EHL, Elastohydrodynamic lubrication, Rolling Element Bearings, Bearing currents, Capacitance measurement

1. Introduction

The electrical capacitance of lubricated contacts and bearings is a parameter that has been investigated for many years [1–3].The focus of these investigations was to examine the film-thickness of the elastohydrodynamic contact between the rolling elements and the raceways. Nowadays the capacitance is not only of interest for the field of lubrication but also for a drive system behavior and the occurrence of bearing currents and electrical erosive wear. Modern drive systems can be characterized more and more by variable-speed operation that comes with many advantages like an increased efficiency but also some disadvantages. One of these is the occurrence of so called parasitic currents which are a result of the common-mode voltage Ucm that is inherent in the widely used voltage source inverters. The capacitance of drive system bearings – and other parts like gears [4, 5] – combined with motor inherent capacitances creates a capacitance voltage divider. As a result, a voltage U_b that is proportional to the common-mode voltage occurs at the motor bearings. Possible arc discharges in the lubricant gap can melt or vaporize material in the bearing raceways. This leads to a grey-frosted raceway with no proven influence on bearing life, or to so-called corrugated patterns or fluting (see Figure 1 a), which reduce bearing service life. Furthermore, the discharges accelerate the ageing of lubricants, especially greases, due to the catalytic effect of particles generated in the discharge arcs (see Figure 1 b). Unscheduled maintenance and therefore higher costs are the result. There are three main types of bearing currents. One of them is the so called EDM-current (Electrical Discharge Machining) which depends on the breakdown effects inside the lubrication gap of the rolling element bearing. In contrast to the two other types of bearing currents (circulating and rotor ground currents), the occurrence of EDM currents is strongly influenced by the common-mode voltage and the parasitic capacitance network behind the motor terminals which consists of the stator winding-to-frame capacitance C_{wf}, the stator winding-to-rotor capacitance C_{wr}, the rotor-to-frame capacitance C_{rf} and the capacitances C_b of the rolling bearings at the drive end and non drive end of the motor. Equation (1) gives the ratio between the common-mode-voltage and the bearing voltage – the so called Bearing Voltage Ratio *BVR* – depending on the capacitance network [10].

$$BVR = \frac{U_b}{U_{CM}} = \frac{C_{wr}}{C_{wr} + C_{rf} + C_{b\,DE} + C_{b\,NDE}} \qquad (1)$$

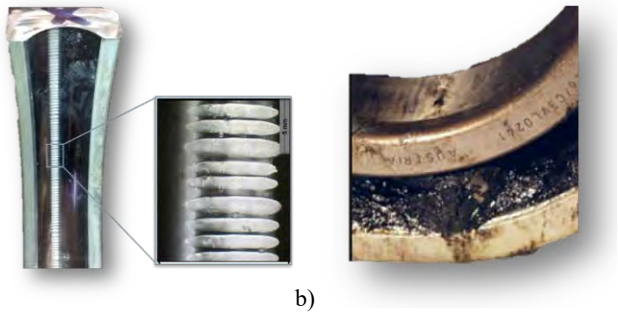

a) b)

Figure 1: Fluting on a bearing raceway (a) and charred lubricant due to EDM-currents (b) [4]

2. Basics

A prediction of EDM-currents requires the knowledge of the bearing capacitances to calculcate the voltage across the bearing and the minimum film-thickness in a bearing to determine the critical breakdown voltage. Each EHL-contact can be described as a system of three parallel capacitances as shown in Figure 2. The capacitance of the Hertzian contact can be calculated quite well, however the inlet and outlet zone of the Hertzian contact also contribute to the total capacitance [2, 6]. The influence of these areas is often described by a constant factor (usually 3.5) while in reality the factor depends on geometry and film-thickness. For a better understanding measurements and calculations for a single contact on a two-disc-testrig and for a multi contact in a bearing are conducted in this work.

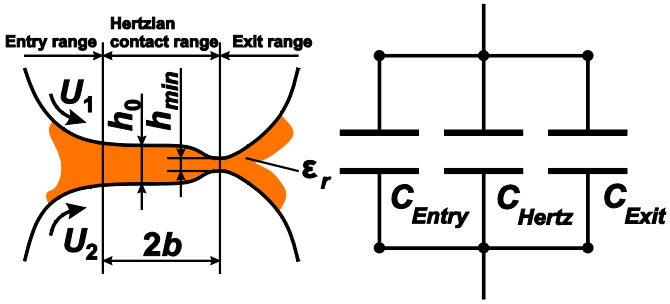

Figure 2: Equivalent model for capacitance in an EHL-Contact (according to [2, 3])

With knowledge of the Hertzian contact area A_{Hertz}, the central film-thickness h_0 and the dielectric behavior of the lubricant ε_r, Equation (2) can be used to determine the Hertzian capacitance C_{Hertz}. These parameters are all dependant on factors like the pressure p, temperature ϑ, contact force F_N, curvature radius R, combined Young's Modulus E', hydrodynamic speed v and viscosity η.

$$C_{\mathrm{Hertz}} = \varepsilon_0 \cdot \varepsilon_{\mathrm{r}}(p,\vartheta) \cdot \frac{A_{\mathrm{Hertz}}(F_{\mathrm{N}},R,E')}{h_0\left(\bar{v},F_{\mathrm{N}},R,\eta(p,\vartheta)\right)} \qquad (2)$$

The total capacitance of a contact can be calculated by Equation (3) if the capacitance of the entry and exit zone are known or if one assumed or calculated a value for $k_C = C_{\mathrm{total}}/C_{\mathrm{Hertz}}$.

$$C_{\mathrm{total}} = C_{\mathrm{Entry}} + C_{\mathrm{Hertz}} + C_{\mathrm{Exit}} = k_C \cdot C_{\mathrm{Hertz}} \qquad (3)$$

3. Single-contact model

To allow for a comparison of the single EHL contact capacitance model measurements were conducted using a twin disc test rig shown in Figure 3. Here, a single EHL contact is investigated. The contact is established between a cylindrical and a crowned disc which are pushed together with a defined normal force. The load, speed, oil temperature, and slide to roll ratio (*SRR*) can be variied. The use of insulating bearings and couplings, allows for a defined path only through the EHL contact. During the experiments the capacitance of the contact was measured using a measurement system which was applied to the shafts. The shafts were contacted using copper brushes. Subsequently a voltage step U_0 was applied over a charing resistor R. The voltage of the EHL contact U_{EHL} was measured as shown in Figure 4. From the time constant of the U_{EHL} the capacitance of the EHL contact could be determined. As only one contact is present Equation (3) can be used to describe the total capacitance C_{total}. Furthermore, the Hertzian contact area and the film thickness can be acurately calculated thus allowing for the determinitaion of C_{Hertz}. Therefore, the factor k_{c} can be accurately determined and compared to theoretically expected value resulting from simulations of the capacitance of the contacting geometries.

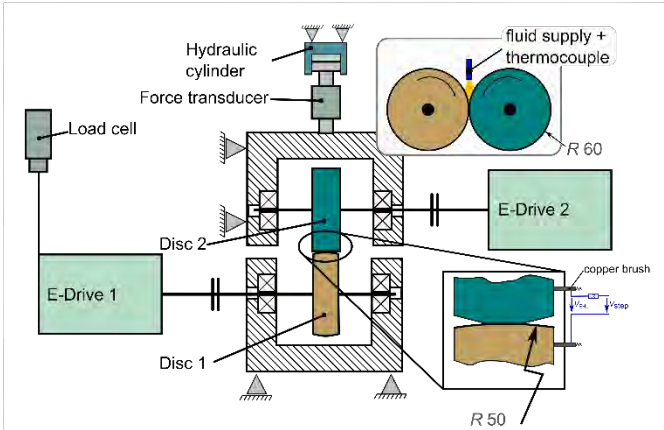

Figure 3: Twin disc test rig used in the experiments

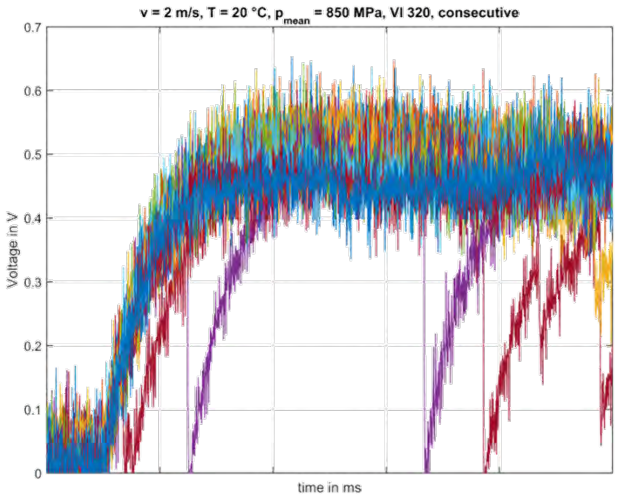

Figure 4: Measured charging curves using a voltage step U_0 = 500 mV

4. Bearing as multi-contact model

Contrary to the single-contact model of the two-disc testrig, a bearing consists of multiple contacts with different capacitances. These capacitances can be combined to a single bearing capacitance. However, for this the cage design is important as it influences the way the contact capacitances are combined. For a bearing with a conducting cage and by assuming that there is no separating fluid film between the balls and the cage, the equivalent circuit is shown in Figure 5. All contacts at one ring are in parallel with each other and then in series with the other rings' capacitances. Bearings with a non-conducting cage (e.g. polyamide as cage material) behave differently as there is no direct electrical connection between the rolling elements. As Figure 6 shows, the equivalent circuit consists of a parallel circuit for all rolling elements that consist for themselves of a series connection of the inner and outer ring capacitances.

For a bearing with N rolling elements Equations (4) (conducting cage) and (5) (non-conducting cage) can be used to calculate the bearing capacitance C_{b} from the inner-ring capacitances C_{i} and the outer-ring capacitances C_{o}.

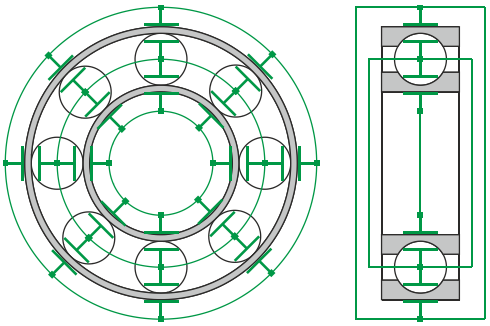

Figure 5: Equivalent model for a ball bearing with a conducting cage

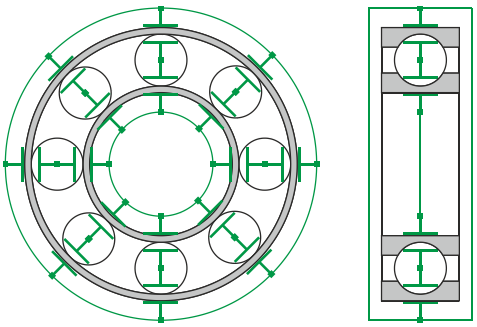

Figure 6: Equivalent model for a ball bearing with a non-conducting cage

$$C_{\mathrm{b}} = \frac{\sum_{i=1}^{N} C_{i,\mathrm{i}} \cdot \sum_{i=1}^{N} C_{i,\mathrm{o}}}{\sum_{i=1}^{N} C_{i,\mathrm{i}} + \sum_{i=1}^{N} C_{i,\mathrm{o}}} \qquad (4)$$

$$C_{\mathrm{b}} = \sum_{i=1}^{N} \frac{C_{i,\mathrm{i}} \cdot C_{i,\mathrm{o}}}{C_{i,\mathrm{i}} + C_{i,\mathrm{o}}} \qquad (5)$$

A bearing test-rig as described in [7, 8] was used to measure the capacitance behavior of ball bearings 6008 for different operating conditions like temperature, speed, load and various lubricants using an oil bath as lubrication method. Figure 7 shows the test-rig with the two outer bearings as the test speciment and the two inner bearings as support bearings to apply the radial load. The radial load is shared equally between the test bearings while the axial load is fully applied to both. Figure 8 shows the electric circuit for the capacitance measurements with a charging resistor R_{L}, the charging voltage U_0, the measured bearing voltage U_{M} and the equivalent circuits of the four bearings. As the two support bearings are hybrid bearings with ceramic balls, they can be ignored due to their low capacitance. For full lubrication the parallel resistors can also be neglected [9] and thus only the capacitances of the test bearings are measured. Assuming that these capacitances are equal – due to the same operation conditions – the measured capacitance is the double value of a single bearing capacitance.

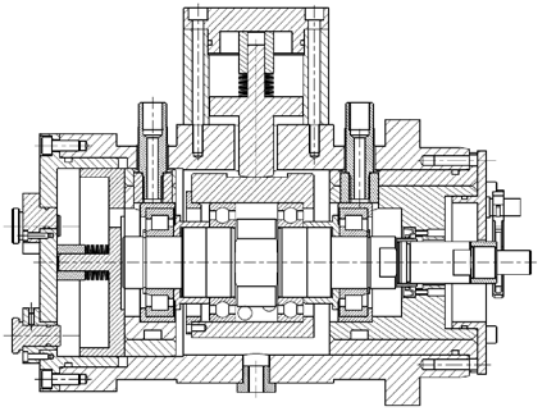

Figure 7: Bearing test-rig used for capacitance measurements

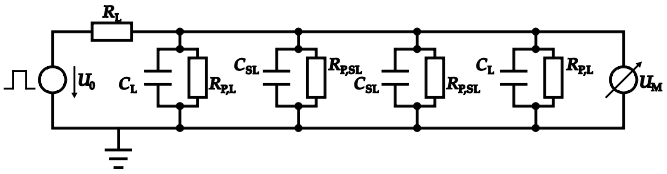

Figure 8: Electrical setup used for capacitance measurements

The lubricants used in this research were a mineral oil for industrial gear boxes with a viscosity grade ISO VG 320 (named MIN320), a synthetic polyalphaolefine oil used in wind turbine gear boxes with a viscosity grade ISO VG 320 (named SHC320), a synthetic polyalphaolefine oil used in railway gearboxes with a SAE class 75W90 (named 75W90), and base oils of typical greases for industrial applications with a viscosity grade about ISO VG 100 (named Alvania, corresponding greases were also used in the work of Wittek et Al. [7, 8]). The measurements – examples are given in Figure 9 and Figure 10 – show a few characteristic effects:

- increasing speed leads to lower capacitances due to the higher film-thickness
- increasing load leads to higher capacitances due to the bigger Hertzian contact area
- increasing temperature leads to higher capacitances due to the decrease in viscosity and therefore film-thickness
- at high speed and high viscosity (low temperature) the capacitance increases again due to starvation effects
- the influence of the Hertzian contact capacitance decreases with higher film-thickness

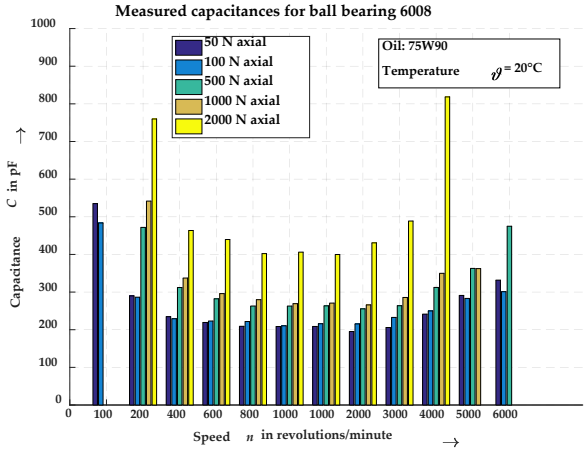

Figure 9: Measured capacitances for ball bearing 6008 by various axial loads and speed

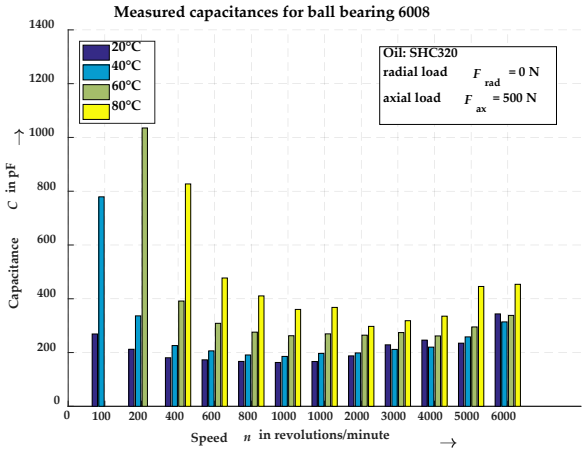

Figure 10: Measured capacitances for ball bearing 6008 for different temperatures

As mentioned before, the influence of inlet and outlet zone of the EHD-contact is often calculated by using the simplified constant factor $k_C = 3.5$. As one can see in Figure 11 this delivers a quite fair correllation for axial load for operation conditions where no starvation effect – here starting at 2000 rpm – occurs. Figure 12 shows the same factor used for radial loaded bearings with a very poor correlation between measurement and calculation. To better determine the k_C factor the ratio between the calculated Hertzian capacitance and the measured capacitance is plotted over the calculated film-thickness for a test setup with axial load only (Figure 13) and radial load only (Figure 14). In these diagrams different lubricants, viscosities and speeds were used. It can be seen that regardless of the parameters that create the film, a comparable behavior between measured and calculated capacitance exists. The resulting curves can be used to determine the total capacitance of a ball bearing (see Figure 15 and Figure 16) and is a confirmation to the results of Jablonka et. al. [6] and their tests with a ball on disc contact. The analyses for axial loads show reduced values for k_C as the Hertzian contact is larger due to the increased number of loaded balls. However, the often used value $k_C = 3.5$ is part of this curve in a regime where many measurments are performed. To determine the effectiveness of the method, only some lubricants were used to define the correlation curve. In Figure 15 the lubricant 75W90 shows a good correlation although it was not used in Figure 13.

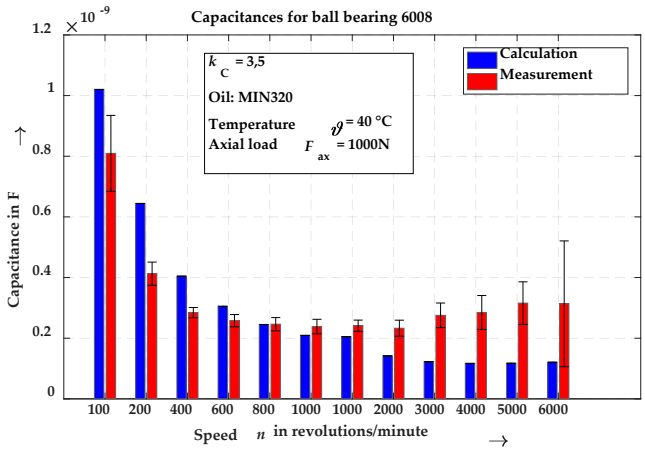

Figure 11: Comparison of calculated and measured capacitance using a constant factor $k_C = 3.5$ for axial load

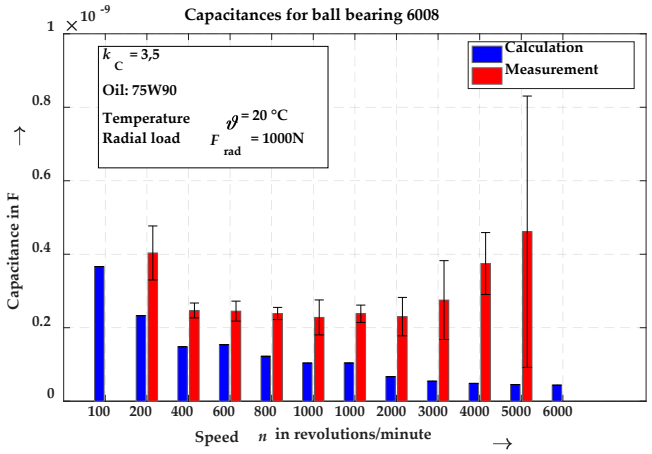

Figure 12: Comparison of calculated and measured capacitance using a constant factor k_C = 3.5 for radial load

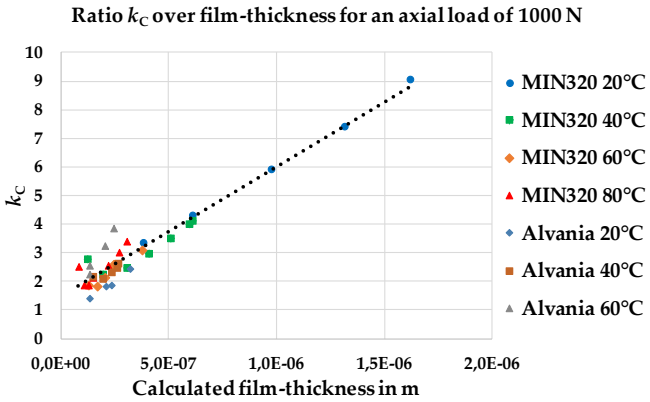

Figure 13: Ratio k_C using different oils and temperatures for an axial load of 1000 N

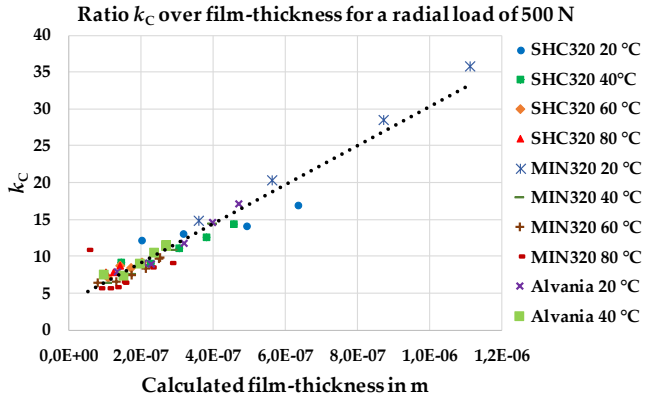

Figure 14: Ratio k_C using different oils and temperatures for a radial load of 1000 N (500 N per bearing)

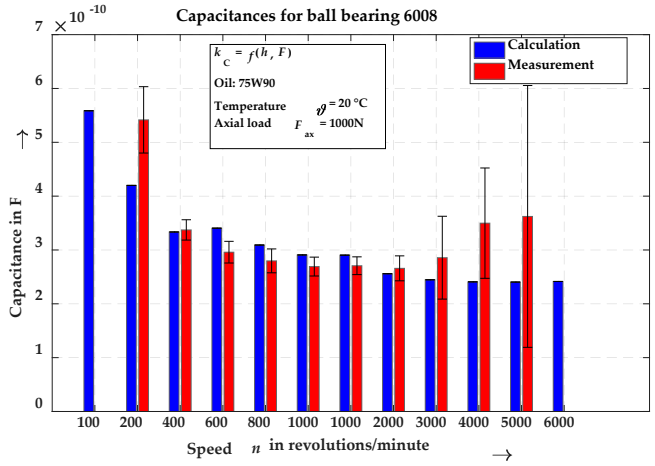

Figure 15: Comparison of calculated and measured capacitance using a factor k_C based upon load and calculated film-thickness for axial load

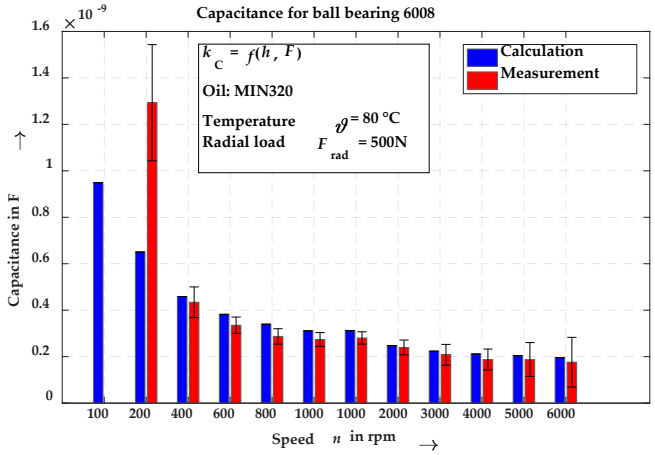

Figure 16: Comparison of calculated and measured capacitance using a factor k_C based upon load and calculated film-thickness for radial load

5. Conclusions

The research presented here investigates the electrical behaviour of EHL contacts in rolling element bearings. Due to increasing number of drive trains with inverters, more and more faults caused by parasitic currents occur. The calculation of these currents requires the knowledge of the electrical capacitance of bearings depending on the operation conditions like tempereature, load, speed, and the used lubricant. Therefore measurements and calculations for a single-contact on a twin-disc test rig and for multiple contacts in ball bearings were conducted. While the capacitance of the Hertzian contact area can be calculated quite well, the influence of the inlet and outlet zone as well as the behaviour of non-loaded rolling elements is difficult to represent. Based upon the measurements a film-thickness dependency for the total capacitance and the Hertzian capacitance can be shown for operation conditions. However, this dependency is limited to non-starved conditions This knowledge can be used to determine the capacitance accurately and thus allow a better prediction of parasitic currents.

Acknowledgment

The authors wish to thank the Siemens AG for partially funding and supporting in this project.

References

[1] A. W. Crook, “The Lubrication of Rollers II. Film Thickness with Relation to Viscosity and Speed,” Philosophical Transactions of the Royal Society A: Mathematical, Physical and Engineering Sciences, vol. 254, no. 1040, pp. 223–236, 1961.

[2] P. Brüser, “ Investigations of the elastohydrodynamic film thickness in elliptical hertzian contacts,” (in German), Dissertation, University of Braunschweig, Braunschweig, 1972.

[3] A. Dyson, H. Naylor, and A. R. Wilson, “The Measurement of Oil-Film Thickness in Elastohydrodynamic Contacts,” Proceedings of the Institution of Mechanical Engineers, Conference Proceedings, vol. 180, no. 2, pp. 119–134, 1965.

[4] H. Tischmacher, I. P. Tsoumas, and A. Furtmann, “Extended probability model for discharge activities in the drive train of converter-fed electric motors,” in 2015 17th European Conference on Power Electronics and Applications (EPE'15 ECCE-Europe): IEEE, 2015, pp. 1–10.

[5] A. Furtmann, H. Tischmacher, and G. Poll, “Extended HF equivalent model of a drive train,” in 2016 XXII International Conference on Electrical Machines (ICEM): IEEE, 2016, pp. 2244–2250.

[6] K. Jablonka, R. Glovnea, and J. Bongaerts, “Evaluation of EHD films by electrical capacitance,” J. Phys. D: Appl. Phys., vol. 45, no. 38, p. 385301, 2012.

[7] E. C. Wittek et al., “Capacitances and lubricant film thicknesses of motor bearings under different operating conditions,” in 2010 XIX International Conference on Electrical Machines (ICEM), 2010, pp. 1–6.

[8] E. C. Wittek et al., “Capacitance of bearings for electric motors at variable mechanical loads,” in 2012 XXth International Conference on Electrical Machines (ICEM), 2012, pp. 1602–1607.

[9] E. C. Wittek., “Characterisation of the lubrication condition in ball bearings with the capacitive method,” (in German), Dissertation, Leibniz Universität Hannover, Institute of machine design and tribology (IMKT), 2016.

[10] A. Mütze, “Bearing Currents in Inverter-FED AC-Motors”, Dissertation, Universität Darmstadt, Fachbereich Elektrotechnik und Informationstechnik, 2004.

Modelling power losses of cylindrical roller bearings in an FZG gear test rig

Minghui Tu[1], Mario Sosa[2], Martin Andersson[3] and Ulf Olofsson[4]

[1] *Department of Machine Design, KTH Royal Institute of Technology, minghuit@kth.se*

[2] *Department of Machine Design, KTH Royal Institute of Technology, msosa@kth.se*

[3] *Department of Machine Design, KTH Royal Institute of Technology, maan4@kth.se*

[4] *Department of Machine Design, KTH Royal Institute of Technology, ulf.olofsson@itm.kth.se*

Abstract - Power losses caused by bearings can be significant in gearbox systems. The main purpose of this research is to develop an accurate bearing friction torque model of NJ 406 cylindrical roller bearings used in an FZG gear test rig. Numerous experiments were performed on a bearing test rig under different conditions. The experimental results were compared with three existing models, namely Palmgren, Harris and SKF. The analysis was separated into zero-load friction torque and load dependent friction torque. Finally, a new model of load dependent bearing friction torque was developed. The load independent friction torque part of the Harris model was also modified for the zero-load friction torque part of the NJ 406 cylindrical roller bearings in an FZG test rig.

Keywords - Roller bearing, bearing friction, modelling

1. Introduction

In efficiency tests for gear pairs, the power losses are not only caused by the gear pair. Also, the power losses caused by bearings can be significant contributor to the measured losses. Being able to predict bearing power losses accurately can provide a better overview of the distribution of power losses in a gear test system.

There have already been many investigations of bearing friction torque. Palmgren [1] presented a bearing model of friction torque and divided it into load independent torque and load dependent torque. Harris [2] followed Palmgren's method and divided load independent torque into viscous friction torque and end-flange friction torque. SKF [3] models of bearings friction further divides the load-dependent losses into rolling and sliding components.

Different researchers have treated the bearing friction loss calculation of gear boxes in different ways. Some like Höhn [4] and Petry-Johnson et al. [5] used one friction coefficient factor to estimate bearing losses. This implies among other things that the losses are independent of rolling bearings rotational speed. Several authors chose to use one of the three models mentioned above and some authors modified one of the three models. Michaelis et al. [6] used the SKF model for load independent loss calculation and load dependent loss calculation for mineral oils; however, they used a multiplier with a new factor called load loss factor. Fernandes et al. [7] modified one of the recommended parameters in the SKF model and they claimed the SKF model could predict the power losses accurately after they tuned the parameters.

To enhance the efficiency measurements of gear pairs in FZG gear test rigs [8] the goal of this study is to experimentally test if any of the above presented models can be used to predict the load dependent as well as the load independent power losses of NJ 406 cylindrical roller bearings in back to back gear test rig accurately. Furthermore, the goal is if none of the presented models fit the experimental results can a new model be proposed.

2. Test equipment

The bearing test rig was designed based on the slave gearbox of a back-to-back gear test rig. The rig can measure the friction torque of bearings under no load and loaded conditions.

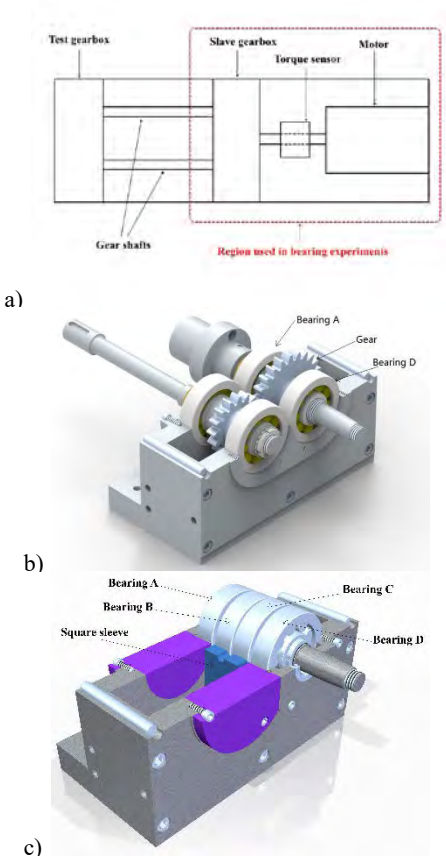

Fig. 1. Comparison between original slave gearbox and the bearing test rig: a) shows the location of the slave gearbox on the FZG test rig; b) shows the original configuration of the slave gear box; c) shows the position of bearings in the bearing test rig.

As shown in Fig. 1 a, the slave gearbox sits between the test gearbox and the motor on the FZG test rig. A torque sensor is mounted on the shaft between the motor and inner rings of the bearings inside the slave gear box. The torque sensor measures the frictional torque of bearing's inner ring. According to the blank test, the minimum torque that the torque sensor can measure is about 0.0764 Nm and the range of the measurement error is ±0.0549 Nm when keeping the accuracy around 95% [9]. The configuration of the original slave gearbox on the rig is shown in Fig. 1 b. The location of the bearings inside the bearing test rig is shown in Fig. 1 c.

The working principle of the bearing test rig is shown in Fig. 2. A lever arm is used to increase the force from a crane. This force then pushes downwards on bearings B and C. Therefore, the load on each bearing has same value, but is exerted downwards on bearings B and C and upwards on bearings A and D.

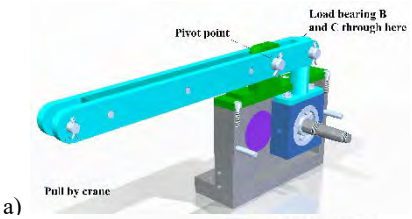

a)

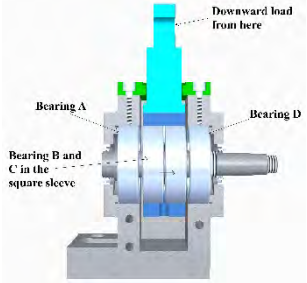

b)

Fig. 2. Configuration of bearing test rig

Precision analysis of crucial parts of the test rig was performed. To test the torque sensor used in the test rig, a blank test and a no-load test were performed and the results compared [9]. The results showed that the torque sensor has adequate sensitivity but the noise is high [9]. The force sensor used in the test rig was loaded by using increasing and decreasing calibrated weights ten times. A linear relation between the weights and the output voltage from the force sensor was found by using polynomial curve fitting [9].

The bearing test rig can be loaded from 0.6 to 9 kN and can handle rotation speeds between 50 and 3500 r/min and oil temperatures between 30 and 120 ºC. It can test dip lubrication.

3. Existing bearing model

Of the many bearing friction models, those by Palmgren [1], Harris [2] and SKF [3] are the most used.

3.1. Palmgren model

According to Palmgren [1], the bearing friction torque is divided into two parts, namely load independent friction torque and load dependent friction torque.

3.1.1. Load independent friction torque

The equation of load independent friction torque when lubricated by oil is shown in equation (1) [1].

$$\begin{cases} M_0 = 1.5572 \cdot 10^{-6} f_0 p {d_m}^3 & \frac{\eta\omega}{p} < 2 \cdot 10^{-6} \\ M_0 \;\; 9 \;\; .81 \cdot 10^{-3} f_0 p {d_m}^3 \left(\frac{\eta\omega}{p}\right)^{\frac{2}{3}} & \frac{\eta\omega}{p} \;\; 2 \;\; \cdot 10^{-6} \end{cases} \quad (1)$$

3.1.2. Load dependent friction torque

Equation (2) and (3) can be used to calculate the load dependent loss of roller bearings [1].

$$M_1 = 0.0098 f_1 g_1 P_0 d_m \quad (2)$$

$$g_1 P_0 = 0.8 F_a \cot\alpha \geq F_r \quad (3)$$

3.1.3. Total friction torque

Total friction torque can be calculated by adding load independent friction torque and load dependent friction torque together, as shown in equation (4) [1].

$$M = M_0 + M_1 \quad (4)$$

3.2. Harris model

In the Harris model [2] the friction torque of bearings can be divided into two parts, namely load independent torque loss and load dependent torque loss. Harris subdivided the load independent torque into two parts, viscous friction torque and end-flange friction torque.

3.2.1. Load dependent friction torque

Equations (5) and (6) show the method used to calculate the load dependent torque of radial roller bearings [2]. Although the equations are similar to those in the Palmgren model [1], the value of f_1 is different in the Harris model [2].

$$M_1 = 10^{-3} \cdot f_1 F_\beta d_m \quad (5)$$

$$F_\beta = max\{0.8 F_a \cot\alpha \,, F_r\} \quad (6)$$

3.2.2. Viscous friction torque

The method for calculating load independent torque from the Palmgren model can be used to calculate viscous friction torque, but the value of f_0 has been updated. Equation (7) shows the method to calculate the viscous friction torque of bearings [2].

$$\begin{cases} M_v \;\; 1 \;\; 0^{-10} f_0 (\nu_0 n)^{\frac{2}{3}} {d_m}^3 & {}_0 n \geq 2000 \\ M_v = 160 \times 10^{-10} f_0 {d_m}^3 & {}_0 n < 2000 \end{cases} \quad (7)$$

3.2.3. Total friction torque

The total friction torque of bearings can be calculated by adding the three types of friction torque together as shown in equation (8) [2]. Since the axial load of bearings was designed to be zero in this research, the end-flange friction torque M_f is always equal to zero.

$$M = M_1 + M_v + M_f \quad (8)$$

3.3. SKF model

According to SKF [3], the friction torque of bearings can be divided into four parts. Load independent friction torque can be divided into friction torque of seals and friction torque of drag losses caused by churning and splashing. Load dependent friction torque can be divided into rolling friction torque and sliding friction torque.

3.3.1. Load independent friction torque of drag loss

The friction torque of the drag loss of roller bearings can be calculated using equation (9) [3].

$$M_{drag} = 4 \times 10^{-3} V_M K_{roll} C_w B {d_m}^4 n^2 + 1.093 \times 10^{-10} n^2 {d_m}^3 \left(\frac{n {d_m}^2 f_t}{\nu}\right)^{-1.379} R_s \quad (9)$$

3.3.2. Rolling friction torque

The Rolling friction torque of cylindrical roller bearings can be calculated using equation (10) [3].

$$M_{rr} = \phi_{ish} \phi_{rs} G_{rr} (\nu n)^{\cdot \; 6} \quad (10)$$

3.3.3. Sliding friction torque

The sliding friction torque of cylindrical roller bearings can be calculated using equation (11) [3].

$$M_{sl} = G_{sl} \mu_{sl} \quad (11)$$

3.3.4. Total friction torque

The total friction torque of bearings can be calculated by adding the four types of friction torque together as shown in equation (12) [3]. Since the bearings used in this research do not have bearing seals, the frictional moment of seals M_{seal} is always equal to zero.

$$M_{rr} + M_{sl} + M_{seal} + M_{drag} \quad (12)$$

4. Methods

4.1. Experimental methods

4.1.1. Operating conditions

The input variables for the experiments are rotating speed, load, oil level, oil type, and oil temperature. Their values are shown in Table 1.

Table 1. Input variables of experiments

Oil type	Oil level [mm]	Oil temperature [ºC]	Duration of experiments [min]	Rotating speed [r/min]	Load on each bearing [N]
PAO std	73.5	40	5 (10)*	87	0
PAO LV	88.25	60		174	527
VG100	103	90		348	908
				550	1405
				1444	2738
				1740	3573
				2609	
				3479	

** Duration of 10 min only performed under zero load at 103 mm oil level using PAO std oil for three different temperatures*

The experiments were divided into zero-load bearing friction torque experiments and load dependent bearing friction torque experiments. Not all combinations were performed. The duration of experiments was always 5 min. The 10-min duration was only chosen to check whether the 5-min duration is stable enough. The viscosities of the three types of oils under different temperatures are listed in Table 2.

Table 2. Viscosities of oils under different temperatures

Oil type	Temperature [ºC]	Dynamic viscosity [mPas]	Kinematic viscosity [cSt]
PAO std	40	59.44	72.55
	60	31.56	39.14
	90	14.56	18.49
PAO LV	40	39.60	49.17
	60	20.20	25.50
	90	9.47	12.26
VG100	40	79.94	93.97
	60	32.85	39.36
	90	12.47	15.22

The oil levels were measured from the bottom of the slave gear box. The 103 mm oil level means the height of oil reaches 1.5 mm above the center of the bearings (H_{half}), the 73.5 mm oil level means the oil height just reaches the center of the lowest roller from bottom and the 88.25 mm oil level is in the middle of the two oil levels which is shown in Fig. 3. D_i is the inner diameter of the out ring.

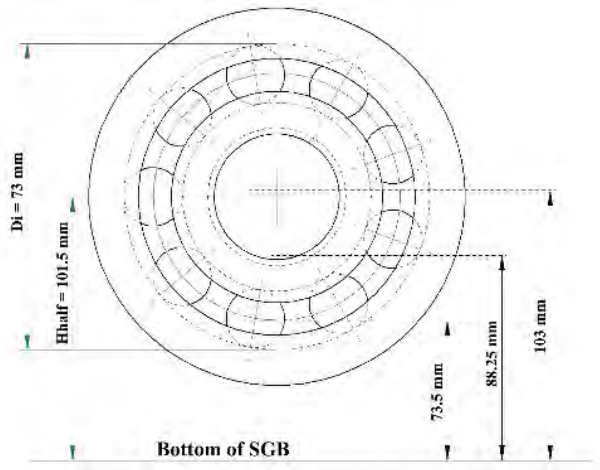

Fig. 3. Geometric relation between oil level and bearings. (SGB represents slave gear box)

4.1.2. Experimental procedure

The procedure for one experiment is listed in Table 3. In each experiment, only one oil type and one oil level can be tested. For each bearing load, all rotating speeds were tested as one cycle. For zero-load bearing friction torque experiments, only zero load was used. For load dependent bearing friction torque experiments, one zero load experiment was always performed to obtain the load dependent bearing friction torque by subtracting the zero-load friction torque from the total friction torque.

Table 3. Procedure of one experiment in detail

Step number	Step detail
1	Clean the slave gearbox by flushing oil twice (start the motor for 1 min at 1000 r/min each time)
2	Pour in new oil to required oil level
3	Close slave gearbox, set and start heating oil to required temperature
4	Apply the required load to the bearings by the traverse crane
5	Select required rotating speed
6	Start the test rig and recording MATLAB code at the same time for required duration of experiments
7	Repeat step 5 and 6 for all required rotating speeds
8 (if need to change load)	Repeat step 4 to change required load and then repeat step 7
9 (if need to change oil temperature)	Repeat step 3 to change required oil temperature and then repeat step 7
10	Close the test rig, save experimental data from MATLAB

4.2. Methods of modelling

By comparing the results of existing models and experimental data, new or modified bearing models can be created. If the results from existing models are close to the experimental data, an existing model can be modified in order to improve the results by, for example, changing the values of the parameters or adding a factor.

If there are large differences between the results from existing models and the experimental data, a new model should be developed. The process for developing a new model is shown below.

1. Create a mathematical model suitable for the experimental results.
2. Calculate values of parameters by using a least squares method.
3. Calculate confidence bounds for each parameter.
4. Verify the new model by using Monte Carlo simulation.

5. Results

5.1. Results of experiments

The differences between existing bearing models and experimental data can be found by plotting the results of existing models and experimental data together. In addition, by changing the value of one input variable and keeping other input variables constant, the effect of that input variable on the bearing friction torque can be found.

5.1.1. Zero-load friction torque

The results from existing models and experimental data for zero-load bearing friction torque were plotted together in Fig. 4. The friction torque from experiments under no load condition was treated as load independent bearing friction torque during the research and was marked as $M_{independent}$, since the experimental data are close to the load independent friction torque part of Harris model. In each subfigure, one input variable was changed while the other input variables were kept constant.

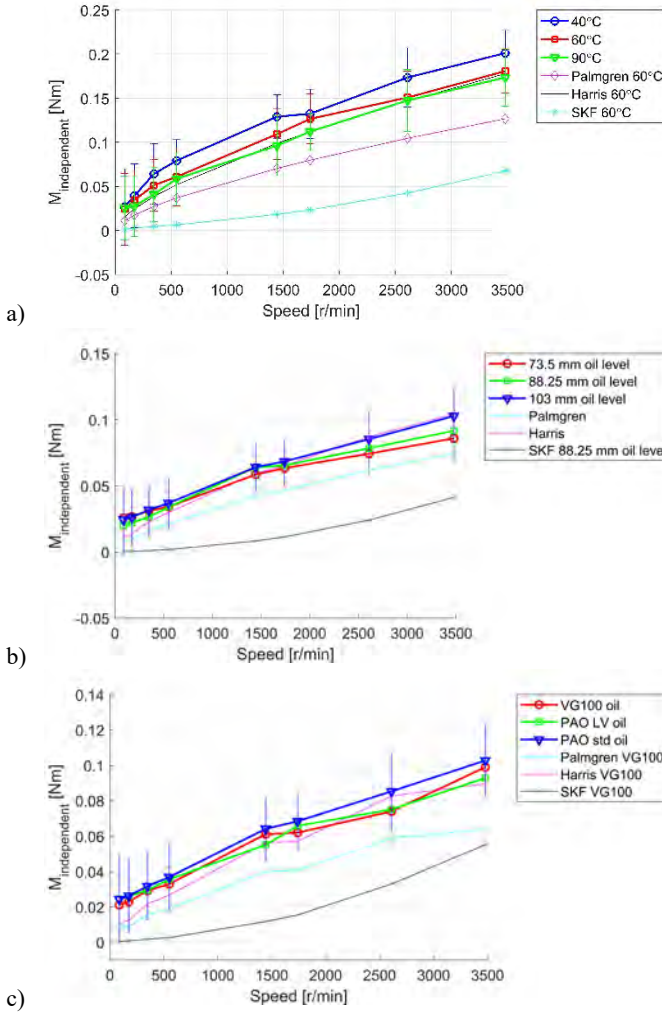

Fig. 4. Results of zero-load friction torque experiments with load independent friction torque from the three bearing models. Error bars show two standard deviations from experiments. a) Zero-load friction torque at different oil temperatures, using PAO std oil and 103 mm oil level; b) Zero-load friction torque at different oil levels, using PAO std oil and 90 °C; c) Zero-load friction torque using different types of oil, at 103 mm oil level and 90 °C.

Fig. 4 shows that oil temperature, oil level and oil type do not affect the zero-load bearing friction torque. Under all conditions, the experimental data are close to each other. In addition, the results from the Harris model are the largest among the three existing models and the SKF model has the lowest value. Of the three subfigures, independent of oil temperature, oil level, or oil type, the load independent friction torque from the Harris model was always the closest to the experimental data among the three existing models.

5.1.2. Load dependent friction torque

The results of load dependent friction torque experiments were plotted together with the results of existing models in Fig. 5. As in Fig. 4, one input variable a time was changed while the others were kept constant.

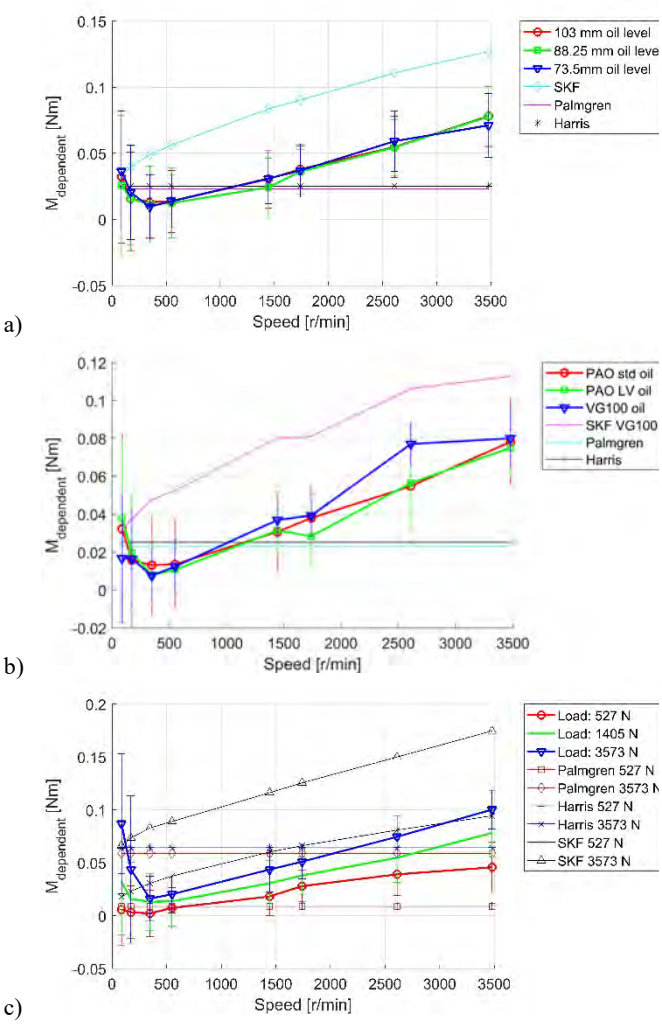

Fig. 5. Results of load dependent friction torque experiments. Error bars show two standard deviations from experiments. a) Load dependent friction torque at different oil levels, using PAO std oil at 90 °C under 1405 N load; b) Load dependent friction torque using different types of oil at 103 mm oil level, 90 °C under 1405 N load; c) Load dependent friction torque under different loads, using PAO std oil, 103 mm oil level at 90 °C.

Fig. 5 shows that oil level or oil type does not affect the load dependent bearing friction torque. However, the higher the load on bearings, the higher the load dependent friction torque get. Of the three existing models, the SKF model has the highest value in all conditions. The Harris and Palmgren models are independent of rotating speed. The experimental data curve shows a Striebeck curve behaviour [10]. None of the existing models fit the experimental data.

5.2. Results of modelling

According to the results, the zero-load friction torque data from experiments are close to the load independent friction torque from Harris model. Therefore, the load independent part of the Harris model can be used to predict the zero-load friction torque of NJ 406 cylindrical roller bearings. In order to optimize the Harris model, the value of f_0 in the Harris model was modified. None of the existing models fit the measured load dependent friction torque. A new load dependent bearing friction torque model was thus developed.

5.2.1. Optimizing the zero-load bearing friction torque model

Zero-load friction torque fits the load independent friction torque from Harris model well. In order to improve the Harris model to predict the

zero-load friction torque in this research case, the value of f_0 was modified based on the experimental data when using PAO std oil, PAO LV oil, and VG100 oil at 90 °C under different speeds. The result is shown in Fig. 6. The thin solid lines represent the value when the different oil types overlap. In addition, below 500 r/min the value of f_0 decreases significantly, but above 500 r/min, the value of f_0 becomes stable.

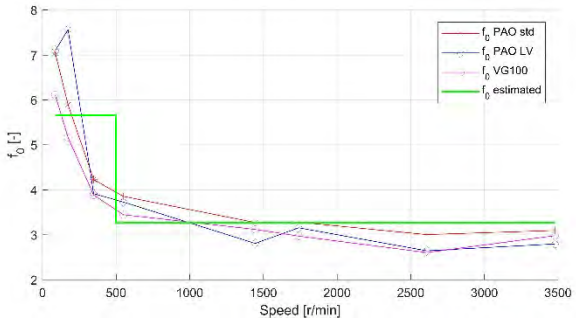

Fig. 6. Modification of Harris model by tuning f_0 using different types of oil (103 mm oil level and 90 °C)

The value of f_0 changes great deal below 500 r/min (Fig. 6). Since f_0 in the Harris model should be a constant, but the behaviour of f_0 is different below 500 r/min and above 500 r/min, mean values of f_0 were calculated for these two ranges. The old value of f_0 in the Harris model was replaced by the new values of f_0 listed in Table 4.

Table 4. Values of f_0 in Harris model at different speed regions

Speed region	Value of f_0 [-]
Speed less than 500 r/min	5.6545
Speed above 500 r/min	3.2646

5.2.2. Developing a load dependent bearing friction torque model

A mathematical function that fits the experimental data over the entire speed and load spectrum is shown in equation (13).

$$M_{dependent} = a \cdot n + \frac{\nu}{n} + c \qquad (13)$$

In equation (13), a, b and c are parameters that were calculated using a nonlinear least squares method. Using PAO std oil, 103 mm oil level at 90 °C as an example condition, the calculated values of these parameters are shown in Table 5.

Table 5. Values of parameters when using PAO std oil at 103 mm oil level and 90°C

Load on each bearing	a	b	c
527N	$1.452 \cdot 10^{-5}$	$4.760 \cdot 10^{-1}$	$-1.7 \cdot 10^{-3}$
908 N	$2.189 \cdot 10^{-5}$	$1.259 \cdot 10^{0}$	$-5.8 \cdot 10^{-3}$
1405N	$2.668 \cdot 10^{-5}$	$3.409 \cdot 10^{0}$	$-1.0 \cdot 10^{-2}$
2738 N	$2.776 \cdot 10^{-5}$	$6.510 \cdot 10^{0}$	$-5.4 \cdot 10^{-3}$
3573 N	$3.240 \cdot 10^{-5}$	$8.420 \cdot 10^{0}$	$-1.3 \cdot 10^{-2}$

The confidence bounds of the three parameters under 1405 N bearing load were calculated by the method from the MathWorks [11] and are shown in Table 6 as an example. Equation (14) and (15) are used in this method. J is the Jacobian matrix of equation (13) and s is standard deviation of the data from experiments used when calculating the value of parameter a, b and c. Then the square error S for each parameter can be found by taking the diagonal elements from the result matrix in equation (15). The value of z can be found in a standard normal distribution table. Finally, the values confidence bounds C for each parameter can be calculated by equation (14) (d represents the value of parameter a, b or c).

$$\mathrm{C} = \mathrm{d} \pm \mathrm{z}\sqrt{S} \qquad (14)$$

$$\mathrm{S} = (J^T J)^{-1} s^2 \qquad (15)$$

By using the mathematical model (equation (13)), and the calculated values for each parameter within the bounds value for specific condition, there is 95 % certainty that the model accurately predicts the load dependent loss of NJ406 cylindrical roller bearing.

Table 6. Bounds of parameters when using PAO std oil at 103 mm oil level and 90 °C under 1405 N load

Load on each bearing	a max	a min	b max	b min	c max	c min
1405 N	$2.979 \cdot 10^{-5}$	$2.357 \cdot 10^{-5}$	$4.721 \cdot 10^{0}$	$2.097 \cdot 10^{0}$	$-4.2 \cdot 10^{-3}$	$-1.6 \cdot 10^{-2}$

By using Monte Carlo simulation, the robustness of the mathematical model and the bounds for each parameter can be checked. During the Monte Carlo simulation, for each speed, the three parameters in equation (13) were set to randomly vary simultaneously 1000 times in a normal distributed range. The expectation value was set to be the calculated value of the three parameters. The standard deviation was set to be the maximum confidence bounds value among all speeds divided by z value (z is equal to 1.96 here) for each parameter. Then using the newly got three parameters to calculate the load dependent friction torque for each rotating speed.

Fig. 7 shows the results of Monte Carlo simulation under the example condition. In Fig. 7, each green point represents one run in the Monte Carlo simulation and most of which were fell into the standard deviation region of related experimental data. The model has higher accuracy in the high-speed region and most of the values from these tests are within two standard deviations of the experimental values. Also notice that the bounds are conservative with respect to the mean experimental data.

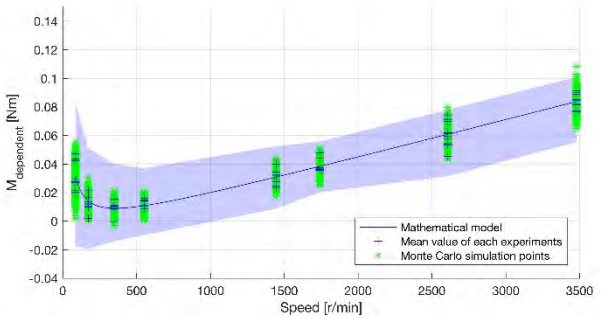

Fig. 7. Monte Carlo simulation of the new model for the condition of using PAO std oil, 103 mm oil level and 90 °C under 1405 N load on each bearing. Shaded area represents the two standard deviation region of all related experiments.

1.1.1. Total bearing friction torque from new models

In order to have a total view of the new model, the optimized zero-load friction torque model and the new load dependent friction torque model were combined by summing up to get the total friction torque of bearings.

Fig. 8 shows a comparation between total friction torque calculated by new models and a set of data from one of experiments under example condition. The experimental data is close to the value from new models and most of data are fell into the confidence bounds region.

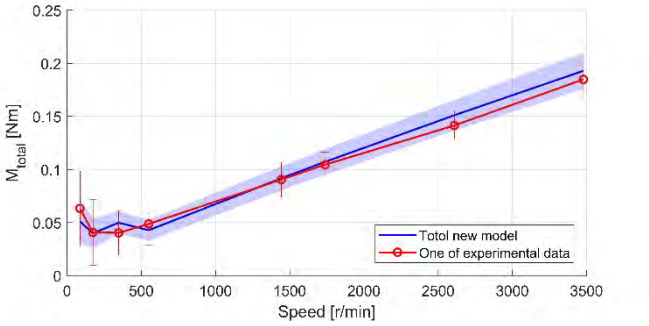

Fig. 8. Comparation of the results from new bearing friction torque models and a set of data from one of experiments. The condition is using PAO std oil, 103 mm oil level and 90 °C under 1405 N load on each bearing. Shaded area represents the region of load dependent friction torque part in new models in 95 % confidence bounds.

6. Discussion

6.1. Zero-load bearing friction torque

Although zero-load friction torque cannot be exactly equal to load independent bearing friction torque since pure load independent friction torque is hard to find, the experimental data show a good fitting with load independent bearing friction torque part in Harris model (Fig. 4). Therefore, it is possible to treat zero-load friction torque as load independent friction torque which follows Harris model in this research.

Also in Fig. 4, under different temperatures, oil levels, oil types and no load from 87 to 3479 r/min, the results from the three existing models are divergent. At different temperatures, oil levels and oil types, the value of load independent friction torque from the Harris model fits the experimental data well, especially in the high speed region. Therefore, the Harris was chosen to predict the zero-load friction torque of NJ 406 cylindrical roller bearings.

6.2. Load dependent bearing friction torque

When changing oil level and oil type, the experimental data overlap (Fig. 5), which means the effect of different oil levels, oil types and load dependent friction torque is not significant. Since Söndgen et al. [12] show that the oil levels would affect bearing friction torque under axial load, it could be imply that oil levels would have larger effect on bearings only under axial load condition. When the bearings only have radial load, the effect of oil levels would be neglectable. In addition, the effect of oil levels to the bearing friction torque could need to be further investigated. In the work of Koryciak [13], when adding the oil level to merge the whole bearing, the friction torque would be different to the condition of only half bearing is inside the oil. However, in this research, the three chosen oil levels do not merge the whole bearings. Therefore, testing more different oil levels could help to find more precise relation between oil levels and bearing friction torque.

VG100 oil has larger load dependent friction torque compared to the other oils only at around 2600 r/min. One possible explanation for this is that there is another type of additive in VG100 compared to PAO std and PAO LV oil. However, different bearing loads do affect the load dependent friction torque of bearings. The higher the load on the bearings, the higher the load dependent friction torque.

Since the load dependent friction torque from the three existing models is independent of oil level, there is only one curve for each models in Fig. 5 a. In the same way as for Fig. 4 b, the VG 100 oil condition was chosen to plot results from the SKF model in Fig. 5 b. Only the 527 N load and 3573 N load conditions are plotted in Fig. 5 c, the results from the other loads lie between these load. There is a positive correlation between load dependent friction torque and load on the bearings.

Fig. 5 shows that the experimental data does not fit any of the existing models under all conditions. When changing oil level, oil type, or load, the SKF model always has the largest value for all speeds. The Palmgren model and the Harris model are similar to the experimental data at low speeds but differ at higher speeds. So, tuning the parameters in existing models by changing the constants is insufficient. For example, the load loss factor in Michaelis et al. [6] is affected by oil types and oil temperature. Although modifying the SKF model by multiplying by a load loss factor can increase the accuracy for different temperatures and oil types, the shape of the SKF curve is still different from the curve shape of the experimental data in this paper.

Another example is tuning the value of μ_{sl}, as Fernandes et al. [7] did. However, this can only affect the load dependent friction torque in the low rotating speed region. In the low speed region, the shape of their curve of load dependent friction torque vs. rotational speed has a similar shape to our data. Fernandes et al. did not investigate the behaviour of load dependent friction torque at high speed region and their upper limit of rotating speed is 1500 r/min.

Fig. 5 shows that the relationship between bearing friction torque and rotating speed is not a constant. Therefore, using an average friction coefficient to calculate the friction torque of bearings, as Höhn et al. [4] did, would introduce an error. Also, using an average friction coefficient of bearings to calculate load dependent friction torque can cause errors since both load independent friction torque and load dependent friction torque do not have a constant value of friction coefficient with respect of speed and load. Petry-Johnson et al. [5] subtracted all load independent losses from total loss to avoid an error in the load independent bearing friction loss. However, an error still appears using an average friction coefficient of bearings to calculate the load dependent bearing friction torque.

Similar curves for the total bearing friction torque and rotational speed appeared in Houpert [14], including different bearing friction models. Therefore, the curve obtained in this paper is not caused by experimental error. It is a general behaviour of bearings not only of cylindrical roller bearings but also of tapered roller bearings and ball bearing.

Although this paper is mainly focused on bearing radial load, Söndgen et al. [12] show that the relationship between total friction torque caused by axial load and rotating speed is similar to the curve of total friction torque caused by radial load and rotating speed. Therefore, the effect of radial load and axial load on bearings could be related, and this is worthy of further investigation.

6.3. Modelling

The new values of f_0 in Harris model are shown in Table 4. The bearing zero-load friction torque may be influenced by the geometry of the test rig, which means the new values of f_0 maybe only suitable for the test rig used in this paper. However, the Harris model fits the experimental results best. This implies that the load independent friction torque part of the Harris model is more suitable for NJ 406 cylindrical roller bearings than the other two models.

In addition, there are other ways to develop bearing load independent friction torque models. For example, fluid mechanics were used by Liebrecht et al. [15]. In this paper, a modified Harris model was chosen for the zero-load bearing friction torque model and it is close to the experimental data. However, the value of f_0 is not a constant in the low speed region. Therefore, fluid mechanics can perhaps be used in the future for load independent friction torque analysis.

By comparing the load dependent friction torque of the SKF model and the new model, the first part of the new model ($a \cdot n$ in equation (13)) is similar to M_{rr} in the SKF model. The second part (b/n in equation (13)) is similar to M_{sl} in the SKF model. M_{rr} dominates in high

speed region and M_{sl} dominates in the low speed region, just the same as in the new model. In addition, the Monte Carlo simulation showed a good result in Fig. 7. Thus, by using the new model and the confidence bounds, the predicted values are always within two standard deviations of the experimental results. The values of the three parameters were also calculated in other conditions like changing oil types and oil levels. The differences when changing oil type and oil level are small, but significant when changing load. This is consistent with the results from load dependent friction torque experiments.

Finally, from Fig. 8, the combination of the optimized zero-load friction torque model and the new load dependent friction torque model accurately predicts the total friction torque of bearings.

7. Conclusions

After performing many bearing friction experiments and analysing the experimental data, a new load dependent friction torque model for the NJ 406 cylindrical roller bearings used in this back-to-back gear test rig was developed. The goal of this research mentioned in the introduction were reached, and the main findings are summarized below:

- Oil temperature, oil level, and oil type have a small effect on the zero-load friction torque.
- Oil level and oil type have a limited effect on the load dependent friction torque of bearings.
- The mathematical model developed can be used to predict the load dependent friction torque of NJ 406 cylindrical roller bearings.
- By combining the load independent friction torque from the Harris model using a new f_0 and the new load dependent friction torque model, the friction torque of the bearings used in the back-to-back gear test rig can be predicted accurately within the range of rotating speed and bearing load in this research.

Acknowledgment

Thanks to Ola Harström, Alexander Jonsson, Victoria Magnerius and Sofie Strand students at the department of Machine Design, KTH for their project course work in adapting the FZG gear test rig to a bearing test rig.

Appendix

Table 7. Values of parameters in the SKF model for NJ 406 cylindrical roller bearings

Name of parameters	Value of parameters for NJ 406 roller bearings
K_{roll}	$6.63 \cdot 10^{-12}$
C_w	0.6678
l_D	1.2458
f_t	$\begin{cases} \sin 0.5t & when\ 0 \le t \le \pi \\ 1 & when\ \pi < t < 2\pi \end{cases}$
R_s	$660.96(t - \sin t)$
t	$2\cos^{-1}\frac{36-H}{36}$ (Depends on oil level H)
f_A	0.51
φ_{ish}	$\frac{1}{1+3.512\cdot10^{-7}n^{1.28}\nu^{0.64}}$ (Depends on rotating speed n and kinematic viscosity of oil ν)
φ_{rs}	1
G_{rr}	$0.0193F_r^{2.41}$ (Depends on radial load F_r)
G_{sl}	$0.09F_r$ (Depends on F_r and axial load F_a equal to 0)
μ_{sl}	$0.02 + 0.13\phi_{bl}$
φ_{bl}	$\frac{1}{e^{1.56\cdot10^{-6}(n\nu)^{1.4}}}$ (Depends on n and ν)

Table 8. Notation

Name	Meaning	Name	Meaning
a	Values of parameters calculated by least squares method (-)	M_f	End-flange friction torque in the Harris model (Nm)
B	Bearing width (mm)	$M_{independent}$	Load independent bearing friction torque or zero load friction torque in experiments (Nm)
b	Values of parameters calculated by least squares method (-)	M_{rr}	Rolling frictional moment (Nm)
C	Value of confidence bound (-)	M_{seal}	Frictional moment of seals in SKF model (Nm)
C_w	A parameter in the SKF model (-)	M_{sl}	Sliding frictional moment (Nm)
c	Values of parameters calculated by least squares method (-)	M_v	Load independent friction torque in the Harris model (Nm)
d	Representing the value of parameter a, b and c in the equation of calculating confidence bounds (-)	M_0	Load independent friction torque in the Palmgren model (Nm)
d_m	Pitch-circle diameter of the set of rolling elements (mm)	M_1	Load dependent friction torque in the Palmgren and Harris models (Nm)
e	Base of natural logarithm (-)	n	Speed of rotation (r/min)
F_a	Bearing axial load (N)	P_0	Static equivalent bearing load in the Palmgren model (**kg**)
F_r	Bearing radial load (N)	p	Difference between atmospheric pressure and the vaporization pressure of the oil in Palmgren model (**kg/mm²**)
F_β	Resultant load of bearing in the Harris model (N)	R_s	A parameter in the SKF model (-)
f_A	A parameter in the SKF model (-)	S	Square error (-)
f_f	A parameter in the Harris model (-)	S_1	A parameter in the SKF model (-)
f_t	One of parameters in SKF model (-)	S_2	A parameter in the SKF model (-)

Name	Meaning	Name	Meaning
f_0	Factor depending on bearing design and lubricant method in the Palmgren model (for cylindrical roller bearing = 2~3) and the Harris model (for cylindrical roller bearing = 2.2~4) (-)	s	Standard deviation of data used in calculating confidence bounds (Nm)
f_1	Factor depending on bearing design and relative bearing load in the Palmgren model (for cylindrical roller bearing = 0.00025~0.0003) and the Harris model (for cylindrical roller bearing = 0.0002~0.0004) (-)	t	A parameter in the SKF model (-)
G_{rr}	Variable depending on the bearing type, dm, Fr and Fa (-)	V_M	Drag loss factor (-)
G_{sl}	Variable depending on bearing type, dm, Fr and Fa (-)	z	Z value in normal distribution (-)
g_1	Factor depending on the direction of load in the Palmgren model (-)	α	Contact angle between roller element and bearing rings (º)
H	Oil level (mm)	β	Exponent depending on the seal type and the bearing type in the SKF model (-)
J	Jacobian matrix (-)	η	Dynamic viscosity (mPas)
K_L	Roller bearing type related geometric constant (-)	μ_{bl}	Coefficient depending on the additive package in the lubricant (-)
K_{roll}	Rolling element related constants (-)	μ_{EHL}	Sliding friction coefficient in full-film conditions (-)
K_{rs}	Replenishment constant: for low level oil bath and oil jet lubrication =3×10^{-8}, for grease and oil-air lubrication =6×10^{-8}	μ_{sl}	Sliding friction coefficient (-)
K_{S1}	Constant depending on the seal type and the bearing type and size (-)	ν	Kinematic viscosity (cSt)
K_{S2}	Constant depending on the seal type and the bearing type and size (-)	ν_0	Kinematic viscosity in the Harris model (cSt)
K_Z	Bearing type related geometric constant (-)	Φ_{ish}	Inlet shear heating reduction factor (-)
l_D	A parameter in the SKF model (-)	Φ_{rs}	Kinematic replenishment reduction factor (-)
M	Total bearing friction torque (Nm)	φ_{bl}	Weighting factor for the sliding friction coefficient (-)
$M_{dependent}$	Load dependent bearing friction torque (Nm)	ω	Angular velocity of the bearing rings in relation to each other in the Palmgren model (rad/s)
M_{drag}	Frictional moment of drag losses, churning, splashing etc. in SKF model (Nm)		

Table 9. Abbreviations

Name	Meaning
PAO std	Poly-alpha-olefin standard oil
PAO LV	Poly-alpha-olefin low viscosity oil
VG100	Rape oil of ISO VG100

Reference

[1] A. Palmgren, G. Palmgren, and SKF Industries Inc., Ball and roller bearing engineering, 3rd ed. Philadelphia: SKF industries, 1959, p. 264.

[2] T. A. Harris, Rolling bearing analysis, 3rd ed. New York: J. Wiley, 1991, p. xviii.

[3] SKF, Rolling Bearings. 2012.

[4] B.-R. Höhn, K. Michaelis, A. Doleschel, F. Joachim, and Z. Friedrichshafen, "Method of Determining the Frictional Behaviour of Lubricants Using a FZG Gear Test Rig," 2002.

[5] T. T. Petry-Johnson, A. Kahraman, N. E. Anderson, and D. R. Chase, "An Experimental Investigation of Spur Gear Efficiency," Journal of Mechanical Design, vol. 130, no. 6, p. 62601 (10), 2008.

[6] K. Michaelis, B.-R. Höhn, and A. Doleschel, "Lubricant Influence on Gear Efficiency," presented at the ASME 2009 International Design Engineering Technical Conferences and Computers and Information in Engineering Conference, San Diego, California, USA, 2009.

[7] C. M. C. G. Fernandes, P. M. T. Marques, R. C. Martins, and J. H. O. Seabra, "Gearbox power loss. Part I: Losses in rolling bearings," Tribology International, vol. 88, pp. 298-308, 2015.

[8] S. Sjöberg, M. Sosa, M. Andersson, and U. Olofsson, "Analysis of efficiency of spur ground gears and the influence of running-in," Tribology International, vol. 93, no. Part A, pp. 172-181, 2016/01/01/ 2016.

[9] M. Tu, "Validation and modeling of power losses of NJ406 cylindrical roller bearings," Master thesis report MMK 2016:163 MKN 179, Department of Machine Design, KTH, Stockholm, 2016.

[10] R. Striebeck, "Die wesentlichen eigenshaften der gleit und rollenlager," Zeitscrift des Vereines Duetcher Ingenieure, vol. 46, pp. 1342-1348, 1902.

[11] MathWorks. (2016, July 27th). Confidence and Prediction Bounds. Available: http://se.mathworks.com/help/curvefit/confidence-and-prediction-bounds.html?s_tid=gn_loc_drop

[12] S. Söndgen and W. Predki, "Power Loss and Axial Load Carrying Capacity of Radial Cylindrical Roller Bearings," Power Transmission Engineering, p. 6, June 2013.

[13] J. Koryciak, "Einfluss der Ölmenge auf das Reibmoment von Wälzlagern mit Linienberührung," ISBN, vol. 3, no. 89194, p. 178, 2007.

[14] L. Houpert, "Ball Bearing and Tapered Roller Bearing Torque: Analytical, Numerical and Experimental Results," Tribology Transactions, vol. 45, no. 3, pp. 345-353, 2002.

[15] J. Liebrecht, X. Si, B. Sauer, and H. Schwarze, "Calculation Approach of Drag and Churning Losses of Rolling Bearings," presented at the Bearing World, 12-13 April, 2016.

Boundary layers on bearing raceways subject to operating conditions with high risk of white etching cracks related premature rolling contact fatigue

Dieter Lipinsky[1], Christian Muhmann[1], Florian Pape[2], Giovanno Möbes[2], Gerhard Poll[2], Heinrich F. Arlinghaus[1]

[1] *Physikalisches Institut, Westfälische Wilhelms-Universität Münster/ dieter.lipinsky@uni-muenster.de*
[2] *Institut für Maschinenkonstruktion und Tribologie (IMKT)/ pape@imkt.uni-hannover.de*

To achieve a maintenance free run of wind mills, the inserted bearings play a main role. A failure of a bearing results in a loss of produced energy and a cost intensive repair, factors avoiding a profitable operation. Specific challenges are early failures due to so called White Etching Cracks (WEC). These cracks appear in the bearings subsurface within a depth of a few hundred microns. An influence to these cracks is seen in the diffusion of hydrogen into the bearings surface. To avoid the diffusion, boundary layers can act as a barrier. These boundary layers have a high influence on the bearings fatigue life. Due to the test conditions these layers can develop in a positive or negative way. The chemical composition and thickness depends on the bearings load, material, geometry, lubrication, as well as lubrication conditions. Using a lubricant with a low additivation tending to WEC on axial bearing washers in a FE-8 test, the influence of the operating conditions on the early failure of bearings due to WECs was investigated. The mechanical and the chemical composition of the boundary layers on the washers' surfaces were studied.

Keywords – ToF-SIMS, white etching cracks, micro tribology, boundary layers, micro pin-on-disk

1. Introduction

To investigate boundary layers on bearing surfaces, nanoindentational methods and micro pin-on-disk tests provide data on the micro-mechanical material behavior. Previously boundary layers influenced by polymer additivated greases were investigated by nanoindentational studies [1]. To conclude on the frictional properties of these extreme thin layers with a thickness of a few ten nanometers, micro pin-on-disk tests were performed. These tests allow to measure the frictional properties under lowest loads without scratching into the surface [2].

Due to its ability to simultaneously detect all elements including their isotopes and complex molecules with high sensitivity and an information depth less than one nanometer, time-of-flight secondary ion mass spectrometry (ToF-SIMS) is ideally suited to analyze these boundary layers, including the adsorptive layers formed from oil additive components [3]. Employing different modes of operation, like imaging the lateral distribution of elements and molecules on the surfaces of boundary layers or determining the depth distribution of elements within a tribofilm by performing depth profile analysis, ToF-SIMS can be used to analyze the boundary layers formed under tribological conditions.

Figure 1: Setup of axial bearing type 81212.

Axial bearings were submitted to FE-8 tests at the Institute of Machine Design and Tribology (IMKT), Leibniz Universität Hannover. As lubricant a low additivated oil was used, for this oil WECs were achieved under typical test conditions (tested under 100 °C). The tests were conducted in the mixed lubrication regime using an axial load of 60 kN. Three different temperatures (80 °C, 100 °C, and 120 °C) were applied during the test on the housing washer by controlling the oil temperature. A run in for 24 h at 500 rpm with subsequent 176 h test run at 750 rpm was conducted. During the tests, the torque and temperature were measured. A bearing failure before reaching the desired total of 200 h was determined by vibrational measurements. An axial bearing of the tested type (type 81212) is depicted in Figure 1. For this kind of bearing it has to be regarded, that on the middle of the raceway no slip occurs between roller and bearing washer, while asides the raceway higher slip is achieved [4]. Under typical test conditions (100 °C) these bearings tend to subsurface cracks and an early failure. These cracks can be achieved on the bearing washers itself or even on the rolling elements (Figure 2). Figure 2a depicts a SEM (Secondary Electron Microscopy) image of a crack in the subsurface region of a rolling element with a depth of a few hundred microns. Figure 2b shows a crack on top of the surface of the rolling element.

a)

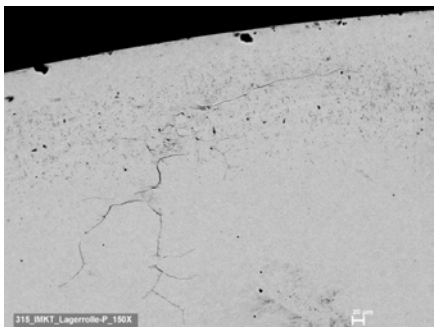

b)

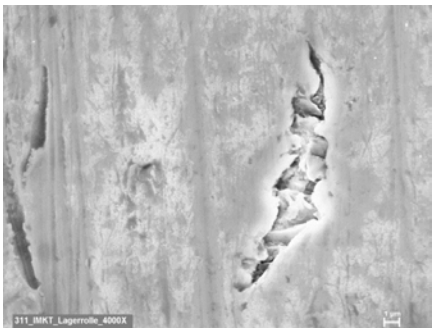

Figure 2: Subsurface cracks on rolling element, a) SEM image of subsurface crack; b) SEM image of crack on top of the surface

2. Bearing life test

Each of the axial bearings subjected to the life test was lubricated with a less additivated oil containing ZDDP additives and mounted in the FE-8 test rig. The oil was supplied at a constant flow rate of 0.1 l/min. Figure 3a depicts the setup of the test rig. A tested axial bearing washer (after test with boundary layers) is shown in Figure 3b. The test is specified in the standard DIN 51819 for the mechanical-dynamic measurement of rolling contact bearing lubricants. The pre-load to the bearings was engaged with disk springs. To stabilize the bearing temperature the test head was ventilated.

a)

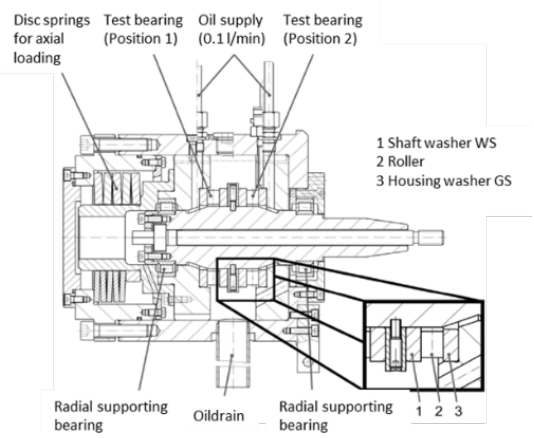

b)

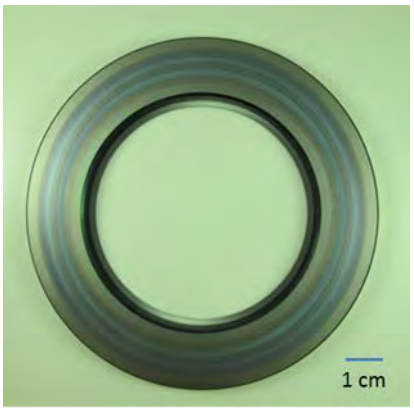

Figure 3: FE-8 test rig for bearing life test. a) head of FE-8 test rig for characterization of rolling contact lubrication, b) axial bearing washer with boundary layers after test.

The bearing life test consists of a run in phase for 24 h at 500 rpm followed by a 176 h test run at 750 rpm. A bearing failure before reaching the desired total of 200 h running time was determined by vibrational measurements. During the tests, the frictional torque and temperature were measured. For the tests, the temperature and load were varied to achieve a change in the chemical kinetics on the bearing surfaces. Thus, boundary layers of different properties should be generated. The test conditions for the axial bearings are shown in Table 1. For the bearings tested at 100 °C the test duration was 50:12 h. For the bearings under a higher temperature of 120 °C the test duration was 200 h. With a reduced temperature of 80 °C the test duration was 200 h.

bearing	axial load in kN	temperature in °C	test duration in h:min
TB 60-100	60	100	50:12
TB 60-120	60	120	200
TB 60-80	60	80	200

Table 1: Test conditions for axial bearings.

2.1. Nanoindentational test setup

The nanomechanical properties of the bearing surfaces were analyzed applying a Hysitron TriboIndenter®. The test setup is based on a 3D-transducer with a three-plate capacitor for vertical displacement and two three-plate capacitors for horizontal displacement. A triangular diamond Berkovich tip (with a tip radius of approx. 100 nm) is used to measure the Young's Modulus and the hardness. The tip is mounted on an elastically suspended pick-up electrode which is placed between the capacitors. The material behavior of boundary layers is characterized by load-displacement curves. A load of 1 mN was applied to the tip. The system allows to measure the hardness of thin films, as well as pure substrates [5]. The hardness values were calculated with the unloading curve of the indentation tests applying the method of Oliver and Pharr [6]. For the hardness measurement twelve indents were performed at one area and the average value was calculated.

2.2. Micro pin-on-disk tester

The micro pin-on-disk tests were carried out with a tester, which is based on a modified Center for Tribology (CETR) Olympus HDI reliability spin-stand. The tester is shown in Figure 4. The test stand was originally used to investigate the head-to-disk interface for hard disk drives. This allows to apply continuous start-stop (css) test cycles, a test commonly used for hard disk drive tests. The tester allows to measure also the frictional properties of coatings and substrates [7].

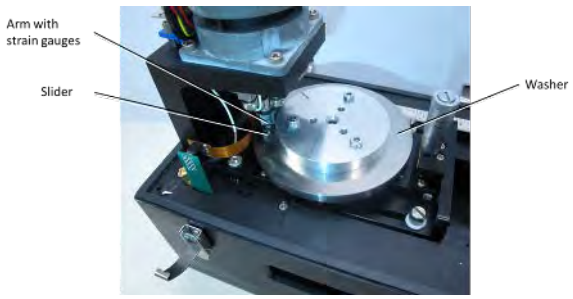

Figure 4: Setup of the micro pin-on-disk tester.

For the tests, axial bearing washers are used as counterparts. As pin a sapphire half ball was attached with adhesive to the slider of a HDD recording head (head gimbal assembly – HGA) (Figure 5). The diameter of the test specimen is 500 microns. Next, the slider was mounted on the testers arm and exposed to the counterpart. The desired normal force of 30 mN is applied by a vertical displacement of the slider in the tester.

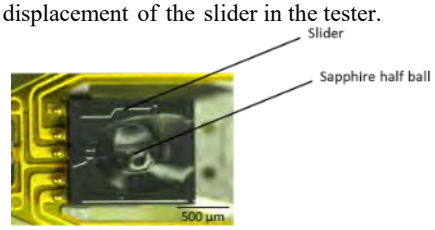

Figure 5: Sapphire half ball mounted on flexure.

The arm with the mounted slider represents the stationary part of the micro pin-on-disk tester, while the axial bearing washer is rotating at 1 rpm. The frictional force during sliding is measured by strain gauges integrated in the testers arm. During the test cycles the coefficient of friction was recorded. To investigate the raceway on the bearing washers, the sapphire half ball was set on different radial positions on the bearing washer to be investigated.

3. Experimental results

3.1. Nanoindentational test results

The bearings TB 60-100 were tested under 60 kN load and 100 °C in the FE-8 test rig. After the macroscopic test the hardness of the bearing´s surface was measured by nanoindentation on one of the bearing washers. The measured hardness on the surface is shown in Figure 6. The measurement positions on the bearing washer start at the outer rim of the bearing. The hardness measurement was evaluated for the no slip zone in the middle of the raceway and the slip zone on both sides of the raceway. On the raceway the hardness is reduced. In the middle of the raceway, where pure rolling of the rolling bearing elements appears, the hardness increases, but remains lower than besides the raceway.

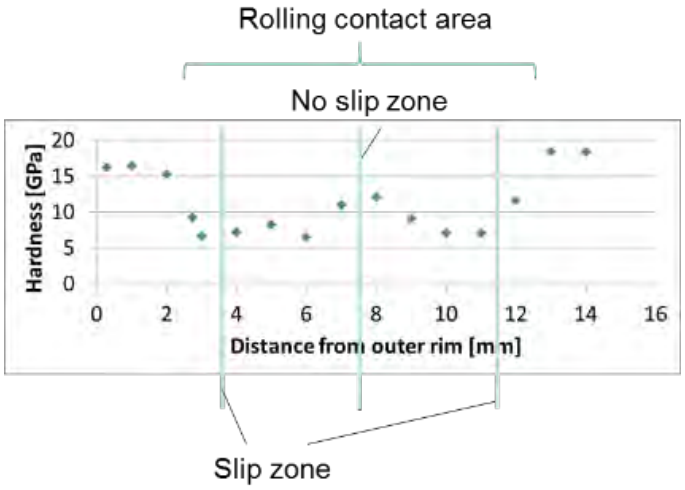

Figure 6: Hardness measurement on the surface of a washer of the bearing TB 60-100 (100 °C, 60 kN load, each point is an average value of 12 indents).

The average hardness on the raceways of the washers for all bearings on the no slip zone is depicted in Figure 7. Figure 8 shows the average hardness on the slip zone. Washer 2 of the bearing TB 60-120 and washer 3 of the bearing TB 60-80 (both with the longest test duration) feature the lowest hardness values. Washer 1 of the bearing TB 60-100 (with the shortest test duration) shows the highest hardness on the race-ways

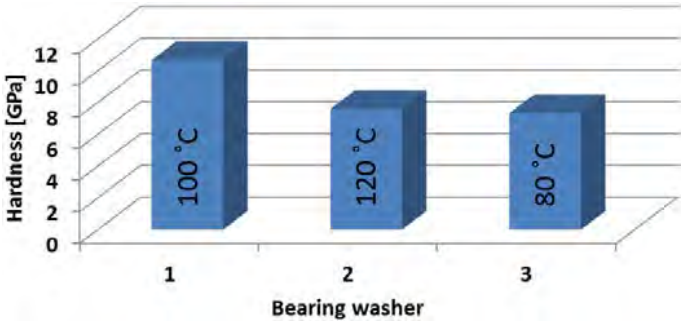

Figure 7: Average hardness on the no slip zone of the tested bearings.

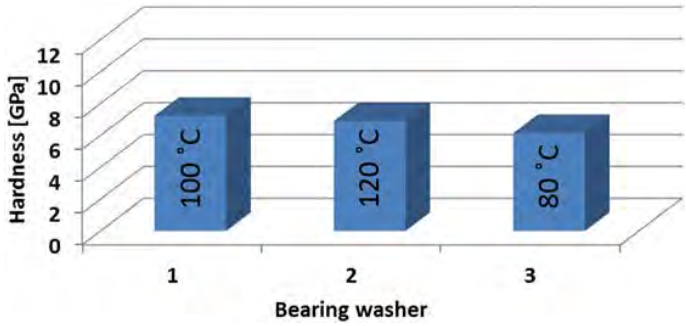

Figure 8: Average hardness on the slip zone of the tested bearings.

For the bearings TB 60-120 and TB 60-80 the hardness of the washers decreases slightly from the no slip zone to the slip zone. The reduced hardness for the bearings TB 60-120 and TB 60-80 can be explained with boundary layers featuring a softer surface. In case of the washer 1 (TB 60-100), the hardness decreases significantly. The decrease in hardness can be correlated to higher formed boundary layers with lower deformation resistance due to slippage.

3.2. Micro pin-on-disk test results

For the model tribosystem sapphire half ball / bearing washer the CoF (Coefficient of Friction) was measured with the micro pin-on-disk tester. The CoF of the model tribosystem with a washer from bearing TB 60-100 for different radial positions on the washer are presented in Figure 9. It is possible to separate the CoF to the no slip zone and the zones with high slip on the bearing washer. The CoF vary between 0.09 and 0.10. On the outer side of the bearing washers the values are slightly higher. On the inner side of the bearing washers and within the no slip zone the values are slightly lower.

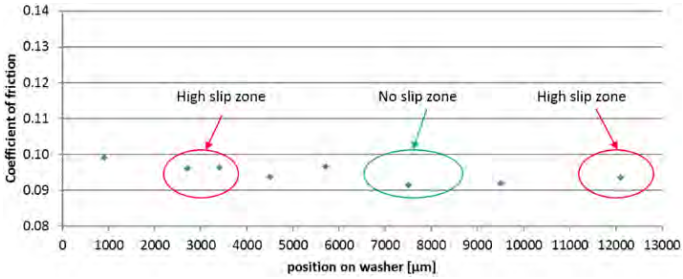

Figure 9: CoF on the surface for the bearing washer TB 60-100 (100 °C, 60kN load).

The CoF of the model tribosystems for the no slip zones are shown in Figure 10. Figure 11 depicts the CoF on the zones of high slippage for the tested bearings. On the no slip zone, where pure rolling of the roller exists, the CoF is highest for the model tribosystem with the bearing washer tested under highest temperature (TB 60-120). The model tribosystem with the washer of the bearing TB 60-80 tested at the lowest temperatures shows the lowest CoF, which is slightly lower than the CoF of the model tribosystem with the washer of the bearing TB 60-100 tested under 100 °C. On the high slip zones of the bearings, the model tribosystem with the washer of the bearing TB 60-100 shows the lowest CoF.

Figure 10: CoF on no slip zones.

The CoF on the zones of high slip shows an increased CoF compared to the no slip zones for the washers TB 60-100 and TB 60-80. In case of the bearing washer TB 60-120 the CoF is decreased slightly comparing the no slip zone to the high slip zone. On the zones of high slip boundary layers with higher CoF (due to adhesion) could be proven for all tested bearings. In case of the bearing TB 60-120 such boundary layers also occur on the slip zone.

Figure 11: CoF on slip zones.

3.3. Results of mass spectrometric analysis

The chemical compositions of unloaded and loaded areas on the washer surfaces and loaded areas on the rolling elements were determined at the Physikalisches Institut, Westfälische Wilhelms-Universität Münster, using a ToF-SIMS instrument comparable to the ToF-SIMS IV of IONTOF GmbH. It is equipped with a bismuth liquid metal ion gun for high-resolution imaging and a noble-gas electron-impact ion gun for sputter erosion in depth-profile analysis using dual beam mode.

Time-of-Flight Secondary Ion Mass Spectrometry (ToF-SIMS) is a surface analytical method for determining the atomic and molecular composition of surfaces of solid state materials. Using this method, the surface of a solid state target is bombarded with energetic primary ions causing the sputtering of the outermost monolayers of the target. Amongst the emitted particles positively or negatively charged atoms or molecules, the so called secondary ions, can directly be analyzed according to their mass-to-charge ratio determined via a mass spectrometer [8-10].

The special merits of ToF-SIMS are a high detection probability combined with a high surface sensitivity. The main focus of applications are in trace element analysis, the determination of lateral distributions of atoms and molecules on the surface and the analysis of the composition of boundary layers using depth profiling. Due to this, ToF-SIMS is ideally suited for the analysis of tribologically build up boundary layers, including the adsorptive layer formed from oil additive components, and to advance the understanding of the interaction of all materials involved [11-15].

In preparation for ToF-SIMS-analysis, the bearing washers were cut into four pieces whereas the rolling elements could be analyzed on the whole. Prior to the analysis, the washer segments and the rolling elements were cleaned in an ultrasonic bath (3 x 5 min) using n-hexane (SupraSolv) to remove the adhering oil film and expose the adsorbate layer.

Figure 12 shows a section of a bearing washer (left) and a rolling element (right) after cleaning. On each washer the lateral distribution of atoms and molecules on the surface was determined by applying the large area mapping mode of operation on an area of 14.7 mm x 1.8 mm covering the whole rolling contact area, including adjacent areas outside the raceway. In order to avoid exceeding the static limit, two large area maps were carried out analyzing positively as well as negatively charged secondary ions. Note that exceeding the static limit results in significant surface damage. Both analyzed areas are depicted in Figure 12.

In addition, two sets of eleven depth profiles each analyzing positive secondary ions and negatively charged ions were carried out. The position of those depth profiles (one outside the raceway on the outer side of the washer, nine inside the raceway and one outside the raceway on the inner side of the washer) are shown numbered in Figure 12 as well.

Due to their curved surfaces, four rolling elements of each test bearing were analyzed. Two elements were used applying large area mapping (8.4 mm x 0.6 mm) of positively and subsequently negatively charged secondary ions. The remaining two elements were used for depth profiling on five spots. The positions where those analyses were performed are depicted in Figure 12 as well.

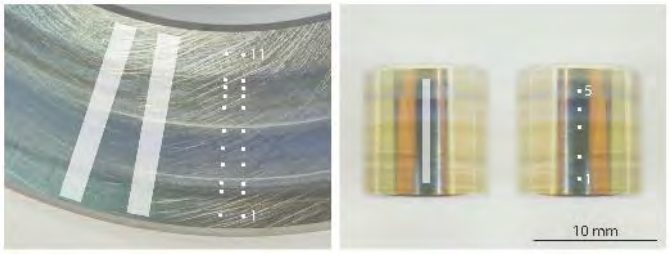

Figure 12: Photographs of a washer segment (left) and a rolling element (right) depicting the positions of large area mappings and depth profile analysis.

3.4. Large area mappings

Figure 13 shows the distribution of selected positive (left) and negative (right) secondary ions obtained from large area mapping of the washer surface of test bearing TB 60-100. The position of the raceway is marked in light-grey, however the relative position depends on the backlash of the rolling elements in the cage which is about ± 250 µm. The dark-grey background marks the whole area of 15.8 mm of the polished washer surface. The outer rim of the washer is indicated by the position 0 mm.

TB 60-100

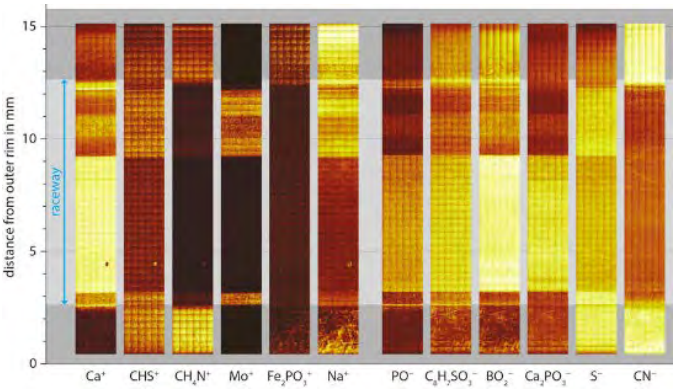

Figure 13: Distribution of selected positive (left) and negative (right) secondary ions obtained from large area mapping of the washer surface of test bearing TB 60-100.

As can be seen, several secondary ion signals show inhomogeneous distributions with clearly separated areas inside the rolling contact area. Some sulfur-containing signals, like CHS^+ or S^-, show opposite behavior with respect to calcium-containing signals like Ca^+ or $Ca_2PO_3^-$. For example, reduced signal intensities of Ca^+ in areas with a distance of about 2.5 to 3.2 mm and 9.3 to 12.6 mm with respect to the outer rim of the washer correspond to enhanced signal intensities of S^-. By comparison, in an area of about 3.2 mm to 9.3 mm with respect to the outer rim, increased Ca^+-signal intensities correlate with reduced S^--intensities.

TB 60-120

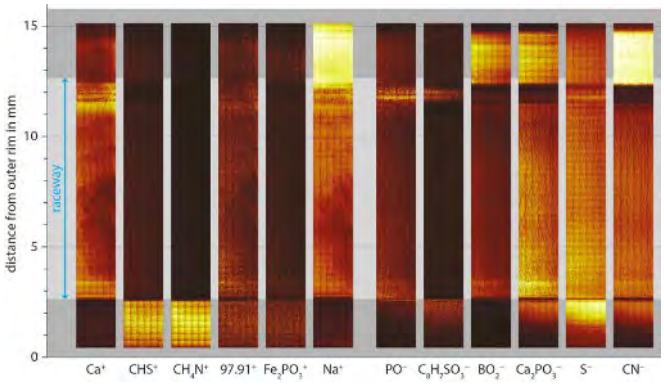

TB 60-80

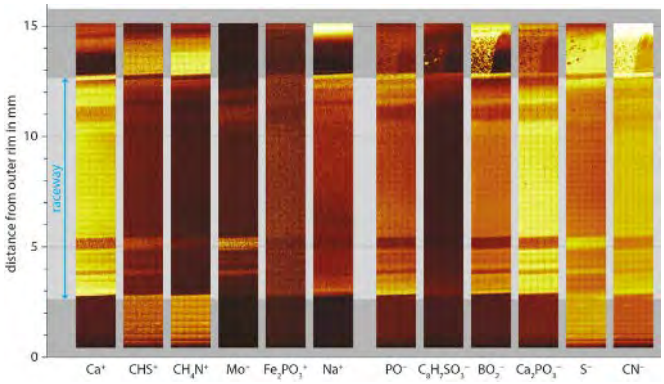

Figure 14: Distribution of selected positive (left) and negative (right) secondary ions obtained from large area mappings of the washer surfaces of test bearings TB 60-120 (top) and TB 60-80 (bottom).

Comparing these results with those obtained from large area maps performed on the washer surfaces of test bearings TB 60-120 and TB 60-80, depicted in Figure 14, some differences as well as similarities can be seen. Looking at the washer surface of TB 60-120, all signals show a much more uniform distribution inside the rolling contact area of the washer apart from areas near to both edges of the rolling contact area. On the washer surface of TB 60-80 some areas show inverted signal intensities inside the rolling contact area comparing sulfur- and calcium-containing signals, similar to the behavior observed on the washer surface of TB 60-100.

The correlation or noncorrelation of some secondary ion signals with respect to the position on the washer surface can be seen in Figure 15 depicting the results of line scan analyses of selected secondary ions covering the whole large area map obtained from the washer surfaces of TB 60-100, TB 60-120 and TB 60-80. To provide better orientation, the corresponding large area map of the Ca^+-signal as a function of distance from the outer rim is displayed above each diagram. The equidistant ripples are caused by a measurement artifact due to slightly reduced detection sensitivity at the edges of each small image area of 300 x 300 µm^2.

Looking at the results obtained on the washer surface of TB 60-100, it can be seen that within the rolling contact area the Ca^+-signal shows areas with different intensity levels and steep transitions. From a high resolution image obtained at the steep decrease at a distance of 9.3 mm from the outer rim, a transition width of about 45 µm was calculated. Its slope correlates with that of the $Ca_2PO_3^-$-signal. In contrast, it is anticorrelated with the slope of the S^--signal. In some areas at both outer sides of the raceway the intensity level of the S^--signal even exceeded those of the Ca^+-signal.

TB 60-100

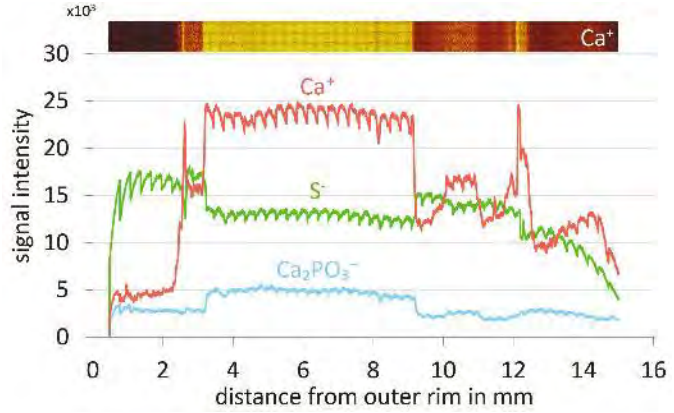

TB 60-120

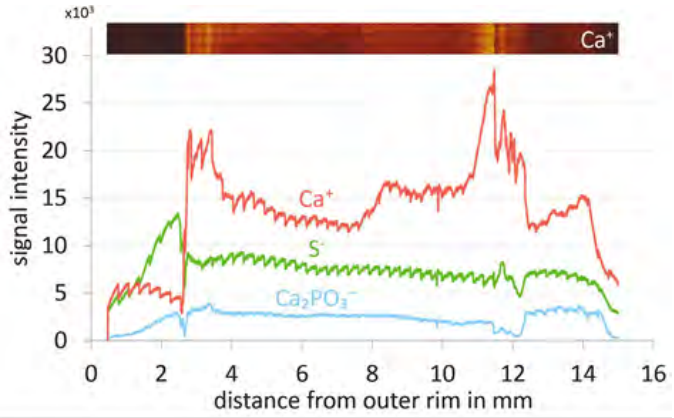

TB 60-80

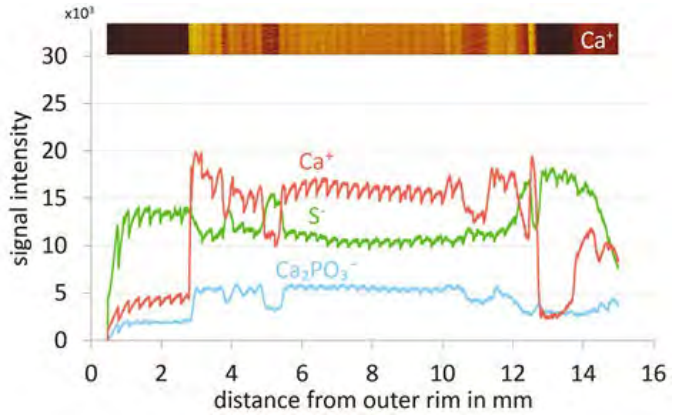

Figure 15: Line scan analyses of selected secondary ions covering the whole large area map obtained from the washer surfaces of TB 60-100 (top), TB 60-120 (middle) and TB 60-80 (bottom).

In contrast to this, within the raceway of TB 60-120 no such inverse behavior comparing the Ca^+-and S^--signal can be seen and the intensity level of the Ca^+-signal clearly exceeded those of the S^--signal at the washer surface. In addition, the correlation between the Ca^+- and the $Ca_2PO_3^-$-signal is not as obvious as in the case of TB 60-100, especially looking at the inner edge of the raceway in a distance of about 11.5 mm from the outer rim, where an inverse behavior can be seen. This emphasizes the differences observed in the chemical composition of the surfaces inside the raceway of these bearing washers tested with different bearing temperatures during the FE-8 test.

Looking at the results obtained from the washer surface of TB 60-80, operated with the lowest bearing temperature, similarities can be found compared to TB 60-100. Here too an inverse behavior of the Ca^+-and S^--signal can be seen with some areas where the intensity level of the S^--signal equaled or exceeded those of the Ca^+-signal.

Figure 16 shows a comparison of the lateral distribution of selected positive and negative secondary ions from large area maps of washer segments and rolling elements of test bearings TB 60-100, TB 60-120 and TB 60-80. As mentioned earlier the relative position depends on the backlash of the rolling elements in the cage which is about ± 250 µm.

In most areas of the washer surface of TB 60-100 signal intensities of the selected secondary ions show inverted behavior compared to those obtained from the surface of the rolling element. This occurs with areas on the outer side of the raceway up to a distance of about 8 mm with respect to the outer rim and on the inner side exceeding distances of about 9.3 mm. In between an area with similar behavior with respect to the signal intensity levels can be seen.

With TB 60-120 all selected secondary ion signals show a much more uniform distribution within the rolling contact area of the washer and on the surface of the rolling elements as well. Due to the fact that the outermost rims of the rolling elements could not be analyzed using the large area mapping mode of operation, changes in signal intensity levels observed on both edges of the raceway of the washer surface could not be detected on the rolling elements. In addition, on rolling elements slightly decreasing (Ca^+ and $Ca_2PO_3^+$) or increasing (S^-) intensities from the inner to outer the side of the rolling contact area can be seen, which are comparable to those observed on the washer surface inside the raceway.

With TB 60-80 some areas inside the rolling contact area of the washer show inverted signal intensities comparing sulfur- and calcium-containing signals. Compared to TB 60-100, the surface of the rolling elements also shows some areas with comparable but less pronounced signal intensity inversions. Similarly to TB 60-100, clear similarities or differences between the rolling element and the washer surface are hardly observable.

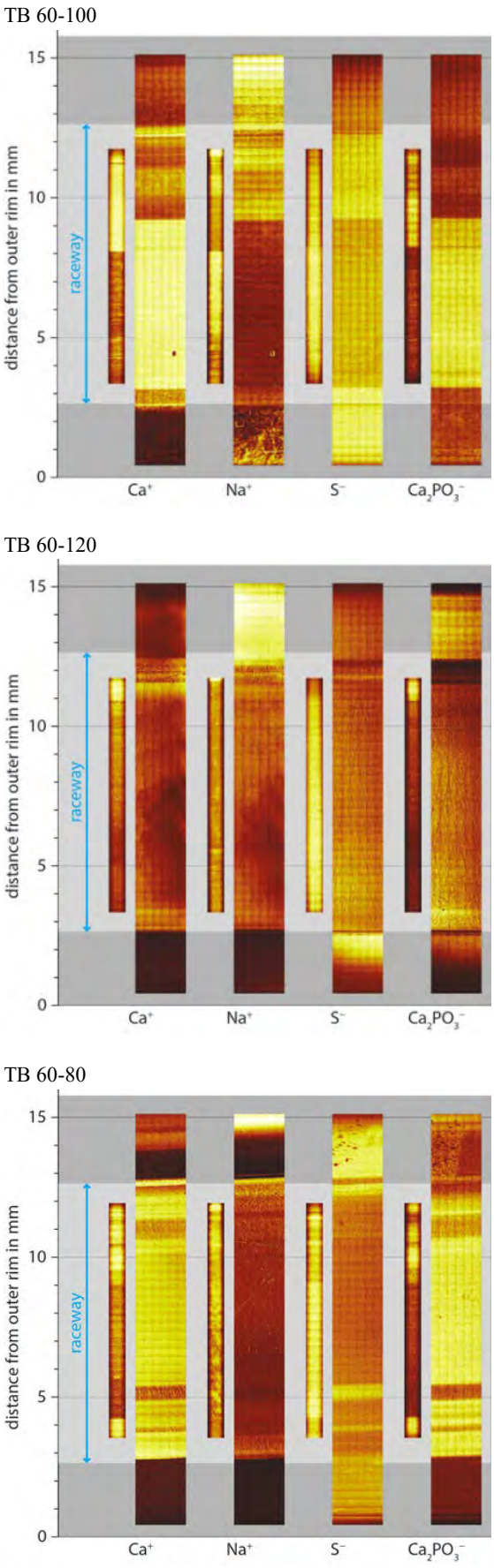

Figure 16: Lateral distribution of selected positive and negative secondary ions from large area maps of washer segments and rolling elements of test bearings TB 60-100 (top), TB 60-120 (middle) and TB 60-80 (bottom).

3.5. Depth Profiling

ToF-SIMS depth profile analyses on selected spots on the washer surface and the surface of the rolling elements were carried out using the so-called dual beam mode. In this mode one ion gun, the so-called sputter ion gun, is used to remove the target surface in order to expose deeper lying layers. Using a second ion gun, the so called analysis gun, a smaller area of the exposed surface within the sputter crater is analyzed applying much lower ion dose densities to avoid exceeding the static limit. Table 2 shows the parameters used for dual beam depth profile analysis on selected spots on the washer surface and the surface of the rolling elements.

	primary ion	ion energy	ion current	area
sputtering	Ar^+	3 keV	20 nA	300 x 300 µm²
analysis	Bi_3^+	25 kev	0.05 pA	50 x 50 µm²

Table 2: Parameters used for dual beam depth profile analysis on selected spots on the washer surface and the surface of the rolling elements.

In order to reduce matrix induced changes of secondary ion yields and sputtering yields during ion bombardment induced removal of tribological loaded boundary layers and bearing base material, all depth profiles were performed using simultaneous oxygen-flooding applying pure ^{18}O-gas with a base pressure of 1 x 10^{-6} mbar. Since the natural abundance of ^{18}O is only 0.200 %, nearly all secondary ions containing ^{18}O were created during depth profile analysis due to the accumulation of ^{18}O at the target surface. Therefore, secondary ion signals containing the isotope ^{16}O can be clearly attributed to oxygen incorporation into the boundary layer during the tribological load applied.

Since the composition of the tribologically formed boundary layer varies highly with depth, no reliable information about the actual sputtering yield is available. Therefore no depth scale was calculated and the time-courses of the intensities of the secondary ion signals are presented as a function of the measured sputter ion dose densities (SPIDDs) applied for the removal of the boundary layers. As a rough estimation concerning the depth, it can be calculated that with the sputter parameters used and assuming constant sputter yield the application of a SPIDD of 1 x 10^{16} ion/cm² would have led to crater depth of about 4.5 nm if applied to a pure iron target. But with a multi component system built up by highly oxidized layers, as it is the case with tribologically formed boundary layers, a clearly reduced and time dependent sputter yield has to be taken into account. The thickness of the depth profiled boundary layers was estimated from where the curves of the decaying Ca^+-signal and the increasing Fe^+-signal intersect. This point corresponds well with those values on the SPIDD scale where in depth profiles of negative secondary ions the $^{31}P^{18}O_3^-$-signal has dropped to about 50 % of its maximum intensity within the boundary layer.

Figure 17 shows the intensities of selected positive (left) and negative (right) secondary ions as a function of applied SPIDDs, obtained from depth profiles performed on selected spots on the washer surface of test bearing TB 60-100.

Fe^+- and $Fe^{18}O_2^-$-signals represent steel substrate and indicate the transition from the tribological boundary layer to the base material. Calcium-, sulfur- and phosphorus-containing signals represent remains of additives. Compared to area 11, where only a low SPIDD was needed to remove the thin boundary layer, higher SPIDDs were needed to reach the crossing point of the Ca^+- and Fe^+-signal curves in areas 7, 5 and 2 within the rolling contact area. Although all areas lay within the raceway in area 7, almost a half of the SPIDD was needed to remove the corresponding boundary layer compared to area 5.

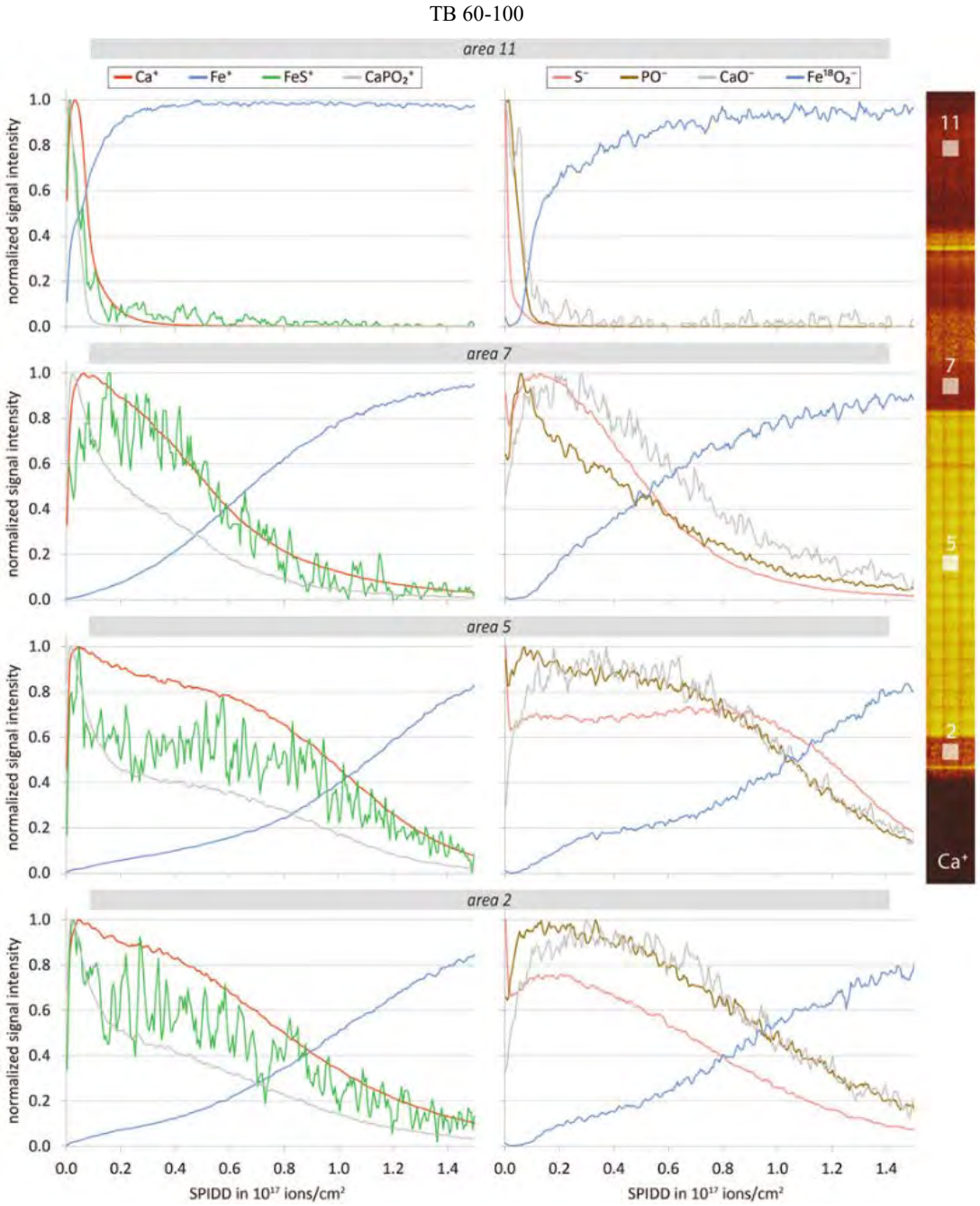

Figure 17: Intensities of selected positive (left) and negative (right) secondary ions as a function of applied SPIDDs, obtained from depth profiles performed on selected areas on the washer surface of test bearing TB 60-100.

In addition, the shapes of the signal curves within the boundary layer differ as well. Whereas in area 5 a clearly formed boundary layer with almost unvarying signal courses can be seen, the shapes of the signals originating from area 7, especially PO^-, show a less developed boundary layer. Furthermore, the results obtained from area 2 suggests that at this point the composition of the surface as well as the boundary layer shows a behavior which is somewhere in between of those of areas 5 and 7. For example, looking at the S^--signal. Its maximum was detected at the surface like in area 5 but after passing a little intermediate maximum a relatively fast decay like that in area 7 can be seen. In addition, the SPIDD needed to reach the crossing point of the Ca^+- and Fe^+-signal curves is somewhat lower compared to that of area 5 but clearly higher compared to that at area 7.

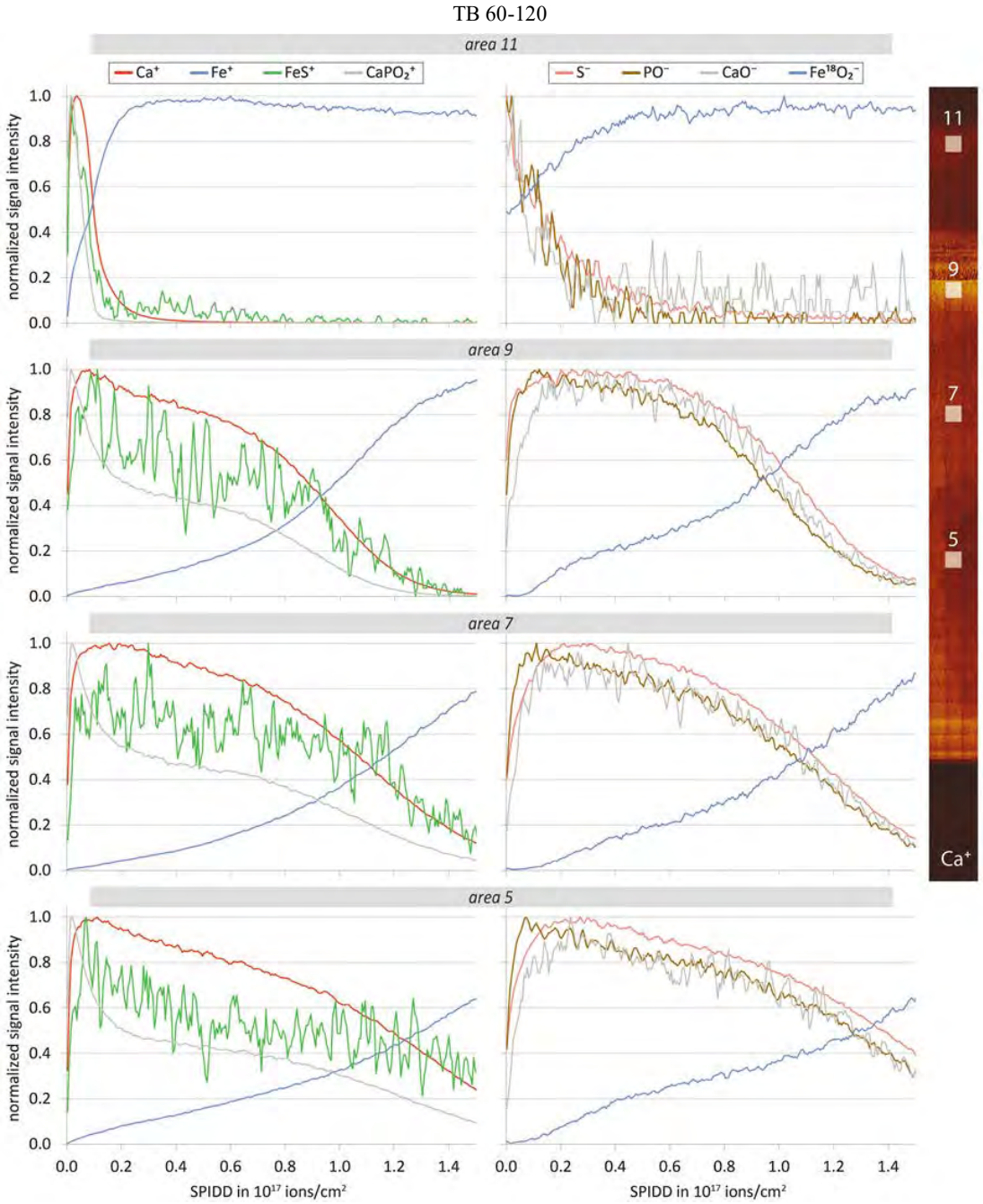

Figure 18: Intensities of selected positive (left) and negative (right) secondary ions as a function of applied SPIDDs, obtained from depth profiles performed on selected areas on the washer surface of test bearing TB 60-120.

Figure 18 shows the intensities of selected positive (left) and negative (right) secondary ions as a function of applied SPIDDs, obtained from depth profiles performed on selected areas on the washer surface of test bearing TB 60-120. Similarly to test bearing TB 60-100, higher SPIDDs were needed inside the rolling contact area to reach the crossing point of the Ca^+-and Fe^+-signal curves compared to the unloaded area 11. In contrast to TB 60-100, starting at the inner edge of the raceway, a clear increase of SPIDD needed to remove the corresponding boundary layers in areas 9, 7 and 5 is observable. In addition, in all areas clearly formed boundary layers with almost unvarying signal courses can be seen.

.

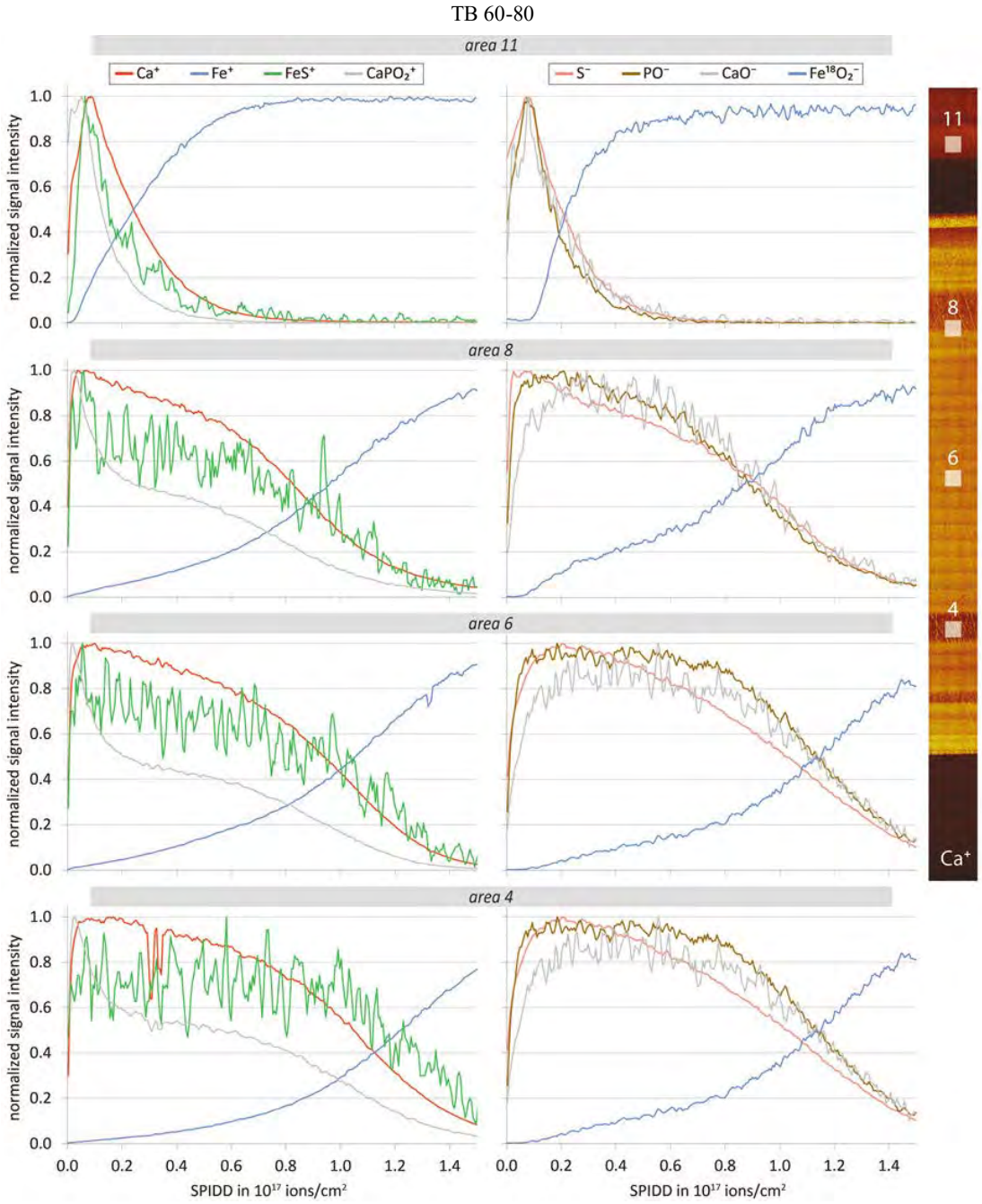

Figure 19: Intensities of selected positive (left) and negative (right) secondary ions as a function of applied SPIDDs, obtained from depth profiles performed on selected areas on the washer surface of test bearing TB 60-80

Figure 19 shows the intensities of selected positive (left) and negative (right) secondary ions as a function of applied SPIDDs, obtained from depth profiles performed on selected areas on the washer surface of test bearing TB 60-80. On lower levels but comparable to TB 60-120, this washer surface shows an increase of SPIDD needed to reach the crossing point of the Ca^+- and Fe^+-signal curves as well, when starting at the inner edge of the raceway.

3.6. Data comparison

Different thicknesses of the boundary layers in the regions presented are confirmed by results of hardness measurements (Figure 20), taking into account, that reduced values of hardness from nanoindentation can be explained by different layer thicknesses of non-metallic layers. For each different test run, this figure shows a comparison of the Ca^+-signal intensity distribution according to ToF-SIMS-large area map analysis, the results of hardness measurements on selected positions (dashed line) and the SPIDDs needed to reach the crossing point of the Ca^+-and Fe^+- signal curves (solid line) as a function of the distance from the outer rim. Note that the hardness values were measured on the opposite washer assuming equal behavior compared to the washer analyzed with ToF-SIMS, which was verified with TB 60-100, where both washers were characterized by nanoindentation. Nevertheless, minor discrepancies cannot be ruled out.

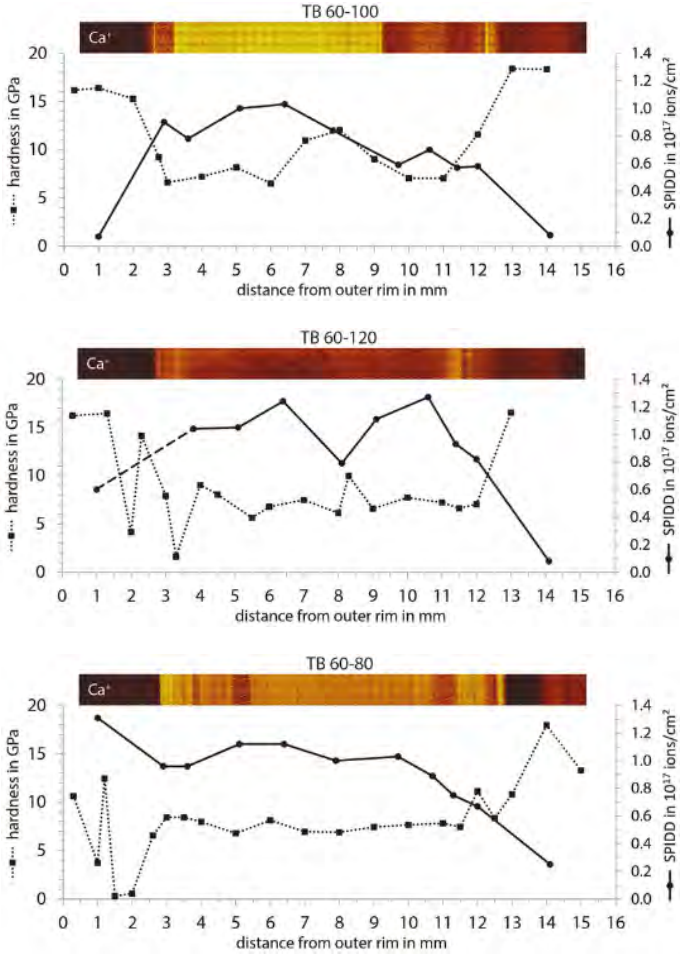

Figure 20: Large area map of Ca^+, hardness values (dashed line) and SPIDDs needed to reach the crossing point of the Ca^+- and Fe^+-signal curves (solid line) as a function of distance from outer rim obtained from the test bearings TB 60-100 (top), TB 60-120 (middle), TB 60-80 (bottom). (Note, due to a measurement artefact while analyzing TB 60-120 the second data point of the SPIDD-curve is missing, indicated by a dashed part of the solid line.)

From the diagrams in Figure 20 it can be seen, that the measured hardness values within the raceway (approx. 2.7 – 12.7 mm from the outer rim) mostly are in the range of 6 to 8 GPa. As can be seen as well, in most of the areas of reduced hardness within the raceways SPIDDs of at least 1 x 10^{17} ions/cm^2 are needed to reach the crossing point of the Ca^+- and Fe^+-signal curves. On the other side, areas where hardness values exceed approx. 8 GPa correlate with regions where corresponding SPIDDs of less than 1 x 10^{17} ions/cm^2 indicate reduced boundary layer thicknesses or layer densities. Nevertheless, with respect to those SPIDDs applied during depth profiles inside the raceway, some differences but also similarities become visible comparing bearing TB 60-120 with the other ones.

On the one hand, considering the course of SPIDD-values needed to reach the crossing point of the Ca^+- and Fe^+-signal curves at spots inside the raceway, all bearings show a slight increase within a distance of approx. 5 mm from the outer rim. In contrast to TB 60-120, where the SPIDD-values remain the same to a large extend up to a distance of approx. 10 mm before decreasing, both, TB 60-100 and TB 60-80, already show an onset of decreasing SPIDD-values at a distance of about 7 mm from the outer rim, which is close to the no slip zone. Although comparable in the point of onset, the SPIDD-values of TB 60-100 show a much steeper decrease compared to those of TB 60-80.

On the other hand, comparing SPIDD-values needed to reach the crossing point of the Ca^+- and Fe^+-signal curves in an area at the outside edge (approx. 2.7 – 5.0 mm from the outer rim) and the inside edge (approx. 10.0 – 12.7 mm) of the raceway one can see, that with all bearings lower SPIDD-values were determined at the inside edge of the raceway. One reason for this could possibly be different amounts of the specific friction energy accumulated at the outer or inner edge of the raceway of this cylindrical roller bearing as proposed in [16].

From those experiments presented here, it can be seen that the combination of microtribological methods and ToF-SIMS can extend the knowledge regarding the build-up of tribological boundary layers. Further combined investigations might clarify to what extend those lateral inhomogeneities in the chemical composition of the boundary layers across the raceway surface observed here can influence their function as a barrier against hydrogen diffusion into the bearings surface.

4. Conclusion

By varying the temperature for the bearing fatigue tests, boundary layers could be developed based on the temperature featuring benefit to the bearing fatigue life. These layers allow to avoide WECs in dependence of the specific test temperature. Under typically test conditions (100 °C) with the applied oil early failure and WECs are achieved with the test bearings.

For the analyzed bearings, the ToF-SIMS large area mappings show inhomogeneous signal distributions within the rolling contact area partially showing well-separated areas. Comparing S^--signal and e.g. calcium-containing signals showed inverted distributions. The signal distributions within the rolling contact area on the washer were sometimes complementary to those on the respective rolling elements. By depth profiling in selected areas a low coverage outside the rolling contact area on the inner side of the bearing washers was detected. Also within the rolling contact area a different formation of boundary layers was detected. The micro-tribological data were combined with the results achieved by ToF-SIMS. The rolling contact areas showed the lowest hardness values corresponding to areas of well-developed boundary layers with enhanced Ca^+/S^--intensity ratios. Those areas, showing intermediate hardness values, correspond to areas of less developed boundary layers with reduced Ca^+/S^--intensity ratios. In case of the boundary layers on those bearings prone to WEC an increased calcium signal intensity was detected across major parts of the rolling contact area. There are also differences between the slip zone and the no slip zone on the bearings. The slip zones feature:

- a thicker boundary layer at the outer side of the rolling contact area,
- an increase in sulfur signal intensity,
- a decrease in calcium signal intensity,
- reduced hardness,
- slightly increased CoF.

The risk of WEC strongly depends on the boundary layers on the surface. The formation of boundary layers is determined by the temperature. Further investigations on influence of the temperature and the load on the boundary layers are ongoing.

Acknowledgement

This work was sponsored in part by the DFG within the research program ”Influence of stress states in rolling bearings on White Etching Cracks”.

References

[1] Pape, F.: Mikrotribologische Untersuchungen an Wälzlagern mit polymeradditiver Fettschmierung, Thesis, Leibniz Universität Hannover, 2011

[2] Pape, F.; Bader, N.; Gatzen, H. H.; Poll, G.: Development of Dry Sliding Friction between 100Cr6 and Sapphire Micro-Balls tested against 100Cr6 Axial Bearing Surfaces, Proceedings of International Tribology Conference, TOKYO 2015, Japanese Society of Tribologists (JAST), 16th-20th September 2015, Tokyo (Japan)

[3] Gatzen, M.; Pape, F.; Poll, G.: Physical properties of boundary layers in angular contact ball bearings lubricated with greases containing polymers., Proceedings of the Institution of Mechanical Engineers, Part J: Journal of Engineering Tribology, 223 (2009) 3, pp. 581-592, ISSN 1350-6501

[4] Loos, J.: Einfluss der Reibbeanspruchung auf die WEC-Bildung in Wälzlagern, 55. Tribologie Fachtagung, Proceedings, Reibung, Schmierung und Verschleiß, Vol. 1, pp. 23/1-23/13, ISBN: 978-3-00-046545-1, 2014

[5] Pape, F.; Dellinger, P.; Moehwald, K.; Poll, G.: Nano- and Micro-Tribological Investigations on Molybdenum Based Coatings for Application on Bearing Surfaces, Proceedings, 7th International Conference on Tribology in Manufacturing Processes, 28.02.-02.03.2016, Phuket, Thailand, ISBN: 978-616-92565-0-2, pp. 95-105

[6] Oliver, W. C.; Pharr, G. M.: An improved technique for determining hardness and elastic modulus using load and displacement sensing indentation experiments, Journal of Materials Research, Vol. 7, Issue 6, 1992, pp. 1564-1583

[7] Pape, F.; Rissing, L.; Gatzen, H. H.: Fabrication and Tribological Investigation of Fullerene C60/C70 Reinforced Epoxy Resin SU-8TM, Tribologie + Schmierungstechnik, 58, 4, 2011, pp. 51-55

[8] Benninghoven, A.; Rüdenauaer, F. G.; Werner, H. W.: Secondary ion mass spectrometry: Basic concepts, Instrumental aspects, Applications and Trends, Wiley, New York, Chemical analysis vol. 86, 1987

[9] Vickerman, J. C.; Briggs, D. (editors): TOF-SIMS: Surface Analysis by Mass Spectrometry, IM Publications, 2nd Edition, 2013

[10] Arlinghaus, H. F.: Static Secondary Ion Mass Spectrometry, in H. Bubert and H. Jenett (editors), Surface and Thin Film Analysis, Wiley-VCH, 2nd Edition, 2011

[11] Minfray, C; Martin, J. M.; De Barros, M. I.; Le Mogne, T.; Kersting, R.; Hagenhoff, B.: Chemistry of ZDDP tribofilm by ToF-SIMS, Tribology Letters, 17(3), 2004, pp. 351-357

[12] Kubo, T.; Fujiwara, S.; Nanao, H.; Minami, I.; Mori, S.: TOF-SIMS analysis of boundary films derived from calcium sulfonate, Tribology Letters, 23(2), 2006, pp. 171-178

[13] Murase, A.; Mori, H.; Ohmori, T.: TOF-SIMS analysis of friction surfaces of hard coatings tested in engine oil, Applied Surface Science, 255(4), 2008, pp. 1494-1497

[14] Lipinsky, D.; Brüning, C.; Mayer, C.; Arlinghaus, H. F.; Skubacz, T.; Poll, P.: Oberflächenanalyse der aus Additiven gebildeten tribologischen Schichten mit der Flugzeit-Sekundärionenmassenspektrometrie, Tribologie und Schmierungstechnik, 58(2), 2011, pp. 29-35

[15] Mayer, M.; Lipinsky, D.; Wohlleber, F.; Pflaum, H.; Stahl, K.; Arlinghaus, H. F.: Coordinated test rig and ToF-SIMS experiments to investigate the influence of phosphate glass layers on the friction behavior of a wet clutch, Surface and Interface Analysis, 46(S1), 2014, pp. 401-404

[16] Loos, J.: Einfluss der Reibbeanspruchung auf die WEC-Bildung in Wälzlagern, GfT, 55. Tribologie-Fachtagung 22.09.-24.09.2014 in Göttingen, Band I pp. 23/1-23/13